Design, Development, and Operation of an Electrochemical Urea Removal Reactor for the Application of Portable Dialysis

Kelly Carpenter

A dissertation

submitted in partial fulfillment of the

requirements for the degree of

Doctor of Philosophy

University of Washington

2021

Reading Committee:

Eric M. Stuve, Chair

Stuart Adler

Charles Campbell

Buddy Ratner

Program Authorized to Offer Degree:

Chemical Engineering

University of Washington

Abstract

Design, Development, and Operation of an Electrochemical Urea Removal Reactor for the Application of Portable Dialysis

Kelly Carpenter

Chair of the Supervisory Committee:

Professor Eric M. Stuve

Chemical Engineering

Electrochemical investigations of Pt and Ni-based catalysts were performed in pursuit of designing a reactor capable of oxidizing 15 grams of urea per day for the use of portable dialysis. The electrocatalytic experiments were primarily performed in an alkaline aqueous three-electrode cell utilizing cyclic voltammetry and chronoamperometry; this served to elucidate the oxidation reaction and deactivation mechanisms and measure the kinetic parameters of urea oxidation on various catalysts including Pt, Ni, $Ni(OH)_2$, and 1 mol% iron-

doped $Ni(OH)_2$. The hierarchy of urea oxidation activity in alkaline media is summarized as $Ni(OH)_2$ = Fe-$Ni(OH)_2$ > Ni >> Pt. Creatinine, the second most concentrated solute in urine, was also electrochemically investigated on Ni foam-based electrodes. The creatinine activity is summarized as Fe-$Ni(OH)_2$ > $Ni(OH)_2$ > Ni. Creatinine oxidizes on Fe-$Ni(OH)_2$ and exhibits a concentration and time dependent catalyst deactivation mechanism.

Application of these electrokinetic studies led to design and development of a bench-scale urea removal cell (URC) utilizing a $Ni(OH)_2$ foam anode, a Pt/C supported on carbon cloth cathode, and an alkaline exchange membrane electrolyte. The URC achieves urea removal rates of about 35 mg/cm^2/day from an anolyte feed of 10 mM urea in 0.1 M $KHCO_3$ operating at a pH of 7.4, a temperature of 37 °C, a flowrate of 20 ml/min, and a cell voltage of 1.9 V. The addition of chloride into the anolyte feed induced pitting corrosion of the anode due to a combination of the neutral pH and applied voltage. Early corrosion experiments indicated that even 1% of physiological Cl^- concentrations in the URC create a corrosive environment, primarily due to the Ni foam substrate rather than $Ni(OH)_2$ catalyst. The reported electrocatalytic urea oxidation research and its application to an electrochemical reactor are directly applicable to the general field of wastewater remediation via electrolysis, which has less strict physiological conditions and portability requirements.

TABLE OF CONTENTS

LIST OF FIGURES

LIST OF TABLES

ACKNOWLEDGEMENTS

I have benefitted from the support and care of many people throughout my years at UW. Eric Stuve has taught me much in the way of electrochemistry, experimental planning, and technical writing, and has cultivated a healthy research environment that I am proud to have been a part of. Our group, co-advised by Stuart Adler, has shaped my fundamental understanding of electrochemical systems. Jon Witt, Brian Gerwe, Isaac Kretzmer, and Anthony Pyka have either directly or indirectly aided my research and academic pursuits and provided camaraderie through late nights. Charlie Campbell has provided me with new perspectives and academic discourse during each exam. The CDI team has given me a unique, interdisciplinary perspective through biweekly research meetings; special thanks to Bruce Hinds, Buddy Ratner, Guozheng Zshao, Daniel Shea, and Shen Ren for constructive feedback and discussion.

DEDICATION

To Randy,

Thanks for keeping me smiling through all the ups and downs.

Chapter 1. INTRODUCTION

Millions of patients worldwide suffer from end stage renal disease (ESRD), meaning their kidneys cannot meet their basic survival needs [1]. The only two treatments available for ESRD are kidney transplantation or dialysis. Kidney transplants are the best treatment based on a five-year survival rate of 80% [2]. Comparatively, dialysis has a five-year survival rate of only 35% and a 15–20% mortality rate in the first year [2]. Because the demand for kidney transplants outpaces donor supply by about 8% annually, most ESRD patients rely on dialysis to stay alive [1, 2]. About 90% of dialysis patients receive hemodialysis (HD) treatment as opposed to other types of dialysis [2]. Conventional HD treatment consists of thrice weekly 4-hour sessions during which the patients are tethered to a machine in a clinic while their blood is filtered through a dialyzer. Due to only moderate treatment efficacy, few HD patients are ever fully rehabilitated, which leads to high comorbidity rates and low quality of life [1]. These statistics, in conjunction with the minimal advancements in HD technology since the 1960s, highlight the immediate demand for improved treatment methods.

High mortality in dialysis patients is largely attributed to the intermittency of HD compared to constant, gradual filtration performed by healthy kidneys [3]. Between dialysis sessions, a patient's body retains fluids, wastes, and salts that healthy kidneys would otherwise expel. The accumulation continues until the next HD session whereupon days' worth of fluid buildup is depleted within a few hours. These fluctuations between fluid overload and depletion subject the patient's body to internal stress. In addition to acute physical symptoms such as

exhaustion, swelling, and pain, years of homeostatic stress leads to bleak long-term survival statistics. Research has indicated, however, that more frequent, longer duration dialysis sessions provide a dramatic health benefit for patients, comparable to receiving a kidney transplant [4]. Even when performed in the home overnight, nocturnal dialysis is limited by the underlying HD technology. An excessive volume of water—and accompanying purification system—is required for dialysate preparation, which limits patient mobility and autonomy.

A portable kidney device that attaches to a patient and continuously filters blood throughout their daily routine would revolutionize ESRD treatment and save lives. Such a concept relies on regeneration of a small volume of dialysate, the fluid that flows counter-current to the blood opposite a semipermeable membrane in the dialyzer (Figure 1.1). Successful regeneration of dialysate would remove organic toxins and maintain fluid and electrolyte equilibrium without forming harmful species. The regenerated dialysate would then recirculate for continued filtration rather than being disposed of after a single pass. In addition to increased quality of treatment and patient autonomy, portable dialysis presents an opportunity to decrease dialysate volume and therefore overall cost of HD. In 2016, the U.S. government spent $28 billion on HD treatment, or 6% of the Medicare budget [2].

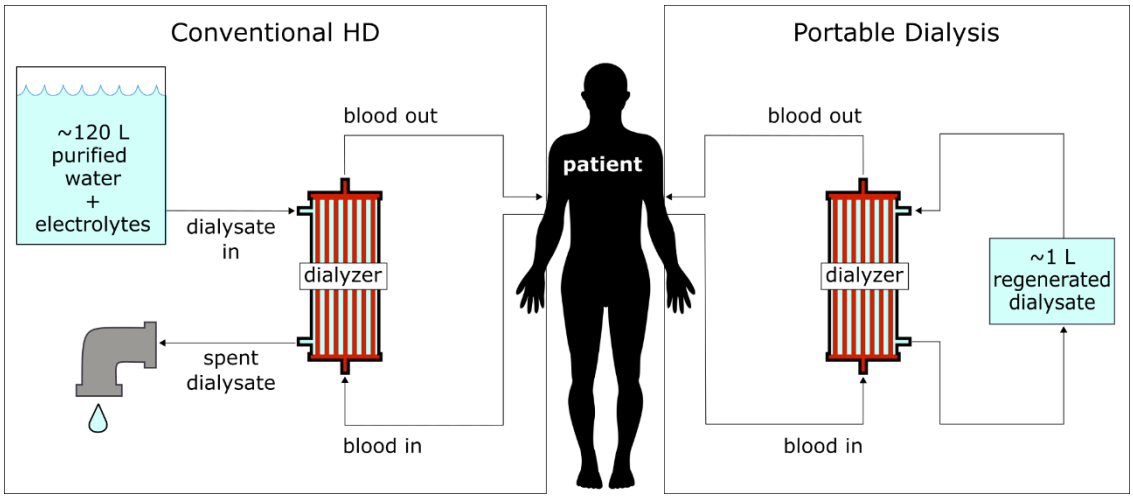

Figure 1.1 Illustration of conventional hemodialysis (HD, left) compared to portable dialysis (right). In conventional HD, dialysate within the dialyzer filters the blood in a single pass design, which demands a large volume of purified water and typically requires in-center treatment. Portable dialysis relies upon closed-loop dialysate regeneration, which removes toxins and excess fluid from spent dialysate without exposing the patient to other harmful byproducts.

Portable dialysis has been researched for decades with some promise [1, 5–7]. A major underlying challenge in all such devices is the efficient clearance of urea. The large quantity of urea needing removal, 12–24 g/day for an average adult, combined with its low affinity for activated carbon, necessitates alternative elimination strategies. Urease enzymatically hydrolyzes urea into toxic ammonium which requires downstream adsorption by large quantities of zirconium phosphate at the expense of portability and cost [6, 7]. Similarly, direct urea adsorption with advanced sorbents requires large volumes of material due to the body's high urea production rate [8, 9].

Aside from sorbents and urease, urea can be removed from an aqueous source through electrochemical oxidation into non-toxic and volatile nitrogen and carbon dioxide [10–13]. Electrodes are small and durable, and urea removal rate can be adjusted by controlling the

voltage across them. The exact mechanism of urea degradation varies depending on electrodes used, composition of analyte, and reaction environment (pH, potential, temperature). As a result, the treated aqueous solution may contain products other than gaseous N_2 and CO_2. If urea electro-oxidation for portable dialysis is to be realized, the production of reactive chlorine and oxidized nitrogen species must be avoided.

Urea is one of the world's most abundant waste products, both industrially and biologically. As a result, multiple technologies— aside from dialysis— rely on urea electrooxidation to either remove it from waste streams or transform it into an energy commodity. Electrochemical degradation of urea and other organic compounds from wastewater is one of the most capable removal methods for environmental denitrification technologies, mainly due to scalability [11, 14, 15]. Furthermore, using a concentrated urea waste stream (or urine) as a fuel cell fuel simultaneously creates electricity *and* removes nitrogen compounds in wastewater [16, 17]. Relatedly, urea or urine can be fed into an electrolysis cell powered by wind or solar energy to generate "green hydrogen", made without fossil fuels, and rectify renewable energy intermittency [18]. Selective and continual removal of urea for dialysis comes with a unique set of requirements that are significantly different than those of wastewater remediation or sustainable energy; however, literature motivated by these applications has laid a crucial foundation for device development and it is therefore briefly summarized in the following chapter.

The focus of this research is to advance the development of a portable dialysis device, specifically the design, development, and operation of a urea removal system. Design of a small electrochemical reactor for use in a medical device relies upon decades of previous fundamental research in electrocatalysis, mass transport, electrochemical thermodynamics, corrosion, membranes, materials science, and biochemistry. The intent of this work is to weave together existing knowledge to build a prototype urea removal device. Research at the intersection of multiple fields is exciting and drives innovation; however, the applied nature tends to favor outcomes over knowledge. Chapter 2 reviews the intermittent evolution of electrochemical dialysate regeneration research, which has led to speculation regarding reasons for discontinuous research. To resist this trend, some results discussed in this manuscript report significant challenges that render some catalysts unfit for use in a portable dialysis device. Such documentation is crucial for the success of future researchers. The findings reported herein summarize novel electrocatalytic research and device design for the application of electrocatalytic regeneration of dialysis for portable dialysis.

Chapter 2. LITERATURE REVIEW

The first published urea electrooxidation research was performed by NASA in an effort to reclaim potable water from urine for extended space flight [19–21]. These studies exclusively focused on indirect urea degradation according to Reaction 2.1. Chloride ions in solution are oxidized to hypochlorite (OCl^-) and other reactive chlorine species (RCS) that chemically oxidize urea into nitrogen and carbon dioxide [20]. Electro-dialysis was then employed to remove excess RCS from water and render it potable. Almost immediately, medical researchers began to explore urea oxidation in an effort to regenerate dialysate because the N_2 and CO_2 products are non-toxic and bubble out of aqueous solution; however, excess RCS build-up due to high chloride content in dialysate remained a serious problem [22]. The hypochlorite-mediated urea oxidation mechanism was investigated with some initial success [23] before follow-up studies identified problematic RCS accumulation [12, 24].

$$CO(NH_2)_{2(aq)} + 3NaOCl_{(aq)} \rightarrow CO_{2(g)} + N_{2(g)} + 3NaCl_{(aq)} + 2H_2O_{(l)} \quad (2.1)$$

In 1974, evidence of direct urea oxidation was observed on a platinum electrode [13]. Direct oxidation, Reaction 2.2, occurs when urea loses electrons to the electrode surface as opposed to a bulk solution reaction with RCS.

$$CO(NH_2)_{2(aq)} + 6OH^-_{(aq)} \rightarrow CO_{2(g)} + N_{2(g)} + 5H_2O_{(l)} + 6e^- \quad (2.2)$$

Urea adsorption and oxidation studies on smooth Pt in acidic, chloride-containing environments revealed that electrode potential can be used to control the preferred urea oxidation mechanism [25]. At voltages below 1.6 V vs. RHE, direct oxidation (Reaction 2.2) dominates. Above 1.6 V vs. RHE Reaction 2.1 dominates as urea reacts with RCS before reaching the anode [11]. Subsequent studies were performed for urea oxidation at lower potentials to limit RCS formation and evaluate methods for portable dialysis on Pt electrodes [12, 26, 27]. These studies demonstrated electrochemical urea removal, although products were not fully analyzed, and other researchers have found that urea oxidation on Pt electrodes forms other species (CNO^-, NO_3^-, NO_2^-, $N_2O_2^-$, N_2O, NO_2) in addition to the expected CO_2 and N_2 [28, 29]. More positive oxidation potentials of urea on Pt promote the formation of nitrogen oxides instead of N_2 [28]. Distribution of additional partially oxidized species is heavily influenced by reaction environment and anode material [30]. Therefore, it cannot be assumed that the nitrogen contained in urea will exclusively form N_2 as written in Reaction 2.2.

Anode catalyst development for indirect urea oxidation in chloride-containing media has been the focus of multiple studies [30–33], primarily for treating wastewater streams. These studies have concluded that Pt electrodes have a lower *faradaic efficiency* for urea decomposition than other anode materials tested, such as boron doped diamond [32], RuO_2 [30], and IrO_2 [34]. Faradic efficiency (η) measures the ability of an electrochemical cell to utilize electrons and is electrolytically defined by Equation 2.1. During urea electrolysis, η represents the amount of charge that participated in urea oxidation divided by the total amount of charge passed through the electrode. In Equation 2.1, ΔC is the change in urea concentration, V is

solution volume, n = 6 moles e^- /mole urea, $F = 9{,}6485$ C/mole e^- , and $\int j(t)dt$ is the charged passed during the experimental time. In this case, lower faradic efficiency means electrons participated in other electrochemical reactions besides UOR (Reaction 2.2) and therefore is often associated with unwanted byproduct formation including electrode corrosion. In more recent research [10, 35–39], artificial kidney devices using noble metals or graphite have been studied for indirect urea oxidation performed via current control without reporting cell voltage. Electrode voltage is critical to understand corrosion risk, as it can present a risk in a medical device. Because of this concern, Wester et al concluded that graphite anodes should be used in dialysate regeneration to prevent metal leeching, as reported for Pt and RuO_2 electrodes [10]; however, their analysis did not take into account loss of graphite electrodes due to oxidation into CO_2 which is known to occur at potentials above 1.2 V RHE and become more severe with higher temperatures and voltages [40, 41].

$$\eta = \frac{\Delta C V n F}{\int j(t)dt} \tag{2.1}$$

Most of the modern urea oxidation literature is motivated by wastewater remediation, urea fuel cells, or green hydrogen production [15, 42–49]. Urea is concentrated in industrial and agricultural waste streams due to a dramatic increase in use over the past few decades [50]. It's role in anthropogenic eutrophication of lakes is well studied and presents significant environmental concerns [51]. In aqueous environments, urea hydrolysis (Reaction 2.3) typically requires temperatures above 60 °C to proceed; however, the enzyme urease, which is present in most bacteria and plants, causes urea hydrolysis to occur rapidly at low temperatures and results

in the formation of ammonia (NH_3) gas [52]. Ammonia volatilization leads to major inefficiencies for global agricultural systems, averaging to 18% loss of applied synthetic nitrogen [53]. Additionally, NH_3 is further transformed by plants, bacteria, and archaea to form nitrous oxide (N_2O) and nitrogen oxides (NO_x) which contribute to smog, acid rain and global warming [54, 55]. Thus, removal of urea from industrial and agricultural runoff is agriculturally and environmentally prudent.

$$CO(NH_2)_{2(aq)} + H_2O_{(l)} \xrightarrow{\text{urease}} CO_{2(g)} + 2NH_{3(g)} \quad (2.3)$$

In 2009, Botte et al [15] concluded that Ni is more active towards urea oxidation in alkaline media—and in the absence of chloride—than the platinum group metals (PGM) historically used for urea oxidation. It is understood that Ni^{3+} is more active than Ni^{2+} for oxidation of small organic compounds [56–58]. In an alkaline environment, Ni converts to divalent nickel hydroxide [$Ni(OH)_2$], which further oxidizes to the trivalent state, nickel oxyhydroxide (NiOOH), according to Reaction 2.4 at a theoretical potential of 0.49 V vs. SHE [15].

$$Ni(OH)_{2(s)} + OH^-_{(aq)} \rightleftarrows NiOOH_{(s)} + H_2O_{(l)} + e^- \quad (2.4)$$

Because the Ni^{3+} sites are demonstrated to be active in urea oxidation, a Ni electrode activation procedure is used to obtain maximum catalytic activity by cycling electrode voltage around the Ni^{2+}/Ni^{3+} transition to grow oxide layers [57, 59, 60].

A series of studies was performed to understand the mechanism of urea oxidation on Ni catalysts in alkaline media [61–64]. Similar to hypochlorite-mediated urea oxidation in neutral

solutions, direct (Reaction 2.1) and indirect mechanisms (Reactions 2.4 and 2.5) exist in alkaline media [49, 61, 62]. The indirect mechanism consists of an electrochemical-chemical (E-C) pathway defined by electrochemical oxidation of Ni^{2+} to Ni^{3+} (Reaction 2.4) followed by a surface reaction of urea on Ni^{3+}(Reaction 2.5). Based on potential oscillation [63], X-ray diffraction [64], and electrochemical impedance spectroscopy (EIS) studies [49], it has been confirmed that the E-C pathway is dominant when urea oxidation occurs in alkaline media on a Ni anode.

$$CO(NH_2)_{2(aq)} + 6NiOOH_{(s)} + H_2O_{(l)} \rightarrow N_{2(g)} + CO_{2(g)} + 6Ni(OH)_{2(s)} \qquad (2.5)$$

Many recent studies have explored Ni-based anode materials for urea oxidation [42–48, 65–72]. Improved performance and stability are largely due to nanostructured surfaces and multi-metal interactions. Incorporation of carbon nanomaterials [44, 47, 48, 70, 73] and electrode preparation procedures to increase nanostructure [42, 43, 45, 46, 66, 68, 71, 72] have drastically enhanced the electrochemical active surface area to increase anodic current density while maintaining constant geometric area. Combination of Ni with other catalysts—notably Co, Zn, Mn, and PGMs—has effectively reduced the urea oxidation overpotential by 40–150 mV while maintaining electrode stability [42, 43, 65, 67, 69, 72–74].

In pursuit of a more portable urea oxidation system, one study assessed the performance of a polymer gel in place of aqueous potassium hydroxide (KOH) electrolyte [59]. The polymer and KOH content of the gel were varied to optimize mechanical strength and conductivity. The gel electrolyte had a slightly lower ionic conductivity than aqueous KOH and retention of electrolyte within the gel was not perfect; however, the compact design provides a benefit for

mobile and alkaline-sensitive applications. These advantages have been further exploited with the advancement of alkaline membrane-based technologies such as fuel cells and electrolyzers, discussed below.

In 2010, the direct urea fuel cell concept was published [75], which gave rise to an incredible surge in urea electrooxidation research for energy production and storage applications. Urea fuel cells (UFCs), including the direct urine fuel cell, produce power from waste [73, 75–81] while urea electrolyzers generate green hydrogen for energy storage [18, 59, 65, 66, 82, 83] (Figure 2.1). The theoretical cell voltage (E^0_{cell}) of a fuel cell or electrolyzer is defined as the difference between the standard half-cell potentials of the cathode (E^0_c) and anode (E^0_a) reactions (Equation 2.2). When urea oxidation (Reaction 2.2, E^0 = –0.75 V vs. RHE) occurs at the anode while alkaline O_2 reduction (Reaction 2.6, E^0 = +0.40 V vs. RHE) occurs at the cathode, E^0_{cell} = +1.15 V, the positive sign meaning the cell is galvanic and therefore capable of producing power (Figure 2.1a) [75]. Electrolytic cells, on the other hand, have a negative cell potential and therefore require an applied potential to drive a chemical reaction. If alkaline water reduction (Reaction 2.7, E^0 =–0.83 V vs. RHE) occurs at the cathode instead of oxygen reduction, then E^0_{cell} = –0.08 V meaning energy is required when hydrogen is generated at the cathode (Figure 2.1b).

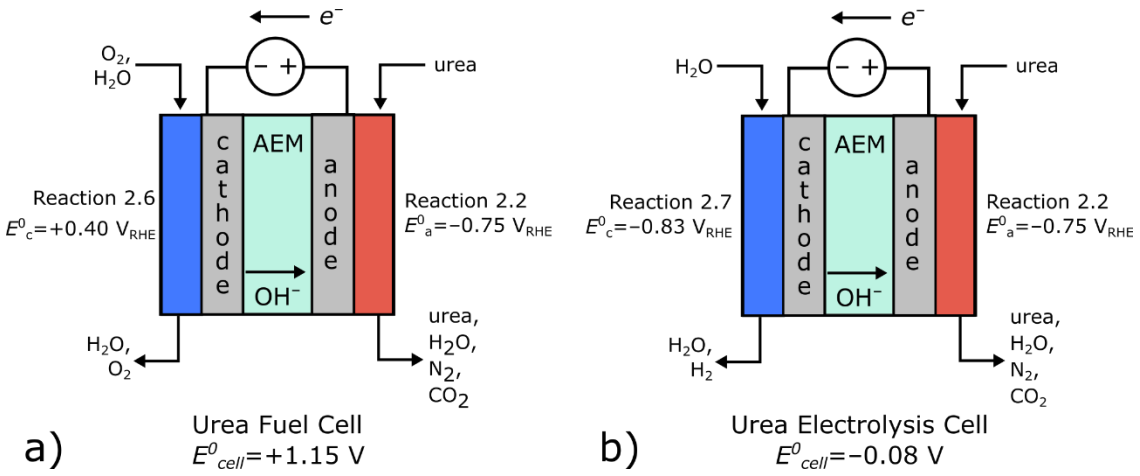

Figure 2.1 Schematic representation of urea-based a) fuel cell and b) electrolysis cell. Both configurations oxidize urea on the anode. The fuel cell cathode reduces oxygen to produce power while the electrolysis cell consumes energy to produce hydrogen at the cathode.

$$E^0_{cell} = E^0_c - E^0_a \tag{2.2}$$

$$\frac{3}{2}\mathrm{O}_{2(g)} + 3\mathrm{H_2O}_{(l)} + 6e^- \rightarrow 6\mathrm{OH}^-_{(aq)} \tag{2.6}$$

$$6\mathrm{H_2O}_{(l)} + 6e^- \rightarrow 6\mathrm{OH}^-_{(aq)} + 3\mathrm{H}_{2(g)} \tag{2.7}$$

Polymer electrolyte membrane cells demonstrate increased portability and safety over their aqueous counterparts. A polymer backbone functionalized with charged, immobilized ions, called an ionomer, maintains the membrane structure while oppositely charged, mobile ions interact to electrostatically neutralize the membrane. When the ionomer is positively charged and the mobile counterions are negatively charged, the membrane is referred to as an anion exchange membrane (AEM, Figure 2.2). For these membranes to obey electroneutrality, the mobile ions will not spontaneously leech from the ionomer without a flux of anions into the AEM

elsewhere. Although these membranes are thin and ionically conductive, they are *not* electrically conductive and therefore allow for compact cell design without a risk of short-circuiting. Urea fuel cells and electrolyzers utilize AEMs because trace amounts (>0.1 ppm) of NH_3 will irreversibly damage a proton exchange membrane (PEM) [84, 85]. Although urea hydrolysis (Reaction 2.3) is unfavorable at room temperature without urease, the risk of producing NH_3 was originally cited as a reason not to use PEMs in urea fuel cells [75]. More importantly, urea oxidation kinetics and thermodynamics benefit from the high alkalinity in the AEM—in fact, two studies have independently demonstrated a *higher* UOR order with respect to OH^- concentration compared to that of urea [61, 86].

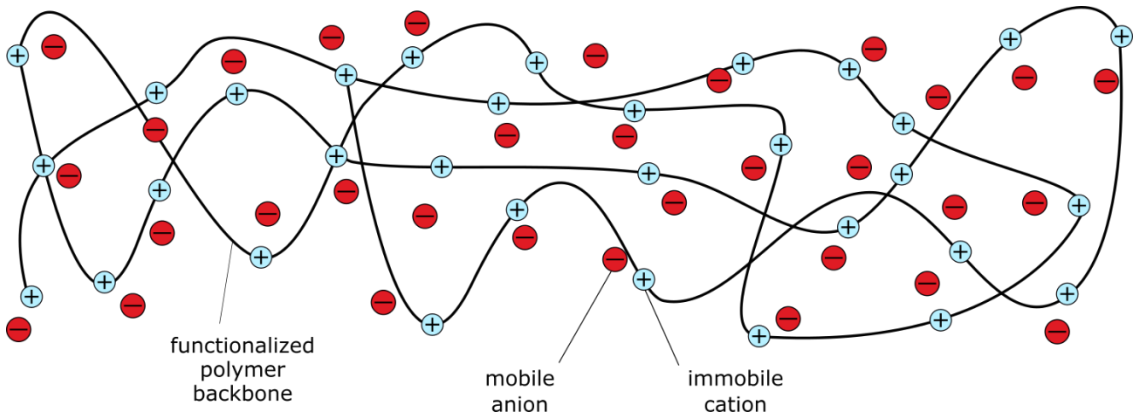

Figure 2.2 Schematic illustration, on a molecular scale, of an AEM. The polymer backbone is functionalized with positive species that interact electrostatically with mobile anions. Water molecules are ubiquitous and have been omitted for clarity. In urea fuel/electrolysis cells, the membrane pH >14 when full hydrated and hydroxylated.

Feed streams for urea fuel cells vary in urea concentration, although most use 0.33 M to replicate urine [76]. An increase in urea concentration of fuel beyond 0.33 M is generally detrimental to power density due to urea crossover through the membrane [75, 87]. Improvements in UFC power density have been reported by adding KOH into the anode fuel [76]

and increasing operating temperatures to reduce the overpotential caused by slow urea oxidation kinetics [87]. Cathode fuel is often humid air or oxygen, but can be modified for higher cell voltage using hydrogen peroxide (H_2O_2) [78]. Furthermore, utilizing toxic industrial effluent as the catholyte can reduce Cr^{6+} to Cr^{3+} at the cathode while oxidizing urea on the anode, in effect transforming two waste streams into power [77].

The literature review reveals important information about urea oxidation and the various reasons it has been studied. Although dialysate regeneration motivated some of the earliest urea oxidation studies in the 1970's, the publication streak ceased by 1990, likely due to the formation of toxic NH_3 [12, 13, 22, 26, 27]. About a decade later, a Russian group briefly resumed similar research on Pt, yet may have observed excessive nitrate, RCS, or acidosis problems due to low selectivity [35–38]. Within the past few years, researchers in the Netherlands have transitioned away from Pt in favor of graphite electrodes to avoid metal leaching [10] and performed the first in vivo study performing regenerative dialysis on goats [10, 39]. Such sporadic research in electrochemical dialysate regeneration demonstrates the considerable potential and challenge of the undertaking. In more recent decades, urea oxidation has primarily been the focus of research motivated instead by waste stream remediation, hydrogen production, and fuel cells. The progress made towards understanding urea oxidation mechanisms and developing active and selective catalysts helps to direct and motivate the reassessment of electro-oxidation for dialysate regeneration. The experiments and discussion in the remainder of this document intend to provide insight into this important, yet niche classification of urea electrooxidation.

Chapter 3. EXPERIMENTAL METHODS

The experiments are categorized by type of electrochemical cell used, a three-electrode aqueous cell or a two-electrode membrane cell. The two-electrode cell, called the urea removal cell (URC), is a bench-scale prototype device that integrates catalysts, membrane, and operational parameters. The advantage of the URC is its form factor, which is a realistic representation of the final envisioned device. Alternatively, the three-electrode cell enables faster electrocatalyst experiments to be performed in a well-controlled environment for comparison. Catalyst studies were first performed in the three-electrode system to assess urea oxidation activity at well-defined electrode potentials. The most promising catalysts were then scaled up for use in longer URC experiments to measure and optimize urea removal rates.

3.1 THREE-ELECTRODE SYSTEM

A 3-electrode cell (Pine Electrochemistry) was used to screen catalysts and to decouple membrane effects from catalyst and operational effects. Figure 3.1 depicts the 150 ml, three-electrode cell set up; a smaller 20 ml cell was also used for the small disk electrodes. The cell consists of a working electrode (WE), a counter electrode (CE) and a reference electrode (RE) submerged in supporting electrolyte at room temperature. In this arrangement, current passes within the circuit connecting the WE and the CE, while the potential of the WE is measured against the RE. Due to the presence of the third electrode, the WE potential and current density are both well-defined.

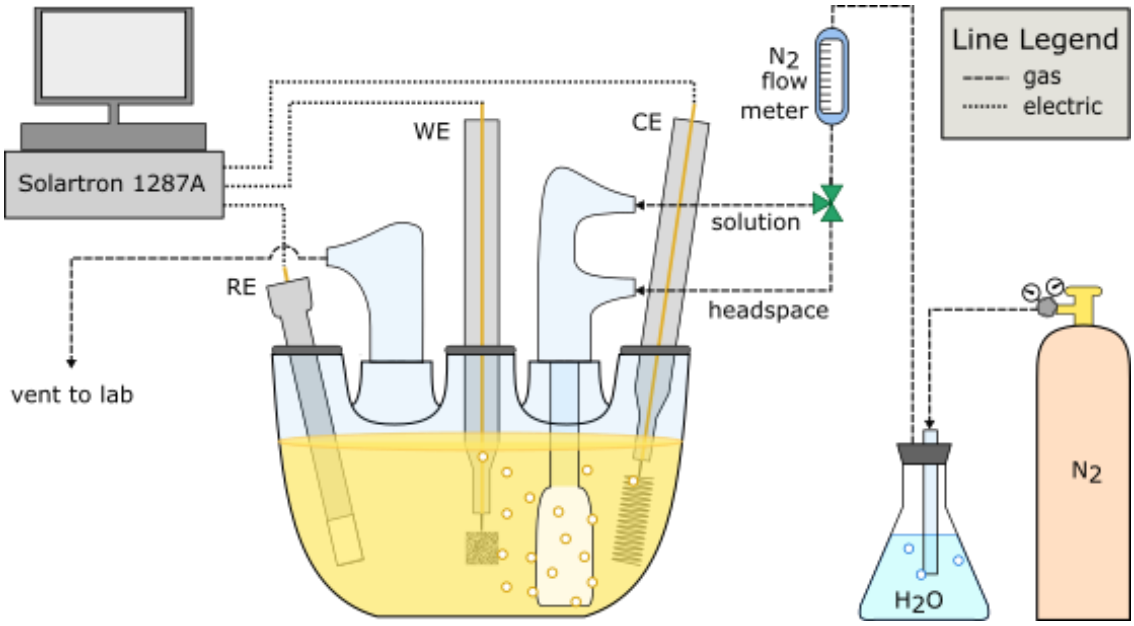

Figure 3.1 Illustration of the three-electrode cell experimental setup including WE, CE, RE, electrical connections (dotted lines), and N_2 purge lines into the solution and headspace. Nitrogen was hydrated before entering the cell to avoid absorption of solution by dry gas. Experiments were performed by a potentiostat (Solartron 2187A) controlled by a computer via CorrWare (Scribner).

Multiple types of each electrode were used in various experiments, as listed in Table 3.1. Platinum and nickel based WEs were studied for urea electrooxidation in the search for an active, stable URC anode. Platinum was also studied for water reduction for use as a URC cathode. Glassy carbon electrodes (GCEs) were used as substrates for nickel electroplating and sputtering to study various forms of Ni electrocatalysts. Nickel foam-based electrodes were homemade (see 3.3.1), and Figure 3.1 depicts an example. The CE in each experiment was sized depending on the surface area of the WE electrode to ensure that the CE reaction did not limit cell current. Foam electrodes, which can achieve active electrochemical surface area (ECSA) thousands of times larger than their geometric surface area, required a high surface area Pt CE (homemade), while disk electrodes utilized a standard Pt coil electrode (Pine Electrochemistry).

Electrode	Type	Use	Brand
Pt disk	WE	Urea oxidation, water reduction; 0.02 cm^2	Basi
Glassy carbon disk	WE	Ni electrodeposition, ink-cast; 0.07 cm^2	Basi
Ni disk	WE	Urea oxidation; 0.07 cm^2	Basi
Ni foam	WE	Urea oxidation; 0.5 – 1.0 cm_{geo}^2	Homemade
$Ni(OH)_2$ foam	WE	Urea oxidation, creatinine oxidation; 0.5 – 1.0 cm_{geo}^2	Homemade
1% Fe $Ni(OH)_2$ foam	WE	Urea oxidation, creatinine oxidation; 0.5 – 1.0 cm_{geo}^2	Homemade
Pt coil	CE	Paired with disk WEs	Pine
High surface area Pt	CE	Paired with foam based WEs	Homemade
Ag/AgCl, Sat. KCl	RE	Electrolyte pH 0–8; E_{ref}^0 =0.199 V vs. NHE	Pine
Hg/HgO; 4.24 M KOH	RE	Electrolyte pH 8–14; E_{ref}^0 = 0.098 V vs. NHE	Pine

Table 3.1 Types of electrodes used in the three-electrode system. A summary of procedures for making each type of homemade WE can be found in 3.3.1 with more detailed preparation procedures in Appendices A—C.

The type of RE used in each experiment was dictated by solution pH; strong alkaline solutions required a Hg/HgO reference, otherwise a Ag/AgCl reference was used. Many WE potentials reported in text and figures have been converted to the pH-independent reversible hydrogen electrode (RHE) scale using the conversion provided by Equation 3.1. Each standard reference electrode potential (E_{ref}^0) is noted in Table 3.1. The RHE scale is convenient to use when translating WE potentials into URC cell voltages, E_{cell}, because H_2 evolution is the cathode reaction. Therefore, E_{cell} is equal to E_{anode} vs. RHE plus the effects of cell overpotentials.

$$E_{RHE} = E_{measured} + E_{ref}^0 + 0.059\text{pH} \tag{3.1}$$

Supporting electrolyte allows for ion migration to balance the movement of charge created by the electrochemical current. Supporting electrolyte is not intended to be consumed

during anode or cathode reaction, therefore its concentration stays constant. Supporting electrolyte used for urea oxidation studies was 1.0 M or 0.1 M KOH to mimic the high alkalinity of the URC membrane. Potassium bicarbonate ($KHCO_3$) and sodium chloride (NaCl) were occasionally used in the supporting electrolyte to mimic the URC anolyte and for corrosion studies. The electrolyte solution was sparged with N_2 for at least 5 minutes prior to running experiments to remove dissolved oxygen from the solution and to limit KOH absorption of atmospheric CO_2. Cell headspace was flushed with N_2 throughout each experiment to ensure a stable environment without disturbing the electrolyte. When Ni foam-based electrodes were used in the 3-electrode cell, the solution was sparged throughout the experiment to increase mass transport at the electrode surface and within its pores. For urea oxidation studies, urea was added into the supporting electrolyte up to 10 mM to simulate serum urea levels. In creatinine electrooxidation studies, creatinine and urea were added to the cell individually and simultaneously in concentrations that mimic dialysate (10 mM urea, 60 µM creatinine) and urine (0.33 M urea, 18 mM creatinine).

3.2 Two-Electrode System

Figure 3.2 shows a schematic of the two-electrode URC with the hydrogen evolution reaction (HER, Reaction 2.7) occurring at the cathode and UOR (Reaction 2.2) occurring at the anode. As in the three-electrode cell, the critical components of the URC are the electrodes and the electrolyte; however, there are only two electrodes, and the electrolyte takes the form of an anion exchange membrane (AEM). Cell voltage was measured between the anode and cathode without a reference electrode. For this reason, the three-electrode cell experiments were critical

to approximate actual electrode potentials within the URC. The anodic and cathodic reactions are coupled through shared electrons (e^-) and hydroxide ions (OH^-) (Figure 3.2). Electrons pass from the anode to the cathode during operation, while hydroxide ions in the AEM migrate in the opposite direction and "drag" a solvation shell of β water molecules along (Figure 3.2). For readability, Figure 3.2 is not drawn to scale; in reality, the electrodes are each on the order of ~1 mm thick, the AEM is ~100 µm thick, and the endplates are each ~1 cm thick.

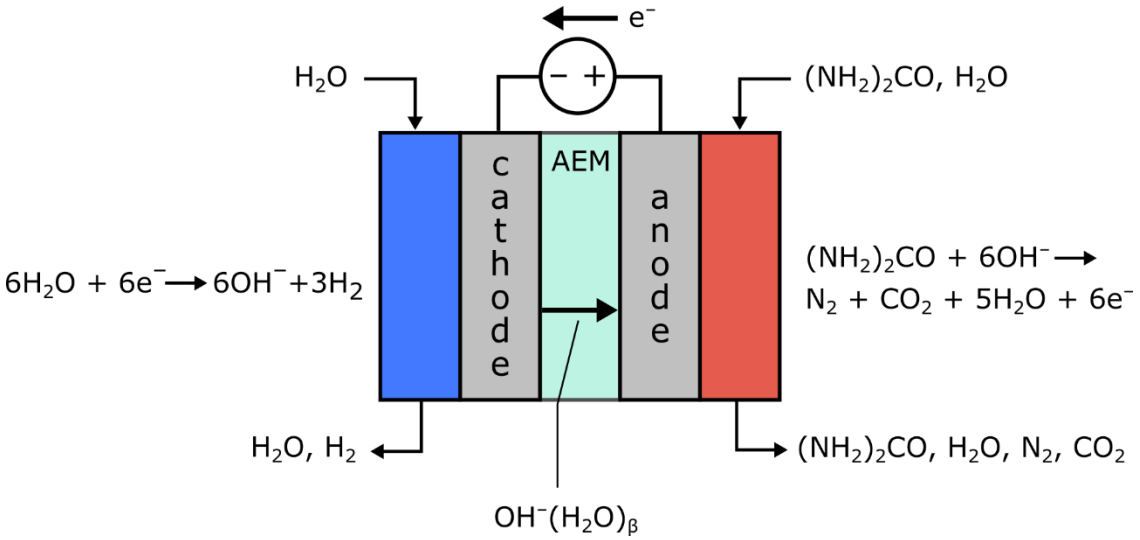

Figure 3.2 A cross-sectional side view schematic representation of the URC depicting the anode, cathode, AEM, relevant reactions, and inlet/outlet streams. During operation, the anode potential is positive relative to the cathode to provide sufficient overpotential for urea electrooxidation.

The URC may be assembled in 5 cm^2 or 25 cm^2 active area configurations. Catalysts were initially made into 5 cm^2 electrodes and sized up to 25 cm^2 if they performed well. URC anodes were nickel-based catalysts. Nickel supported on carbon (Ni/C) was originally used, followed by Ni foam, and eventually nickel-hydroxy foam (NHF). Cathodes were 20% Pt mixed with carbon powder (Vulcan XC-72R) and sprayed on a carbon cloth support, referred to as Pt/C. The methods used to make URC anodes and Pt/C cathodes are briefly summarized in 3.3.1 with more detailed

procedures outlined in Appendices A and B. Commercially available AEMs were purchased according to their high mechanical and chemical stability, discussed further in 3.3.2.

The URC experimental system (Figure 3.3) included fluid and gas delivery along with temperature, pH, and electrical measurement and control devices. Peristaltic pumps (Cole-Parmer) delivered fluids to the cathode and anode, referred to as the catholyte and anolyte, respectively. A dual probe heater (Scribner) was powered by a variable transformer and heated each URC endplate from the backside (not shown in Figure 3.3). A thermocouple (TC) in the cathode endplate reported the cell temperature, which maintained a narrow temperature range of 37–40 °C. The catholyte was ultrapure water recirculated at room temperature and contained in a closed reservoir to limit evaporation. Like the idea of a high surface area CE in the three-electrode cell, URC cathodes were designed to have higher than necessary catalyst loading to ensure the cathode was not limiting reaction. As a result, when tested, the catholyte flowrate did not impact URC current density and was kept around 10 mL/min to minimize tubing wear. The anolyte varied by experiment and contained KOH or $KHCO_3$ with urea and/or NaCl. Because urea oxidation on the anode is the reaction of interest, the anolyte pH, temperature, and flowrates were closely monitored and controlled. A temperature control loop used the anolyte TC and a hot plate (Isotemp) to maintain the temperature at 37 °C. Constant mixing limited thermal and concentration gradients in the 4.0 L anolyte feed reservoir.

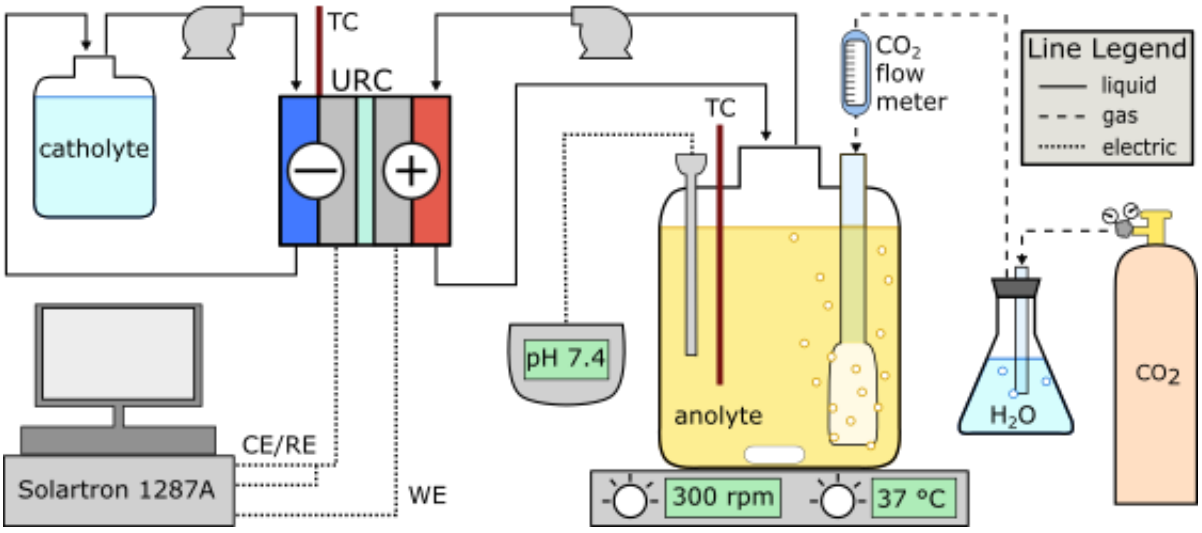

Figure 3.3 The two-electrode experimental system consisted of the URC, catholyte flow loop, and anolyte flow loop. Thermocouples measured temperature of the cathode endplate and the anolyte feed, each heated separately. A pressurized CO_2 tank, rotameter flow meter, and pH meter served as the anolyte pH control system. Electrochemical experiments were controlled and monitored by the potentiostat and computer.

Anolyte pH control was achieved via the carbonate buffer system, one of the human body's essential pH regulation systems [88]. During pH-controlled experiments, the anolyte consisted of 25–100 mM $KHCO_3$ and urea, which had a slightly alkaline pH of 8.3–8.6. To maintain a biological pH of 7.4, the partial pressure of CO_2 was increased, which caused an increase in dissolved CO_2 according to Reaction 3.1, dictated by Henry's Law. According to the buffer system equilibrium (Reactions 3.2), increasing the concentration of dissolved CO_2 creates carbonic acid which immediately dissociates into bicarbonate ion and a proton, resulting in pH reduction. A needle valve rotameter (Supelco) was used to precisely control CO_2 flow into the fritted sparge tube (Figure 3.3). A pH probe and meter were used for real-time solution pH measurements, and the CO_2 flowrate was manually adjusted in response. To achieve a pH of 7.4 at 37 °C in 25 mM

bicarbonate, a CO_2 flow around 80 ml/min was required. The system pH response was sensitive to changes in CO_2 flowrates and exhibited nearly immediate response times.

$$CO_{2(g)} \rightleftarrows CO_{2(aq)} \tag{3.1}$$

$$CO_{2(aq)} + H_2O_{(l)} \rightleftarrows H_2CO_{3(aq)} \rightleftarrows H^+_{(aq)} + HCO^-_{3(aq)} \tag{3.2}$$

3.3 MATERIALS

3.3.1 *Electrode Preparation*

Disk electrodes used in the three-electrode cell (Table 3.1) were polished immediately before each experiment to achieve a reproducible catalyst surface. Alumina polishing pastes of grit size 0.3 µm and 0.05 µm were used in succession followed by sonication in ultrapure water for 60 s to dislodge alumina particles and achieve a mirror finish. Prior to purchasing Ni disk electrodes, GCEs were used as substrate for electrodepositing Ni in varying thicknesses. Electrodeposition was performed by constant potential reduction of Ni^{2+} onto a GCE to obtain a Ni film. Multiple electro-deposition solutions were used to make Ni electrodes, denoted in Table 5.1.

Both the three-electrode cell and the URC utilized Ni foam-based electrodes. Ni foam (Sigma-Aldrich) was purchased in 1.6 mm thick sheets with a porosity of 95%. Bare Ni foam was cut to size with a laser cutter, soaked in 3 M HCl for 5 minutes to reduce the surface oxide layer, rinsed well with ultrapure water, rinsed once more with ethanol, and left to fully dry in air. At

this point, the Ni foam was made into a WE for the three-electrode cell or used as a substrate for $Ni(OH)_2$ growth, both described briefly below.

A one-pot hydrothermal synthesis procedure [89–91] was adapted for the growth of $Ni(OH)_2$ and 1% Fe-doped $Ni(OH)_2$ on Ni foam substrate, herein referred to as nickel hydroxy foam (NHF) and Fe-NHF, respectively. First, Ni foam was cut to size and acid cleaned, as specified above. Once fully dried, electrode masses were recorded to later calculate catalyst mass loading. The clean, dry Ni foam pieces were placed vertically into a Teflon-lined stainless-steel hydrothermal vessel (Toption Labs) before the hydrothermal solution was added. To make the hydrothermal solution, urea (0.125 M) and $Ni(NO_3)_2 \cdot 6H_2O$ (0.0125 M) were dissolved into enough ultrapure water to cover all electrodes when standing vertically in the small (20 ml) or large (1000 ml) hydrothermal vessel, dictated by electrode size. The Fe-NHF hydrothermal solution was made to contain 1 mol% Fe salt by adding $Fe(NO_3)_3 \cdot 9H_2O$ in addition to $Ni(NO_3)_2 \cdot 6H_2O$ while the urea concentration remained unchanged. The growth of Fe-NHF was otherwise identical to that of NHF. With its lid secured, the vessel was placed into a 105 °C oven for 12 hours. Once removed from the oven, the vessel was allowed to cool to room temperature before it was opened. The electrodes were removed with tweezers, rinsed well with DI water and ethanol, and left to dry before their final masses were recorded. Appendix A provides a detailed procedure for making NHF electrodes for the URC.

Homemade Ni-foam based WEs for the three-electrode cell (Table 3.1) were designed based on the following required criteria: a) low resistance electrical contact, b) secure mounting within the cell, c) the ability to swap electrodes easily, and d) no introduction of new chemical

species into the cell. The resulting design includes WE holders and removable “heads”, shown in Figure 3.4. After Ni foam was cut to 0.5–1.0 cm^2 and acid cleaned, a piece of Ni wire was spot welded in three locations along the foam (highlighted in red in Figure 3.4) to achieve stable physical and electrical connection. To make a NHF WE, this substrate was then placed into the hydrothermal bath, as described above. Once removed and rinsed, these electrodes were immersed, wire-down, into 3 M HCl for 30 minutes to chemically reduce the $Ni(OH)_2$ for acceptable electrical contact with a female snap connector. Last, the female snap connector was crimped onto the Ni wire for easy mounting and interchanging of WE heads onto a WE holder. Working electrode holders were made with copper wire housed within a glass pipette body and epoxy resin filled for durability. A male snap was crimped onto the copper wire, which served as the WE head mounting mechanism. Appendix C provides a detailed procedure for making WE heads and holders. While in use within the three-electrode cell, the electrolyte solution only contacted the WE foam and Ni wire portions (represented by the dotted line in Figure 3.4) of the WE head while the female snap connector, a cheap metal alloy, was not submerged.

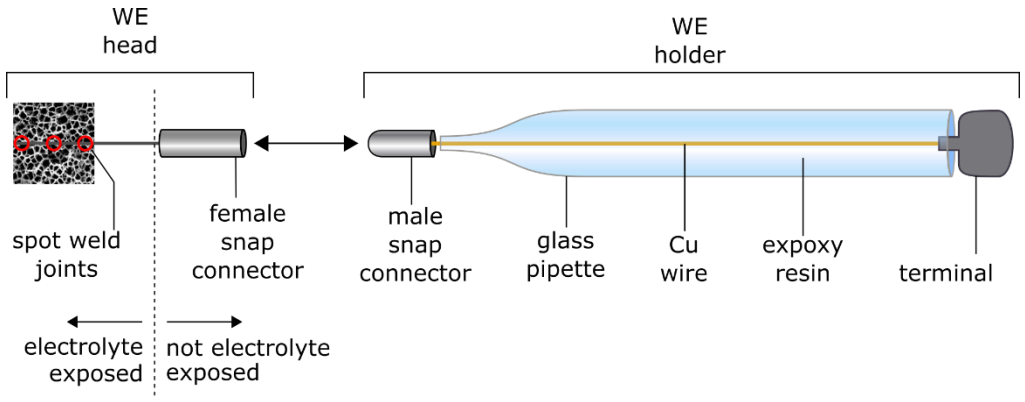

Figure 3.4 Illustration of a homemade Ni foam based WE head and holder. A dotted line delineates the electrolyte exposed region of the WE head while in use

within the three-electrode cell. Drawing not to scale, photographs are found in Appendix C.

Cathodes for the URC were made by spraying Pt/C ink onto carbon cloth to create gas diffusion electrodes (GDE). The GDEs were made to have 1.0 mg/cm^2 of Pt, an intentionally high catalyst loading. The high cathode catalyst loading ensured that the cathode reaction was not limiting overall URC current. Ink was made by mixing catalyst powder, solvent, and anion exchange ionomer in mass percentages of 1%, 3%, and 96%, respectively. The catalyst powder was 20% Pt supported on Vulcan XC-72R (Fuel Cell Store). The ionomer solution was 10% FAA-3 dissolved in N-methyl-2-pyrrolidone (NMP, Fuel Cell Store). This ionomer is the solution form of the Fumasep AEMs used and consists of a polyaromatic polymer with quaternary ammonium functional groups and Br^- counterions. The solvent used was 50% methanol, 50% tetrahydrofuran (THF), by volume (Sigma-Aldrich). Solvent was mixed with catalyst powder and kept stirring while ionomer was added dropwise to facilitate dispersion. The vessel was sealed and allowed to stir vigorously for 1 hour, followed by sonication for 1 hour. Ink was moved directly from the sonication bath back to the stir plate and remained stirring while ~2 ml aliquots were loaded into an airbrush (Iwata) for spraying. Ink was not allowed to settle at any point during the ink preparation process due to the risk of ionomer phase separation, which would reduce the number of triple phase boundary active sites in the final catalyst layer. The ink solution was sprayed onto a carbon cloth substrate (AvCarb 1071 HCB, 356 µm) that was heated to 80 °C on a hotplate. A detailed procedure outlining URC cathode production is included in Appendix B.

3.3.2 *URC Components and Assembly*

Aside from the basic electrochemical cell including anode/membrane/cathode (Figure 3.2), the URC requires hardware for reactant delivery, cell compression, and sealing. An exploded view diagram of the URC is provided in Figure 3.5, with a list of each component material provided in Table 3.2. Membranes were shipped and stored in dry bromide form. Prior to mounting in the cell, AEMs were hydrated and ion exchanged to hydroxyl form by soaking in 1.0 M KOH for 24 hours. Thinner AEMs experienced puncture failure against rough Ni-foam edges either during URC assembly (30 µm, Ionomr) or during URC heating (75 µm, Fumasep) due to thermal expansion. Hydrated and activated 130 µm membranes functioned well for months of testing.

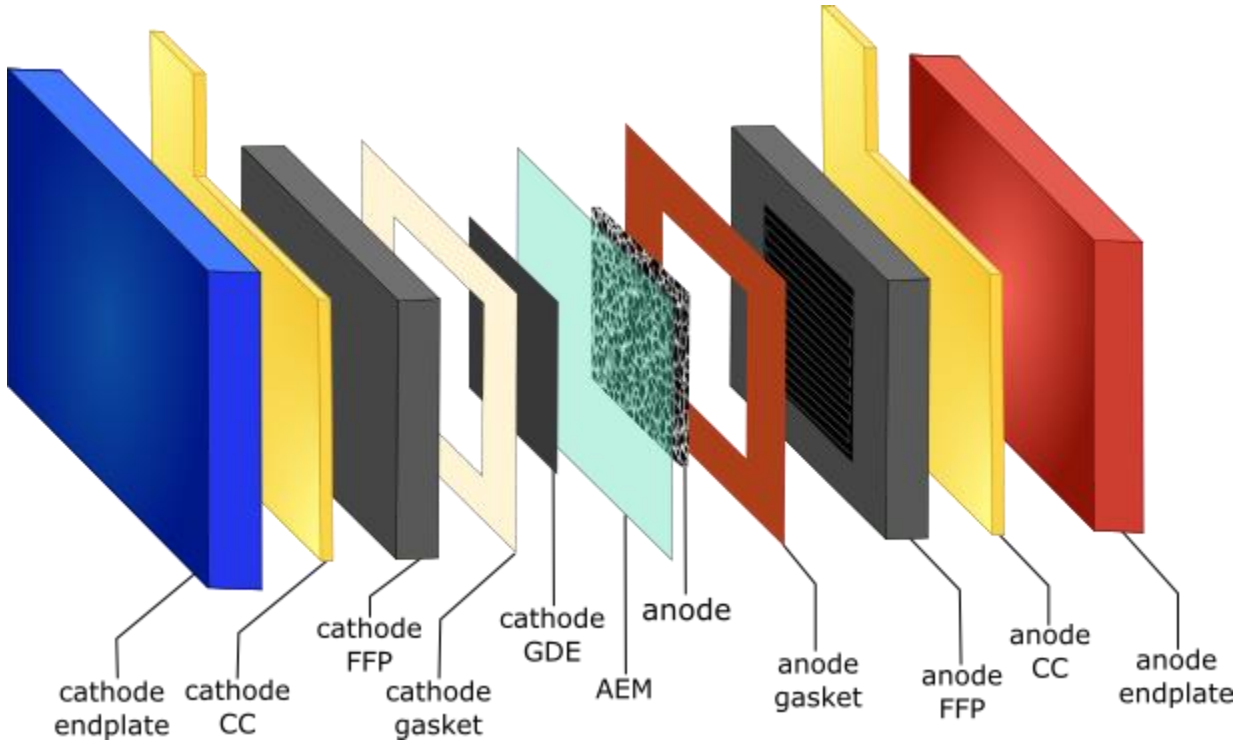

Figure 3.5 An exploded view diagram of the URC depicting all components and their mounting order. Machined bolt holes and reactant inlet/outlets in each

endplate and CC are not shown for simplicity. Materials for each component are listed in Table 3.2.

The endplates, current collectors (CC), and flow field plates (FFP) were purchased from Scribner Associates Inc. The chemically resistant flow path of the anode endplate enabled use of alkaline solution during URC break-in (detailed in Appendix E). The URC was assembled by successively stacking the components in the order shown in Figure 3.5: anode endplate, anode CC, anode FFP, anode gasket/anode, AEM, cathode gasket/cathode, cathode FFP, cathode CC, and cathode endplate. Eight bolts (not shown in Figure 3.5) were lightly greased and tightened in 5 lb_f-in increments to a final torque of 20 lb_f-in to achieve even and reproducible cell compression. Irreversible compression of the NHF anode by about 25% is expected the first time an anode is mounted into the URC.

Component	Half-cell	Material
Endplate	Anode	Anodized aluminum with non-corrosive, chemically resistant flow paths
Endplate	Cathode	Anodized aluminum
Current collector (CC)	Anode & cathode	Gold-plated copper
Flow field plates (FFP)	Anode & cathode	POCO graphite, serpentine flow fields (5 cm^2 or 25 cm^2)
Gasket	Anode	1/16” heat resistant silicone
Gasket	Cathode	1/32” PTFE
Electrode	Anode	NHF (Appendix A)
Electrode	Cathode	Pt/C on carbon cloth (Appendix B)

Anion Exchange Membrane (AEM)	N/A	Fumasep FAA–3–PK–130; PK reinforced polyaromatic polymer with quaternary ammonium functional groups, 130 µm thick

Table 3.2 Components necessary to operate the URC. Multiple gaskets, electrodes, and AEMs have been tested; materials listed are the best performing or most durable.

3.4 Sample Characterization

3.4.1 *Morphology*

Homemade electrodes, including hydrothermally grown NHF and airbrush sprayed Pt/C, were characterized according to catalyst mass loading and scanning electron microscopy (FEI XL830 Dual Beam SEM/FIB) before being mounted into the three-electrode cell or the URC. Energy-dispersive spectroscopy (EDS, Oxford) was used to assess elemental makeup of Fe-NHF to confirm Fe doping. The hydrothermal procedure used for NHF and Fe-NHF growth resulted in consistent total mass loadings of 1 mg/cm_{geo}^2.

3.4.2 *Electrochemical*

Both systems were electrically connected to a Solartron 1287A potentiostat coupled to CorrWare software for experimental control and data collection (Figure 3.1, Figure 3.3). During electrochemical experiments, the cell under investigation was subjected to a programmed potential—potentiostatic, potential stairstep, linear sweep voltammetry, or cyclic voltammetry (CV)—and the current response was recorded and analyzed. In the three-electrode cell, CVs were

used to measure electrode activity over a range of potentials; however, due to the complicated nature of the URC under non-steady-state conditions, potential stair steps were a more reliable measurement of URC current over a range of cell voltages. Experimental parameters are provided separately for each experiment throughout the manuscript.

Current density within data figures was based on geometric area of the electrode. Small changes in foam geometry can result in large real surface area differences. Therefore, all electrochemical data reported in a figure on Ni foam-based catalysts were obtained from the same foam-based WE to ensure that the real electrode surface area remained consistent between scans. Additionally, the active electrochemical surface area (ECSA) was estimated using the blank anodic scan charge according to Equation 3.2, where Q is the total charge measured for the anodic Ni^{2+}/Ni^{3+} peak during a blank electrode scan at 10 mV/s, and $q = 257$ μC/cm^2, the specific charge of $Ni(OH)_2$ monolayer formation [86, 92].

$$\mathrm{ECSA} = \frac{Q}{q} \tag{3.2}$$

3.4.3 *Solution Composition*

Composition of the URC anode feed solution was measured throughout longer experiments in which solute concentration was changing, sometimes significantly. A blood urea nitrogen (BUN) assay was performed using a clinical chemistry analyzer (Beckman Coulter, AU680) in a collaborating lab. A BUN assay measures the mass of atomic nitrogen, due to urea, within a certain volume of sample. Clinically, BUN assays are often performed on blood samples;

however, BUN measurements are a valid method of determining urea concentration in other neutral samples that contain urea including urine, saliva, and dialysate. The conversion from BUN (mg/dl) to urea concentration (C_u, mmol) is calculated using Equation 3.3, derived based on the presence of two N atoms per urea molecule, $(NH_2)_2CO$.

$$C_u = 0.357 \times \mathrm{BUN} \tag{3.3}$$

Nickel concentration measurements were performed on samples to quantify chemical dissolution and electrochemical corrosion processes of the URC anode. Atomic Ni (II) concentration measurements were performed on an inductively coupled plasma optical emission spectrophotometer (ICP-OES, Perkin Elmer Optima 8300) at a wavelength of 231.604 nm. The instrument was controlled, and data were collected using ICP software (WinLab 32, Windows 7). During each ICP measurement, a pure water blank, a reagent blank, and five Ni standard concentrations (1.0 µl – 1.0×10^5 µl) were analyzed prior to analysis of URC anolyte samples, in triplicates. As a result, Ni contamination in water and reagents was accounted for, and a standard concentration curve ($R^2 > 0.999$) was confirmed.

Chapter 4. UREA OXIDATION ON PLATINUM

4.1 POTASSIUM HYDROXIDE ELECTROLYTE

A clean Pt surface produces multiple electrochemical peaks when scanned between 0 and 1.6 V vs. RHE (Figure 4.1). Hydrogen evolution occurs below 0 V vs. RHE and OER occurs above 1.6 V vs. RHE. These peaks vary in position and size based on the background electrolyte. Figure 3.1 and Table 4.1 provide an overview of each peak location and relative size in 0.1 M KOH and scan rate (ν) of 20 mV/s. The electrochemical processes listed in Table 4.1 are named throughout this chapter to discuss how the peaks captured on a Pt surface in alkaline media change with the presence of urea. Oxidation peaks are positive on the current density (j) axis, and reduction peaks are negative. Electrochemical cleaning of Pt electrodes, after polishing smooth with alumina, is performed by fast cycling (ν = 100 mV/s) in this potential window until successive CVs are reproducible. A polished and electrochemically cleaned Pt surface is characterized by the hydrogen adsorption ($H_{ads,}$ peak f) and desorption (H_{des}, peak a) peaks in the range of 0–0.45 V vs. RHE (Figure 4.1).

Peak Label	Voltage Region (V vs. RHE)	Type of Current	Chemical Process
a	0.1–0.4 V	oxidation	H^+ desorption
b	0.6–0.9	oxidation	OH^- adsorption
c	0.9–1.5	oxidation	Pt-O formation
d	1.5 + V	oxidation	O_2 evolution
e	0.9–0.55 V	reduction	Pt-O reduction
f	0.4–0.1 V	reduction	H^+ adsorption

Table 4.1 Identification of electrochemical peaks a–f in Figure 4.1.

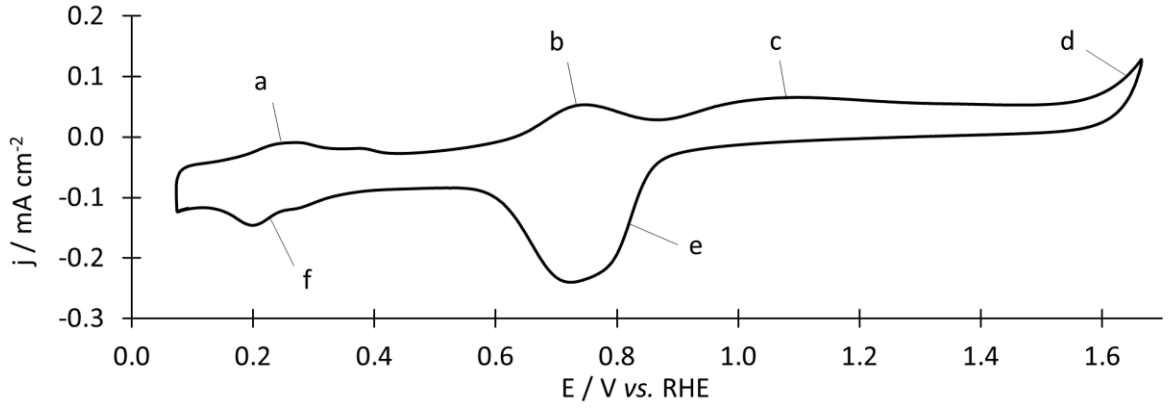

Figure 4.1 CV of a clean a Pt disk WE in 0.1 M KOH and ν =20 mV/s; peaks are defined in Table 4.1 based on electrochemical processes. Oxidation current is positive.

The peaks for each chemical process are affected by addition of urea to 0.1 M KOH (Figure 4.2). Figure 4.2 reveals urea oxidation beginning at 0.9 V vs. RHE, as observed by oxidation current that is more positive than that of the blank scan. This result indicates a large overpotential (η) for urea oxidation on Pt in 0.1 M KOH. Overpotential is an electrochemical driving force and is positive for oxidation reactions, defined by Equation 4.1 where $E(T,p)$ is the potential at which oxidation is observed, and $E^0(T,p)$ is the reversible potential for the reaction at the same temperature (T) and pressure (p). According to Reaction 2.2, E^0(25 °C, 1 atm) for UOR is –0.687 V vs. RHE at pH 13. Therefore, based on an observed oxidation at 0.9 V vs. RHE (Figure 4.2), η for UOR on Pt in 0.1 M KOH is 1.6 V. This substantial overpotential indicates that urea oxidation kinetics are slow on Pt in these conditions, and a large potential driving force is required for UOR to occur.

$$\eta = E(T, p) - E^0(T, p) \tag{4.1}$$

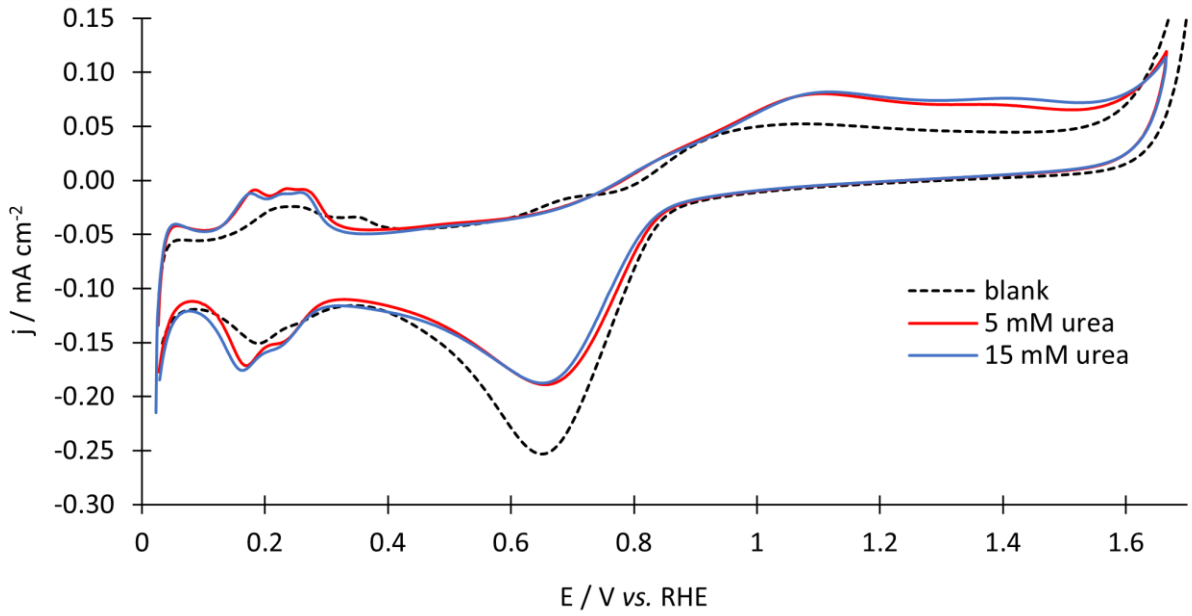

Figure 4.2 CVs of 0, 5, 15 mM urea in 0.1 M KOH, ν = 20 mV/s. Urea oxidation begins at 0.9 V vs. RHE. Presence of urea suppresses oxide reduction and OH^- adsorption current, while increasing H_{ads} and H_{des} current.

Figure 4.2 reveals urea oxidation continuing up to 1.6 V vs. RHE for both urea concentrations. Increasing the urea concentration from 5 to 15 mM results in a subtle increase in oxidation current in the range of 1.2–1.6 V vs. RHE. Urea adsorption competes with, and overtakes, the peak for OH^- adsorption. As a result, urea and OH^- adsorption, and subsequent urea oxidation and oxide formation, are difficult to decouple in CVs. An indication that UOR is suppressing Pt oxidation from 1.2–1.6 V vs. RHE is observed in the shifted Pt-O reduction peak. The oxide reduction peak in the presence of urea is less pronounced and positively shifted by about 10 mV, indicating that the passivating Pt-O layer is less developed in the presence of urea.

Presence of urea increases the current in the H_{ads}/H_{des} region and negatively shifts the peaks. The negative shift indicates that the hydrogen binding energy (HBE) is lower when urea is

present. This could be directly due to the presence of urea; a similar trend is seen where NH_3 lowers HBE of H on Pt [93]. Alternatively, NH_3 may be present due to possible reduction reaction of adsorbed atomic H and N. The E^0 for NH_3 formation under these conditions is –0.722 V vs. RHE, making the presence of NH_3 thermodynamically favorable in this potential region. Reduction of adsorbed N into NH_3 would contribute to the removal of adsorbed H and increase H_{des} current density. The replenishment of adsorbed H from the electrolyte would result in an increased H_{ads} current density.

Figure 4.3 approximates the urea electrochemical oxidation (EO) current by subtracting the blank CV from the 5 mM urea CV in Figure 4.2 within the urea oxidation potential region. The urea EO current is an approximation because it assumes that the presence of urea within the cell has no effect on Pt oxidation. This assumption conflicts with Figure 4.2 evidence for urea-induced Pt oxidation suppression. As a result, the urea EO current shown in Figure 4.3 may slightly underestimate true urea oxidation current in this region. The maximum current (j_{max}) is 0.03 mA/cm^2, which occurs at a potential (E_{max}) of 1.17 V vs. RHE.

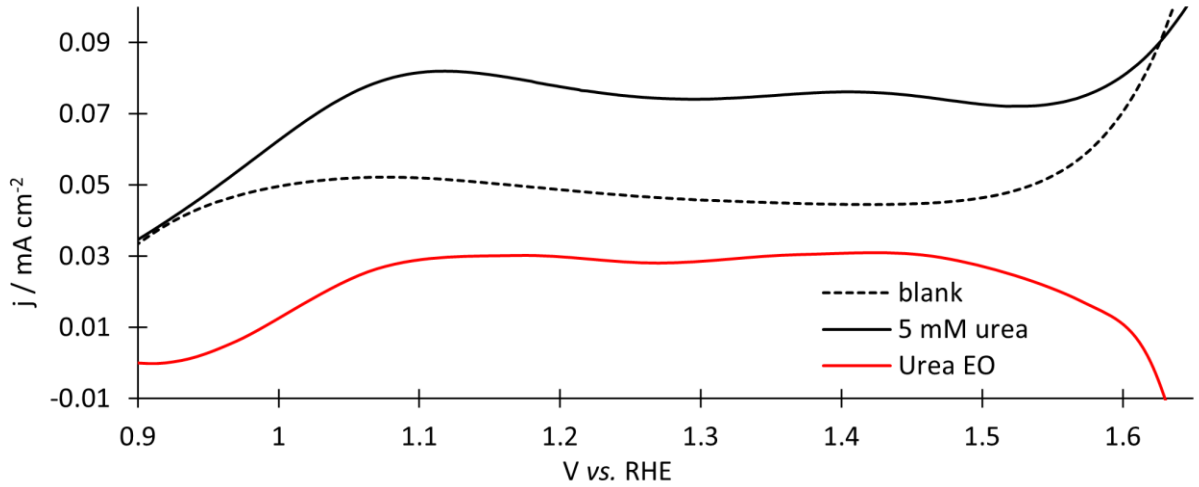

Figure 4.3 Red curve approximates urea electrochemical oxidation (EO) current as the mathematical difference between the 5 mM (black) and blank (black, dashed) data from Figure 4.2 in the urea oxidation region.

Figure 4.4 shows a series of CVs for 5 mM urea with upper potential limits of 1.27 V, 1.47 V, and 1.67 V vs. RHE. As the anodic limiting potential decreases, the oxide reduction peak becomes less defined and undergoes a positive shift, indicating the presence of a less developed Pt-oxide layer. This is similar to, and more pronounced than, the effect of urea concentration on Pt-O formation (Figure 4.2). A lower anodic potential limit promotes continued oxidation of urea upon the reverse scan; this effect is most obvious in the 1.27 V limit scan in the range of 0.9 to 1.27 V vs. RHE. It can be concluded that higher anodic potentials result in higher WE surface coverage by Pt oxides and, possibly, partial urea oxidation species. Urea presence decreases HBE, consistent with Figure 4.2. The intensity of H_{ads} increases with limiting anodic potential, while that of H_{des} is weakly correlated. This is evidence that the H_{ads} current involves species created by oxide formation and/or urea oxidation at higher limiting potentials. Additionally, the decrease in H_{des} reduction peak compared to the blank for both 1.27 and 1.47 limiting potentials indicates Pt surface blockage, perhaps due to adsorbed urea or partial oxidation products.

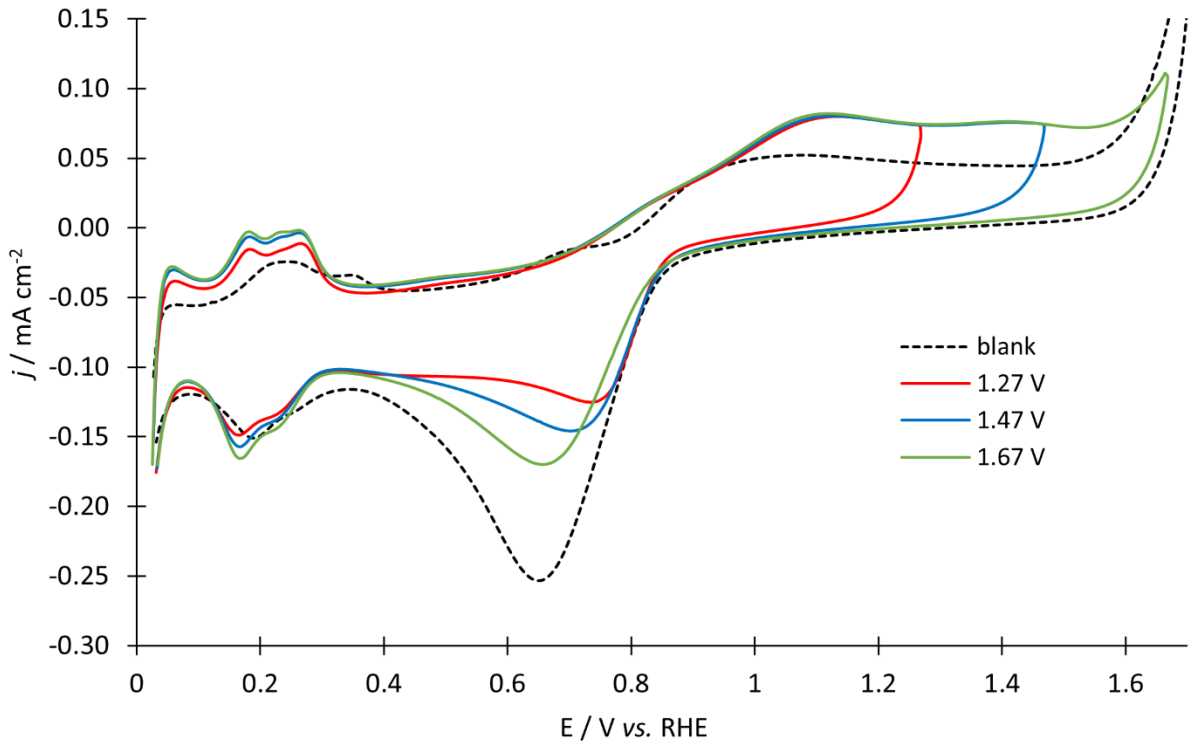

Figure 4.4 CVs for 5 mM urea with positive potential limits of 1.27, 1.47, and 1.67 V vs. RHE performed on Pt in 0.1 M KOH at ν = 20 mV/s. Reduced anodic limiting potentials result in suppressed oxide reduction and H_{ads} current and reduced η for Pt-O reduction.

Figure 4.5 show CVs for 5 mM urea in 0.1 M KOH with increasing lower potential limits, from 0.07 V to 0.97 V vs. RHE. Unlike previous CVs, which demonstrate stability in the potential scan region, increasing the cathodic potential limit suppresses the current observed for each successive scan through a process called *catalyst poisoning*. Therefore, a blank is provided for Figure 4.5a–d, and all data are from the second CV scan. Urea oxidation current decreases relative to the blank when a lower potential limit above 0.07 V vs. RHE is used, attributed to Pt poisoning due to oxide coverage. With a potential limit of 0.27 V vs. RHE (Figure 4.5b), the PtO is fully reduced, however H_{ads} and NH_x contribute to partial Pt surface coverage. As a result,

subsequent scans yield lower urea oxidation currents, and hence, a slower catalyst poisoning mechanism.

When the cathodic potential limit is further increased to 0.67 and 0.97 V vs. RHE (Figure 4.5c,d), the urea oxidation current does not surpass that of the blanks. This indicates that urea oxidation does not occur on Pt when existing oxides and partial oxidation products occupy Pt surface sites. Figure 4.5c,d demonstrate that the oxide layer on Pt is the primary deactivation mechanism for UOR, and Figure 4.5b shows that N_{ads} and other partial UOR surface species contribute to Pt poisoning to a lesser extent. These observations agree with deactivation mechanisms on Pt during ammonia oxidation [93].

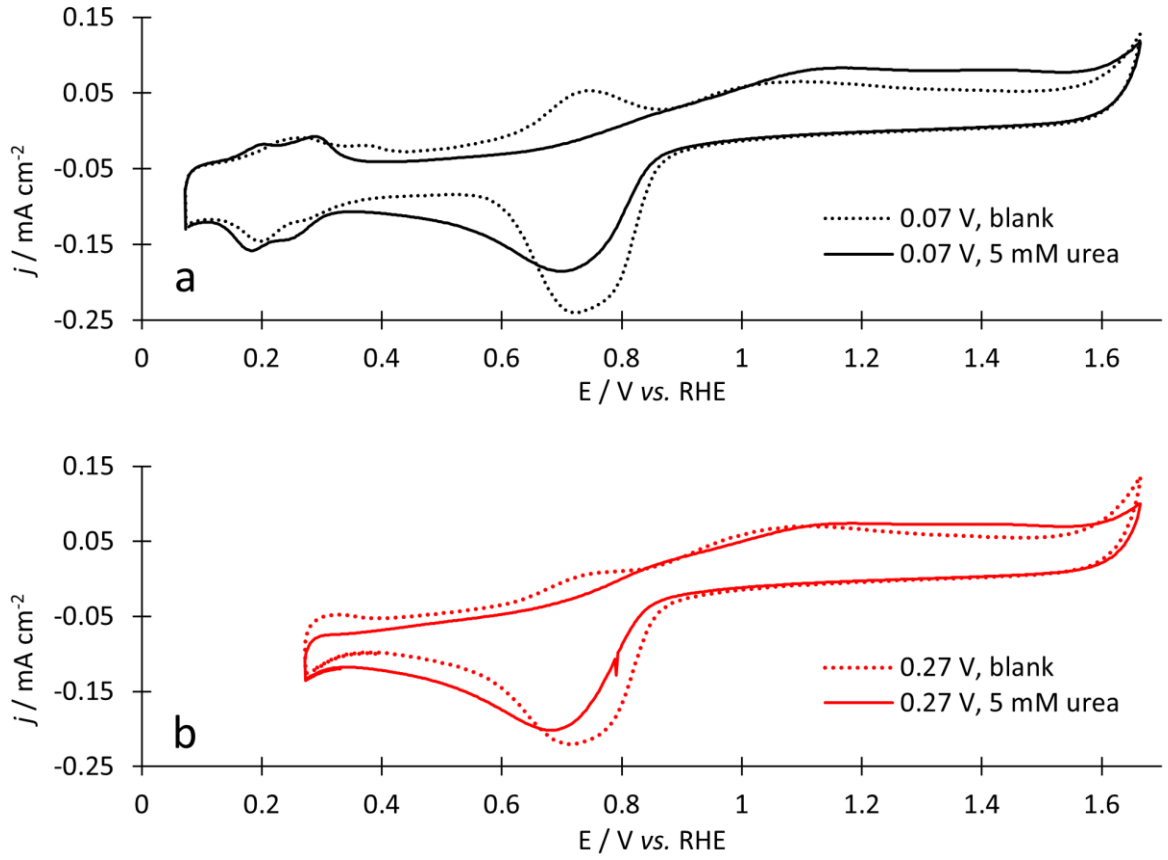

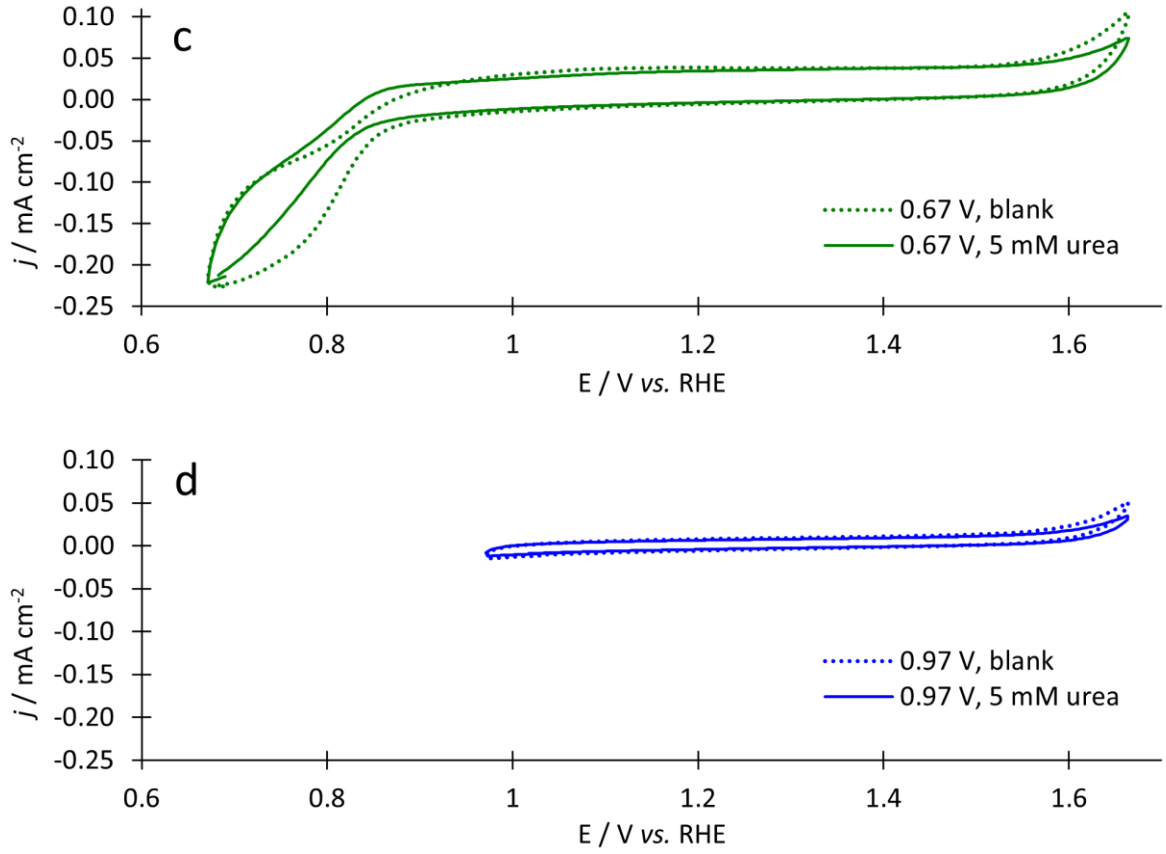

Figure 4.5 CVs for 0 and 5 mM urea in 0.1 M KOH with a lower potential limit of a) 0.07 V, b) 0.27 V, c) 0.67 V, and d) 0.97 V vs. RHE; ν = 20 mV/s for all scans.

The staircase voltammogram shown in Fig. 4.6 shows that extended urea oxidation on Pt in alkaline solution causes more severe Pt poisoning when potentials above 0.77 V vs. RHE are held at longer duration, in agreement with Figure 4.4 and Figure 4.5. Potential was stepped from 0.77 to 1.57 V vs. RHE in 0.2 V increments and each step was held for 10 minutes (Figure 4.6a). The first 600 s are not shown in Figure 4.6 because 0.77 V vs. RHE resulted in slight reduction current, in agreement with Figure 4.2. The order in which the experiments were conducted is important and is provided in Figure 4.6b legend. First, the blank (1) experiment was performed, immediately followed by 15 mM urea (2), and again immediately followed by 30 mM urea (3). At

all potentials, current density for 30 mM urea (3) was lower than that for 15 mM urea (2) due to oxide formation, as the cell was not brought below 0.77 V for 150 consecutive minutes. Furthermore, during the 1.57 V vs. RHE hold, the urea-containing solutions yield lower current density than that of the blank. Informed by the Pt inactivation studies discussed above, a regeneration procedure for the Pt electrode was performed by applying a potential of –0.1 V vs. RHE for one minute. As predicted, the Pt activity was regenerated, and the 30 mM urea post-regeneration (4) current density was increased at each potential above all other experiments.

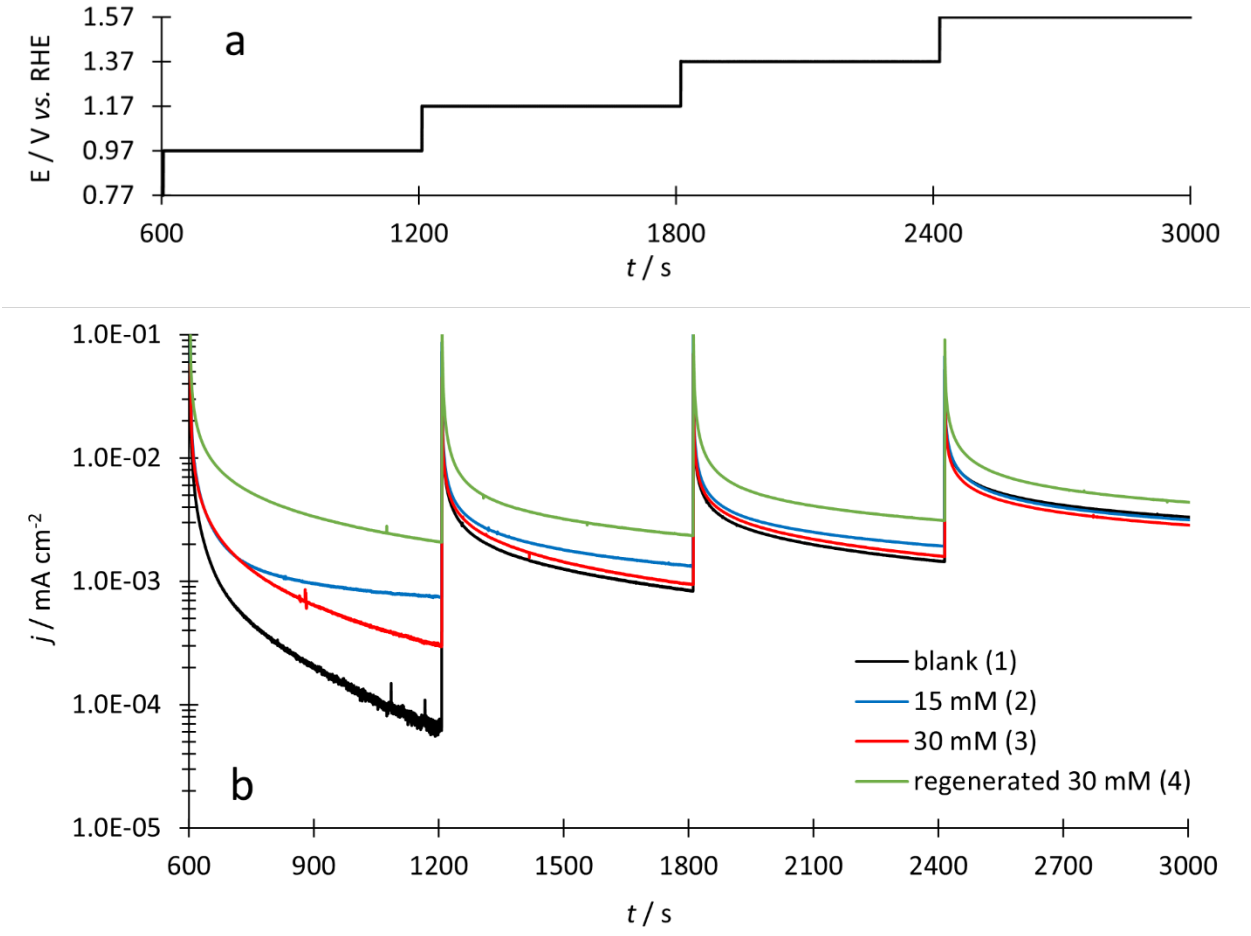

Figure 4.6 a) Applied potential and b) measured current response over 50 minutes for 0–30 mM urea in 0.1 M KOH. Numbers in legend correspond to succession of

experiments. Regeneration was performed by applying –0.1 V vs. RHE for 60 s after 30 mM (3) and before regenerated 30 mM (4).

Table 4.2 summarizes the thermodynamic and kinetic parameters of urea oxidation on a Pt catalyst in 0.1 M KOH. It is confirmed that urea oxidizes on Pt in alkaline solution between 0.9 and 1.6 V vs. RHE, which corresponds to an overpotential of 1.6 V. Urea oxidation current has a weak positive correlation with urea concentration, and a moderate negative correlation with Pt oxide accumulation. Urea oxidation suppresses PtO formation; however, exposure to higher potentials for longer durations causes Pt poisoning due to passivation and occupied catalytic surface sites. This deactivation mechanism is reversible, and the catalytic surface is regenerated with a short potential hold at an electrochemically reducing potential. Cyclic voltammetry and chronoamperometry studies demonstrate that sustained urea oxidation on Pt is not achievable without regeneration by a reducing potential, in agreement with a reactor design study that utilized electrode potential switching to regularly regenerate Pt activity [26]. Using j_{max} and Equation 4.2, a UOR mass reaction rate ($\hat{r}$) is calculated on Pt where n_e = 6 mole e^-/mole urea, F = 96,485 C/mole e^-, and M_u = 60 g/mole urea. Required electrode area, A, to oxidize 15 g urea/day (m_u, the average human body production rate of urea) is calculated using $\hat{r}$ and Equation 4.3. An assumption of 100% Faradic efficiency is used in the application of Equation 4.2, which results in overestimation of real $\hat{r}$ and underestimation of real A. Table 4.2 reports calculated $\hat{r}$ and A for Pt in alkaline conditions.

$$\hat{r} = \frac{j_{\max}}{n_e F} M_u \tag{4.2}$$

$$A = \frac{m_u}{rt} \tag{4.3}$$

Parameter	Measured Value	Source
E (25 °C, 1 atm)	0.9 V vs. RHE	Figure 4.2
η	1.6 V	Figure 4.2
j_{max}	0.03 mA/cm^2	Figure 4.3
E_{max}	1.17 V vs. RHE	Figure 4.3
$\hat{r}$	3.1×10^{-9} g/s·cm^2	Equation 4.2
A	5.6×10^{4} cm^2	Equation 4.3

Table 4.2 Summary of Pt catalytic thermodynamic, kinetic, and design parameters for UOR in 0.1 M KOH at 25 °C and 1 atm.

4.2 Sodium Chloride Electrolyte

Urea oxidation in neutral, chloride-containing media was briefly explored. Due to the highly alkaline AEM environment, the alkaline studies previously discussed received more focus. Neutral experiments were run using 0.1 M NaCl as the electrolyte (Figure 4.7). Chloride interactions on Pt are known to be complex [94], and as a result, the NaCl blank contains more dramatic features than the KOH blank (Figure 4.1). When urea is added into the cell, the features change drastically, likely due to the anodic oxidation of Cl^- into OCl^-, which results in the hypochlorite-mediated bulk urea oxidation mechanism (Reaction 2.1) [30]. Figure 4.7 reveals that urea oxidation on Pt in 0.1 M NaCl has observed UOR onset at 1.25 V vs. RHE and j_{max} remains the same as alkaline UOR at 0.03 mA/cm^2. However, overall urea oxidation rate is likely higher in the chloride solution due to the concurrent chemical oxidation of urea by OCl^- which is not captured in j_{max}.

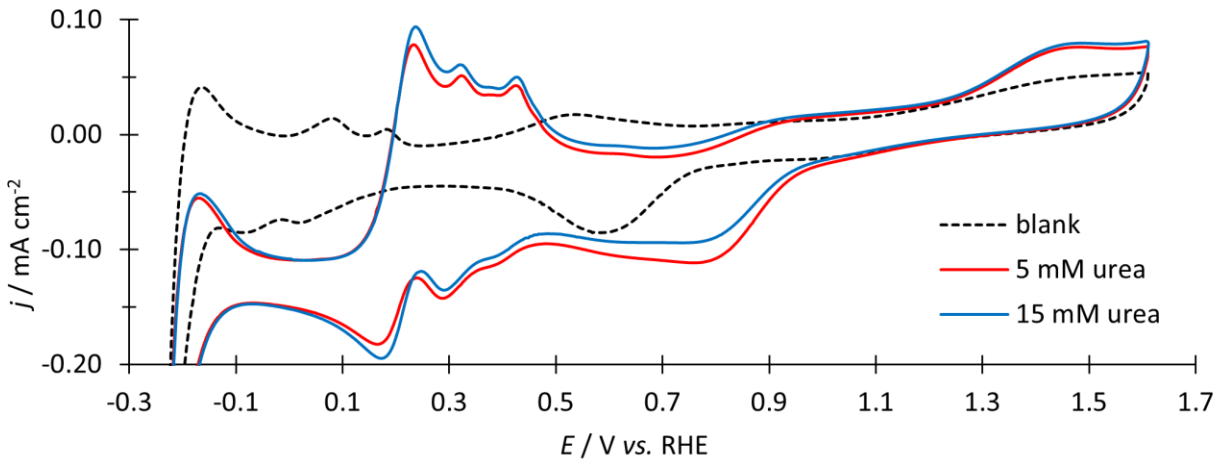

Figure 4.7 CVs for 0, 5, 15 mM urea in 0.1 M NaCl on a Pt disk electrode with ν = 20 mV/s.

Chapter 5. UREA OXIDATION ON NICKEL

The reactor electrode area calculated for a Pt electrode is larger than a portable device can realistically deliver. Higher catalyst activity enables compact reactor design, and while Pt has been the primary catalyst used in dialysate regeneration devices, more recent research demonstrates the exceptional performance of Ni towards urea electrooxidation. This section summarizes exploration of a variety of Ni-based electrode types including sputtered and electrodeposited upon glassy carbon, and commercially available Ni disk, all with geometric areas of 0.07 cm^2 (Table 3.1). Glassy carbon electrodes (GCE) were used as supporting substrate due to their low reactivity yet high electrical conductivity. Kinetic studies require precise knowledge of electrode area and therefore were performed on purchased Ni disk WEs due to the well-defined, reproducible surface area achieved by polishing.

Nickle is an important, cheap catalyst used in an array of electrochemical systems, most notably batteries. Nickel's classification as a transition metal enables the formation of multiple types of oxides and hydroxides in an aqueous environment, which gives rise to its unique electronic properties [25]. Independently, nickel is found to be an essential co-factor for urease to hydrolyze urea [11, 52].

Each urease active site requires the presence of two Ni^{2+} ions that must be transported into the cell. Within the urease binding pocket, the urea molecule is understood to bind to the Ni^{2+} sites via the carbonyl and one amine group [95]. A transition state forms as the carbonyl

double bond breaks and a bond between the enzyme and urea carbon forms. The hydrolysis mechanism is enzymatic and therefore fundamentally distinct from electrocatalytic urea oxidation reaction; however, the shared ability for urease and Ni-based electrocatalysts to enhance urea reaction may be contingent on the binding energies of Ni in its various valence states.

5.1 Sputtered Nickel Working Electrode

In collaboration with the Hinds research group (UW, Materials Science & Engineering), the first Ni catalyst obtained for testing was a sputtered Ni metal WE. The sputtered Ni WE did not withstand complete testing; however, early electrochemical results for UOR were promising when compared to Pt, as shown in Figure 5.1. The Pt current density shown in Figure 5.1 has been scaled by χ =20 for comparison on the same *j* scale. The Ni blank reveals an anodic peak at 1.44 V vs. RHE and a cathodic peak at 1.13 V vs. RHE, attributed to the oxidation and reduction of $Ni(OH)_2$ (Ni^{2+}) and NiOOH (Ni^{3+}), respectively (Reaction 5.1). This reversible transition dictates the valence state of Ni within the UOR potential region and plays an important role in Ni catalysis for organic molecules [58, 96]. The reversible potential for Reaction 5.1 is 1.26 V vs. RHE at pH 13, in agreement with what is seen in Figure 5.1. Increase in oxidation current at potentials greater than the local minimum at 1.4 V vs. RHE is due to OER. When 5mM urea is present, the increased oxidation current above the blank between the Ni^{2+} oxidation and OER peaks is attributed to UOR. Urea oxidation above the blank is also observed on the reverse scan and the subsequent Ni^{3+} reduction peak is smaller because UOR reduced some Ni^{3+} sites, leaving fewer sites to be reduced compared to the blank.

$$Ni(OH)_{2(s)} + OH^-_{(aq)} \rightleftarrows NiOOH_{(s)} + H_2O_{(l)} + e^- \quad (5.1)$$

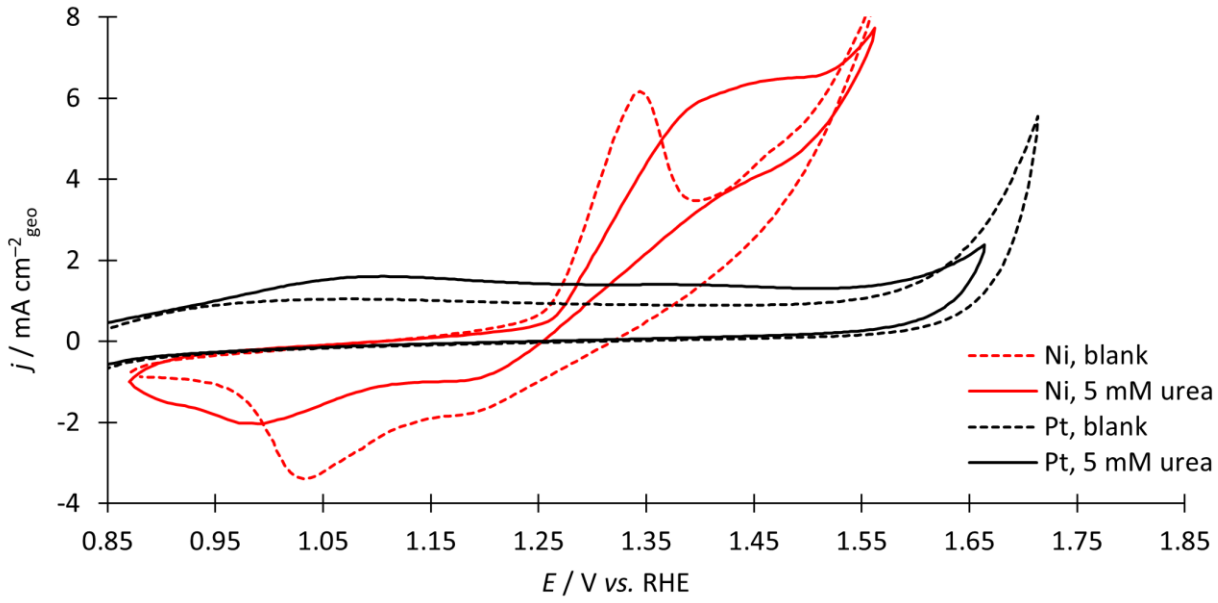

Figure 5.1 Comparison of CVs during urea oxidation on Pt (black) and Ni (red) in 0.1 M KOH at v= 20 mV/s. Pt data has been scaled by χ = 20. Current density, j, is based on geometric area.

Nickel hydroxide oxidation and urea oxidation are competing reactions at potentials above 1.26 V vs. RHE. Unlike adverse PtO formation, $Ni(OH)_2$ oxidation creates Ni^{3+} catalytic sites for urea to react upon and therefore is required for UOR. This is evident in Figure 5.1, as oxidation onset for UOR coincides with Ni^{2+} oxidation. While it is difficult to decouple Ni^{2+} oxidation from UOR, Figure 5.1 shows j_{max} for UOR on Ni that is about two orders of magnitude larger than for Pt. To account for roughness of the sputtered Ni electrode, the ECSA (Equation 3.2) calculation reveals a roughness factor (RF) of 9 compared to a smooth Ni surface. Taking this RF into account, the Ni catalyst remains substantially more active towards UOR compared to Pt. The increased activity of the Ni WE is accompanied by a larger η for urea oxidation. The observed oxidation

potential E(25 °C, 1 atm) is 1.35 V and defined as the potential at which the CV for 5 mM urea reaches 1 mA/cm^2. The resulting η is 2 V, a significant 0.4 V increase compared to Pt.

In pursuit of developing a portable reactor to remove urea, the kinetic advantage of a Ni catalyst for UOR is desirable, even when thermodynamic inefficiencies are accounted for. Although the sputtered Ni WE delaminated with further electrochemical testing, the high activity of Ni towards UOR motivated alternative Ni WE fabrication methods.

5.2 Electrodeposited Nickel Working Electrodes

To electrochemically deposit Ni WEs, a Ni^{2+} salt solution (Table 5.1) was stirred at room temperature while a negative potential (E_{hold}) was applied to the GCE substrate to induce alkaline HER (Reaction 5.2, E^0 = – 0.199 V vs. Ag/AgCl). The OH^- produced at the GCE surface reacts with Ni^{2+} and precipitates $Ni(OH)_2$ (Reaction 5.3) [25]. During electrodeposition, HER was visually confirmed by bubble formation. Additionally, Ni^{2+} is directly reduced into Ni metal (Reaction 5.4, E^0 = –0.456 V vs. Ag/AgCl). At the deposition potentials used, (E_{hold} < –0.9 V vs. Ag/AgCl, Table 5.1) HER kinetically dominates to primarily deposit $Ni(OH)_2$. Film thickness was controlled based on total reduction charge passed. Multiple deposition environments were explored (Table 5.1) [25, 97, 98]. Variations include total film thickness (between 0.33 and 1 µm), deposition potential (between –1.0 V and –0.9 V vs. Ag/AgCl), and salt solution (Ni^{2+} concentration and supporting buffers). Electrodeposition resulted in a reflective "mirror" $Ni(OH)_2$ finish, which confirms a smooth surface. The phase and crystallinity of the resulting catalyst layer is dependent on the nature of the salt bath, the current density, and substrate.

Figure	$[Ni^{2+}]$ (mol L^{-1})	[Electrolyte] (mol L^{-1})	E_{hold} (V vs. Ag/AgCl)	Thickness (μm)
Figure 5.2a	0.5	Sodium Citrate: 0.26	– 1.0	0.33
Figure 5.2b	0.7	Sodium Citrate: 0.26	–0.9	1.0
Figure 5.3	0.1	Boric acid:0.5 Sodium sulfate: 1.0	–0.9	0.33
N/A	0.1	Boric acid:0.5 Sodium sulfate: 1.0	–1.0	0.33

Table 5.1 Matrix of electrodeposition conditions used for $Ni(OH)_2$ electrodes in Figure 5.2 and Figure 5.3; Ni^{2+} ions provided by $NiSO_4 \cdot 6H_2O$.

$$2H_2O_{(l)} + 2e^- \rightarrow H_{2(g)} + 2OH^- \quad (5.2)$$

$$Ni^{2+} + 2OH^- \rightarrow Ni(OH)_{2(s)} \quad (5.3)$$

$$Ni^{2+} + 2e^- \rightarrow Ni_{(s)} \quad (5.4)$$

It has been widely reported that NiOOH is the active catalytic site for oxidation of organic molecules [58, 67, 68]. Nickel hydroxide electrode activation is therefore commonly performed to increase Ni^{3+} surface sites [57, 59]. Nickle hydroxide activation was performed by cycling electrode potential between 0.2 and 0.75 V vs. Hg/HgO at ν = 15 mV/s for 20–80 cycles. Figure 5.2 and Figure 5.3 show activation CVs for electrodes deposited using the conditions listed in Table 5.1. All electrodes exhibit the Ni^{2+}/Ni^{3+} redox couple with peak currents that increase with number of activation cycles performed. Four distinct Ni oxides (α-$Ni(OH)_2$, β-$Ni(OH)_2$, β-NiOOH, and γ-NiOOH) are observed in the electrodeposited electrodes and labeled in Figure 5.2a [25, 99]. The less positive and more positive anodic peaks are due to oxidation of α-$Ni(OH)_2$ and β-

$Ni(OH)_2$, respectively [99]. The β-$Ni(OH)_2$ phase is more stable and therefore is generally favored at higher cycles numbers (Figure 5.2b, Figure 5.3a). Two cathodic peaks are assigned to β-NiOOH (less positive) and γ-NiOOH (more positive), with the latter formed in response to electrode aging, over charging, and material strain [99]. The higher current density observed in Figure 5.2b is attributed to a thicker deposition layer. Figure 5.3a,b shows the same electrode before and after experimental use for UOR to demonstrate the effects of electrode aging. Although the catalyst crystalline phase evolves with activation and electrode use, the aging mechanisms agree with previous Ni electrocatalysis research and electrodeposited WEs exhibit enough stability to perform UOR.

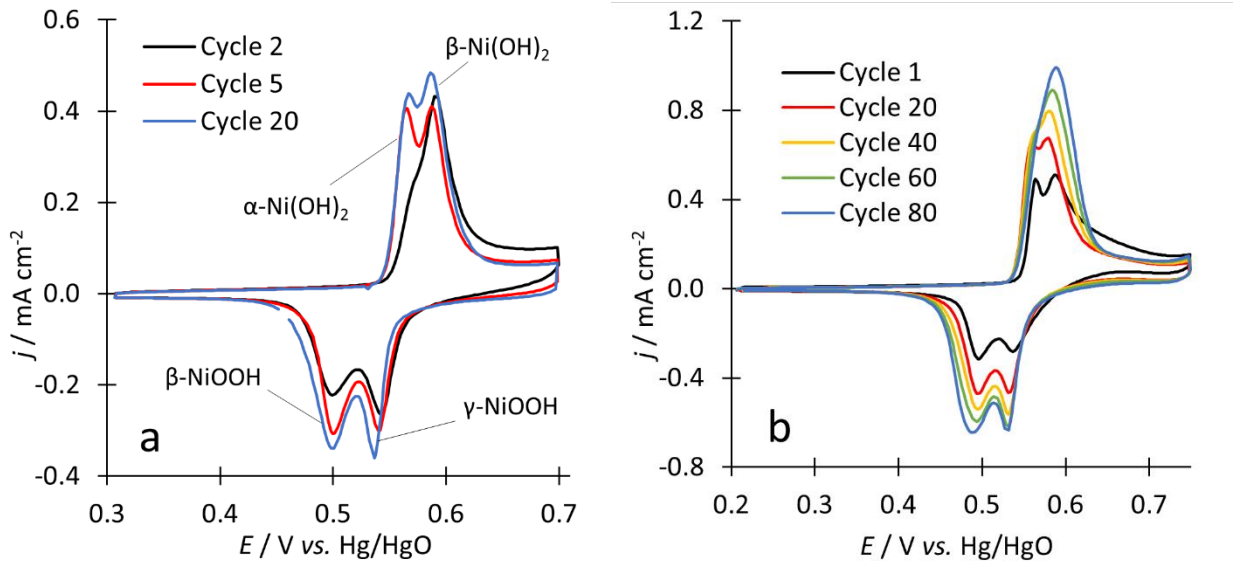

Figure 5.2 CVs showing activation cycles performed on $Ni(OH)_2$ electrodeposited WEs, in 1.0 M KOH and at ν = 15 mV/s. (a) All four Ni oxide peaks (labeled) are enhanced over 20 cycles, and (b) initially both α-$Ni(OH)_2$ and β-$Ni(OH)_2$ exist but stabilize entirely to β-$Ni(OH)_2$ with cycling.

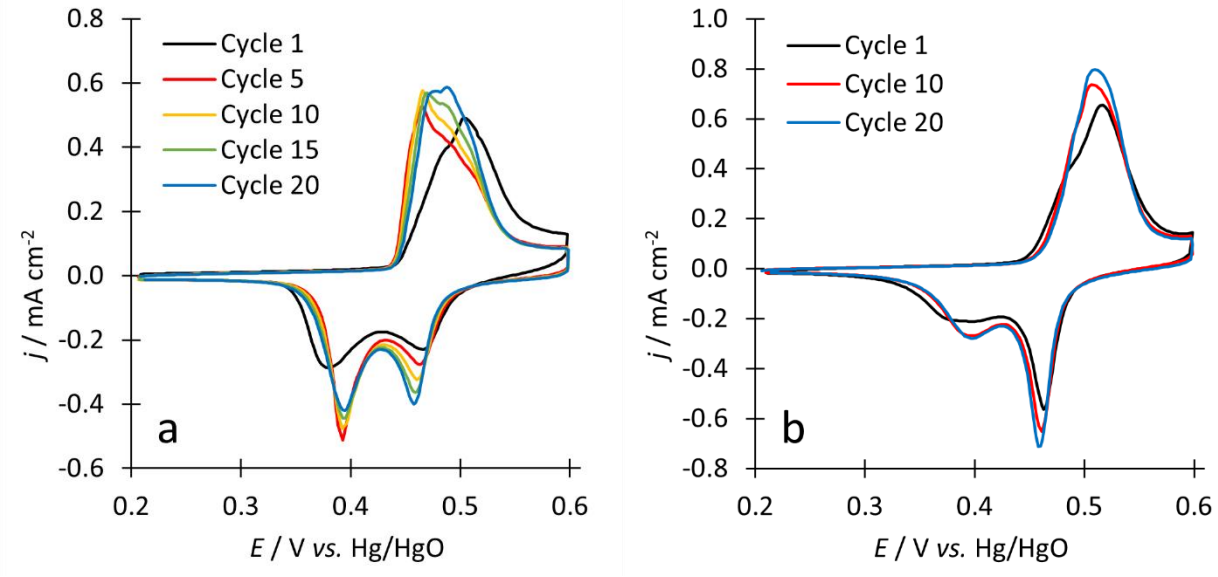

Figure 5.3 $Ni(OH)_2$ electrode activation performed in 1.0 M KOH at ν = 15 mV/s (a) before, and (b) after use for UOR experiments. Peaks initially favor α-$Ni(OH)_2$ and β-NiOOH with cycling and aging resulting in primarily β-$Ni(OH)_2$ and γ-NiOOH.

Cyclic voltammetry in a 15 mM urea and 0.1 M KOH performed on an activated $Ni(OH)_2$ WE is shown in Figure 5.4 and exhibits a more distinct UOR peak compared to the sputtered Ni WE. The current density is not directly comparable to that in Figure 5.1 due to differences in urea concentration and RF. Urea oxidation peaks are observed on forward and reverse scans at 0.64 V vs. Hg/HgO. The peaks at 0.49 V vs. Hg/HgO (reduction) and 0.55 V vs. Hg/HgO (oxidation) are due to the $Ni^{2+/}Ni^{3+}$ couple. Oxygen evolution begins about 0.78 V vs. Hg/HgO.

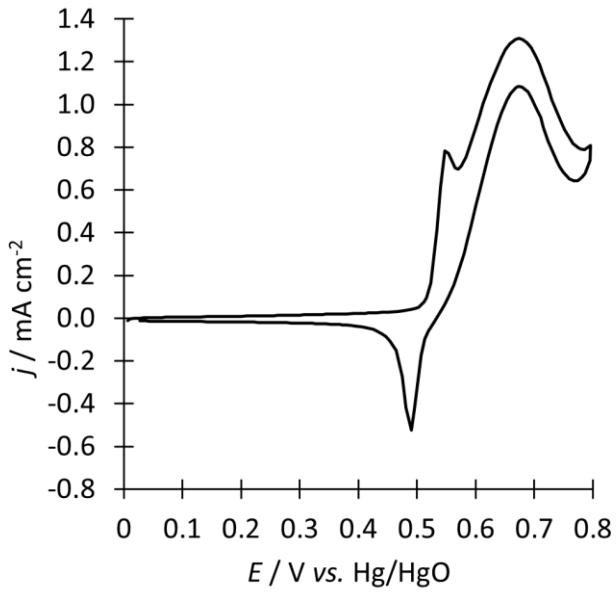

Figure 5.4 CV performed on activated electrodeposited $Ni(OH)_2$ WE in 0.1 M KOH and 15 mM urea at ν = 15 mV/s.

The increase in the oxidation peak current during electrode activation indicates more prevalent Ni^{3+} sites [62], which is confirmed by improved UOR rates. Figure 5.5 shows CAs of 15 mM urea before and after activation, compared to the blank. All CAs were performed in 0.1 M KOH for 10 minutes at 0.65 V vs. Hg/HgO. The activated $Ni(OH)_2$ WE shows a 53% increase in oxidation charge passed after 10 minutes and exhibits a more stable current density compared to its pre-activated state.

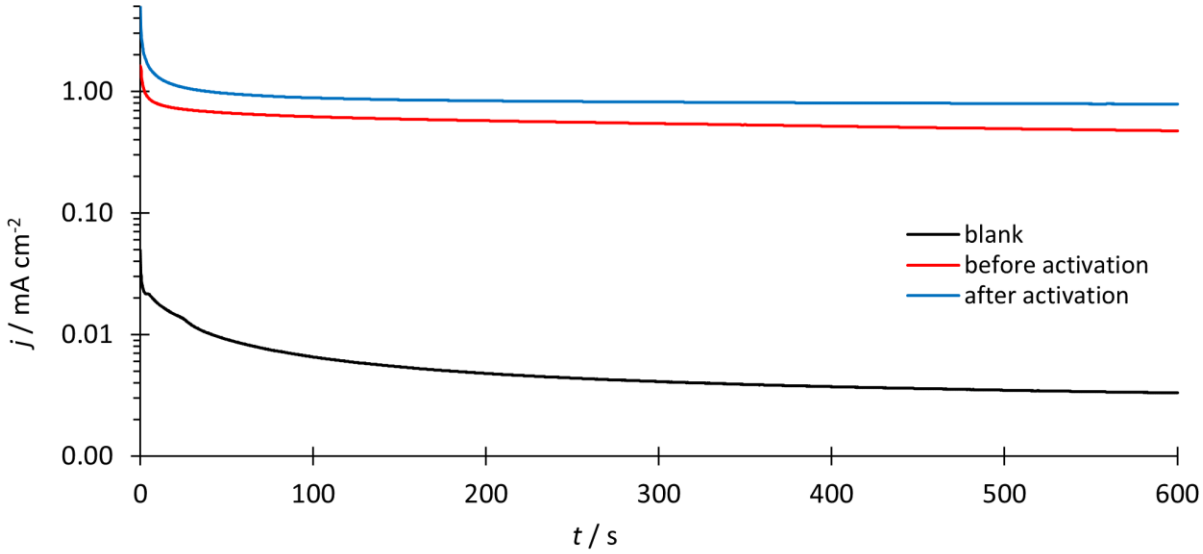

Figure 5.5 Chronoamperograms (CA) of 15 mM urea in 0.1 M KOH at E_{hold} = 0.65 V vs. Hg/HgO for 10 minutes. Terminal charge density above the blank is 50% higher on activated surface than pre-activated when 15 mM urea is present. Activated surface also exhibits more stability toward oxidation.

To understand the effect of temperature on the oxidation of urea, a series of CVs were performed at 23–35 °C on an activated Ni electrode. The forward scan for each CV is shown in Figure 5.6, with an inset to observe how oxidation onset changes with temperature. Increasing the solution temperature from 23 °C to 35 °C decreased the oxidation onset by 18 mV, and increased j_p from 2.2 mA/cm^2 to 7.5 mA/cm^2. An Arrhenius plot of the reaction rate (Figure 5.7a, where n_e = 6, F = 96,485 C/ mole e^-) in the potential range of 1.38–1.42 V vs. RHE shows two linear regions, evidence of two difference activation barriers. An activation barrier of 163 kJ/mole was found for the temperature range of 23–27 °C that decreases to 70 kJ/mol for 27–35 °C. Therefore, narrow temperature increases from 23–27 °C have a larger effect on UOR rate than further increase to 35 °C. This temperature effect is evident in the prolonged increase in reaction

rate for 20 mM urea during CAs at 1.43 V vs. RHE (Figure 5.7b). The current density at 600 s (j_{600}) for 29 °C is nearly double that for 23 °C; and j_{600} for 35 °C is more than triple the room temperature condition (Table 5.2). Based on these results, it is concluded that moderate heating of urea solutions to a physiological temperature of 37 °C enhances UOR in alkaline media.

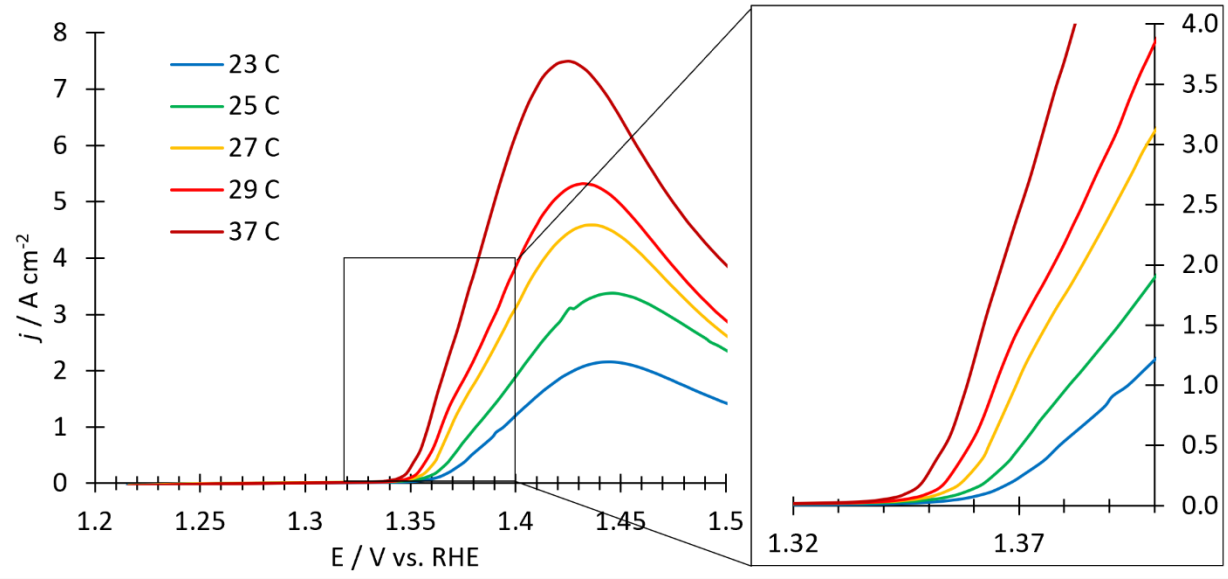

Figure 5.6 CVs of 20 mM urea in 5 M KOH from 23–35 °C collected at v = 20 mV/s.

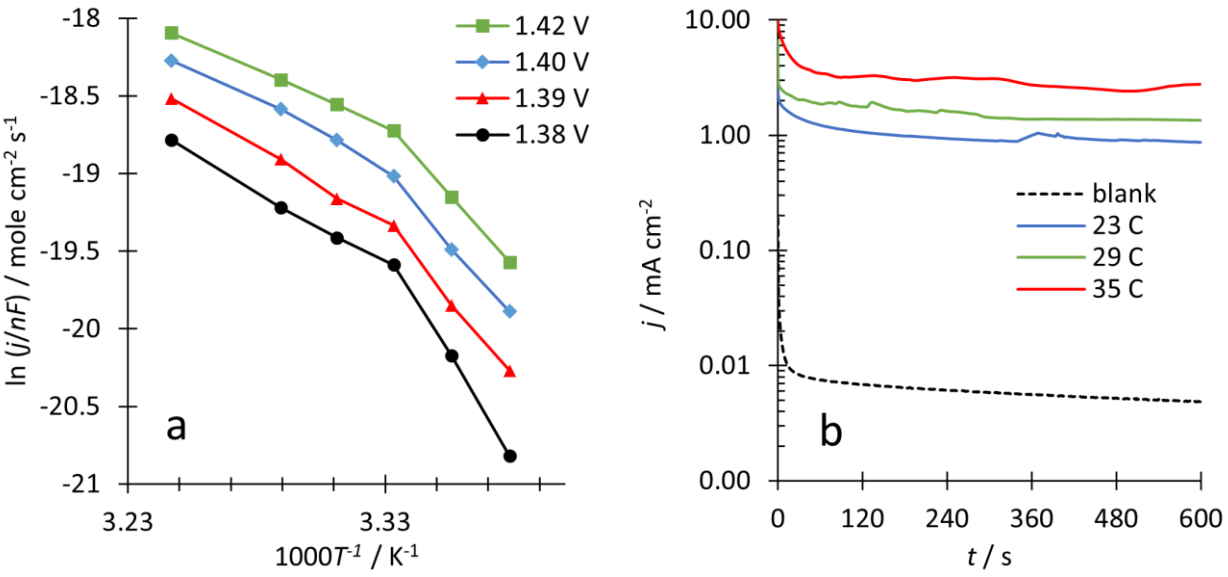

Figure 5.7 a) Arrhenius plot for CVs in Figure 5.6 at 1.38–1.42 V vs. RHE and b) CAs of 20 mM urea in 5 M KOH at 23–35 °C at 1.43 V vs. RHE.

T (°C)	j_{600} (mA/cm^2)
23	0.86
29	1.35
35	2.78

Table 5.2 Current density at t = 600 s (j_{600}) for CAs of 23, 29, and 35 °C, extracted from Figure 5.7b.

Most of the recent literature regarding urea oxidation is motivated by urea fuel cells or wastewater remediation where urea concentrations are 0.33 M or greater. This is more than 30x more concentrated compared to spent dialysate fluid with a typical 10 mM urea concentration. Low concentrations of urea and highly active electrodes can lead to mass transfer limited conditions. When urea is consumed at an electrode surface faster than urea in the solution can replenish the surface concentration, the system is referred to as *diffusion controlled*. Under such conditions, the depletion layer grows with time and the concentration gradient across the depletion layer is the driving force for diffusion. Low bulk urea concentrations minimize the driving force for diffusion and can create a mass-transport limited environment where current density is described by the Cottrell Equation (Equation 5.1). Mathematically, diffusion limited current density, $j(t)$, is proportional to $t^{-0.5}$ by a proportionality constant that depends on n_e = 6 mole e^-/mole urea, F = 96,485 C/mole e^-, the bulk concentration of urea (C), and the diffusion coefficient of urea (D) [100].

$$j(t) = \frac{n_e F C \sqrt{D}}{\sqrt{\pi t}} = \frac{m}{\sqrt{t}} \tag{5.1}$$

To study whether urea is diffusion limited in the dialysate concentration regime, chronoamperometry was performed at 0.61 V vs. Hg/HgO for 0, 5, and 15 mM urea in 0.1 M KOH (Figure 5.8a). The linear dependence of current density on $t^{-0.5}$ for both 5 and 15 mM urea (Figure 5.8b) provides evidence for diffusion-controlled urea oxidation under the experimental conditions. The slope (m) for each urea concentration is included in Figure 5.8b; that of 15 mM urea is about three times greater than the 5 mM urea solution, as predicted by the concentration difference. Using Equation 5.1 and the measured slopes at each concentration, the diffusion coefficient for urea in 0.1 M KOH at 22 °C is calculated to be $D = 3.15 \times 10^{-7}\,\mathrm{cm^2/s}$. This is about two orders of magnitude lower than the measured diffusion coefficient of urea in water at 25 °C and 0.125 M [101]. The discrepancy may be due to the presence of 0.1 M KOH and hydrogen bonding which occurs for both the OH^- and urea solutes. At high concentrations, urea is observed to self-associate in water into clusters of up to 60 urea molecules [102]; however, due to the low concentrations of urea in Figure 5.8, urea self-association is not predicted to be a reason for low diffusion coefficient. A density functional theory study concludes that while cyclic urea dimers can associate in water, they degrade rapidly to form structures where urea is linked through water molecule bridges [103]. These findings, however, cannot describe the two orders of magnitude difference in measured diffusion coefficient between this study and that of Gosting and Akeley [101]. It is not clear what is responsible for the exceptionally low diffusion coefficient in this study. Based on results shown in Figure 5.8, is it is confirmed that the oxidation of urea is mass transport limited at conditions relevant for dialysate regeneration. These initial studies

motivated a more complete analysis of the kinetics of UOR on a Ni surface, discussed in the following section.

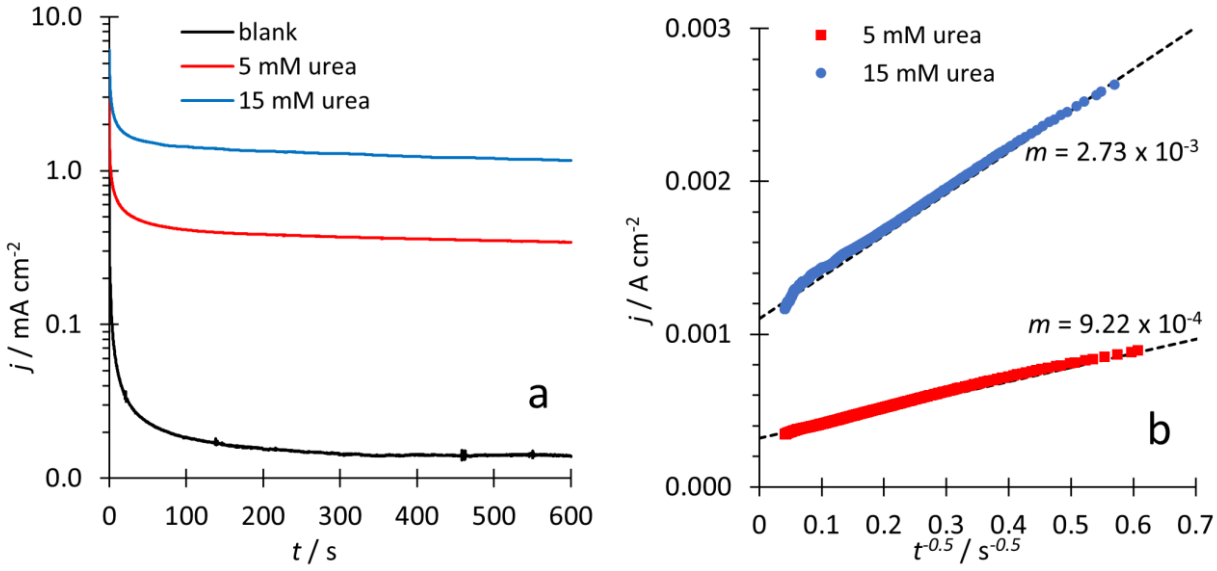

Figure 5.8 a) CAs preformed for 0, 5, and 15 mM urea in 0.1 M KOH exhibit diffusion limited decay as demonstrated by the b) linear dependence on $t^{-0.5}$ (Equation 5.1).

5.3 Kinetic Studies on Nickel Disk Working Electrodes

Kinetic studies of urea electrocatalysis on Ni were performed on disk WEs purchased from Basi that were polished between each experiment to ensure a clean, smooth, and reproducible surface. Additionally, to avoid mass transport limitations, kinetic studies included urea concentrations 0–1 M, and all were performed in 1 M KOH. Figure 5.9a shows a blank CV on a Ni WE with well-defined Ni^{2+}/Ni^{3+} peaks. The blank is also included in Figure 5.9b for comparison to urea containing scans. Figure 5.9b shows CVs of 0, 1, 10, 100, and 330 mM urea at ν = 10 mV/s.

The peak current density (j_p) increases with urea concentration, as expected, and a leading oxidation edge is shared by the higher concentration solutions. The 1 mM urea solution is diffusion limited as observed by its deviation from the leading oxidation edge as reaction outpaces urea diffusion to the surface. Once j_p is reached on the forward scan, the current density decreases to a local minimum before OER onset begins past about 0.65 V vs. Hg/HgO. On the reverse scan, a less intense UOR peak, compared to j_p, is observed for each concentration. And for the non-diffusion limited currents, oxidation continues in the reverse scan through about 0.46 V vs. Hg/HgO at current densities higher than the leading edge on the forward scan. This "crossover" of UOR in urea solutions with concentrations of 10 mM and higher is understood by assessing the coverage of Ni^{3+} catalytic surface sites in the voltage range scanned, discussed below.

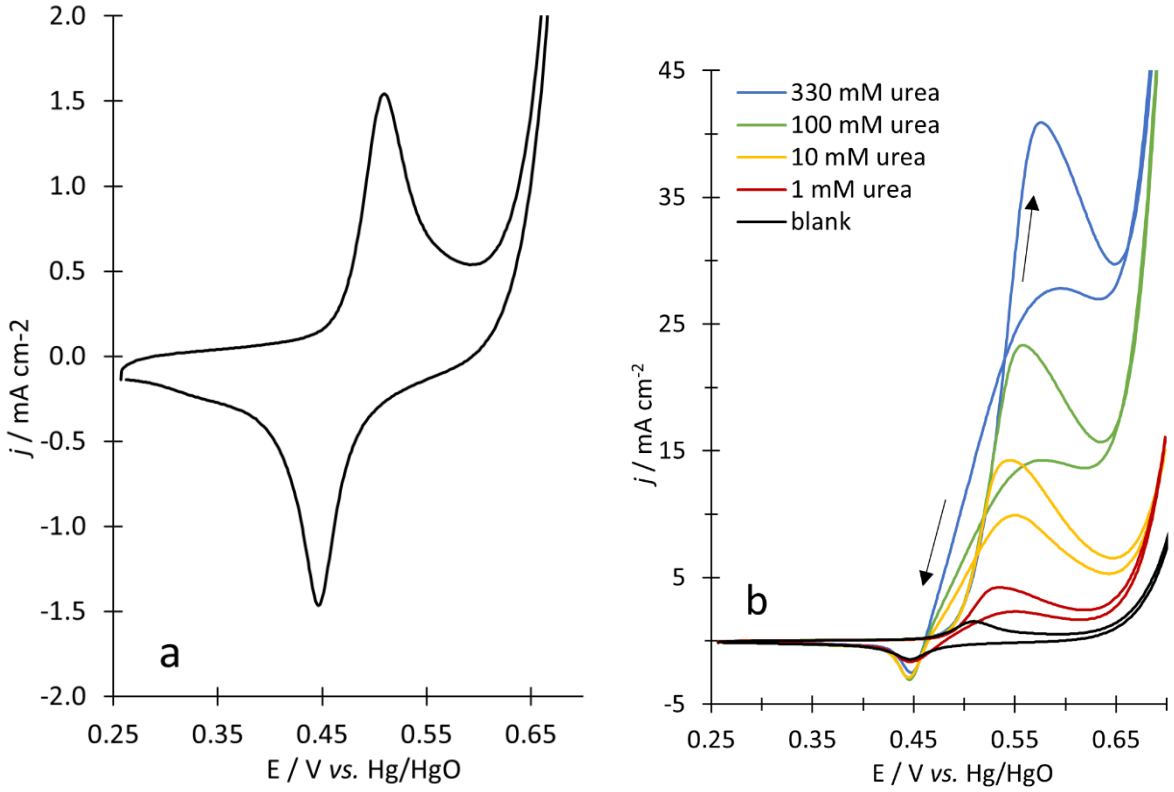

Figure 5.9 CVs of a) 0 mM urea and b) 1–330 mM urea in 1 M KOH on a Ni disk WE, ν = 10 mV/s. Arrows indicate oxidation current direction on the forward scan (high) and reverse scan (low).

To explore how UOR depends on the surface oxidation of $Ni(OH)_2$, the surface coverage of NiOOH ($\theta_{Ni^{3+}}$) is calculated using Equation 5.2, where Q_{blank} is defined by Equation 5.3. Figure 5.10a shows Q_{blank} as a function of electrode voltage (E) with Q'= 870 μC/cm^2 labeled to denote the charge passed on the Ni WE prior to OER onset, at E =0.60 V vs. Hg/HgO, represented by a positive inflection in Q_{blank}. As a result, $\theta_{Ni^{3+}}$ is dimensionless and nonlinear with E (Figure 5.10a). Figure 5.10b plots the current density for each urea concentration as a function of $\theta_{Ni^{3+}}$. For each concentration, UOR onset begins at $\theta_{Ni^{3+}}$ =0.08, which corresponds to E = 0.46 V vs. Hg/HgO. This finding agrees with the crossover effect observed in Figure 5.9b. Upon visualizing current density against the $\theta_{Ni^{3+}}$ scale used in Figure 5.10b, it is evident that UOR oxidation onset matches the potential at which UOR ends on the reverse scan. Furthermore, each urea concentration achieves j_p between 0.65 and 0.9, indicating that at higher potentials other factors, including partial surface coverage by CO_2 and OER onset, contribute to a decrease in coverage.

$$\theta_{Ni^{3+}} = \frac{Q_{blank}}{Q'} \tag{5.2}$$

$$Q_{blank} = \nu \int_{0.25}^{0.60} j dE \tag{5.3}$$

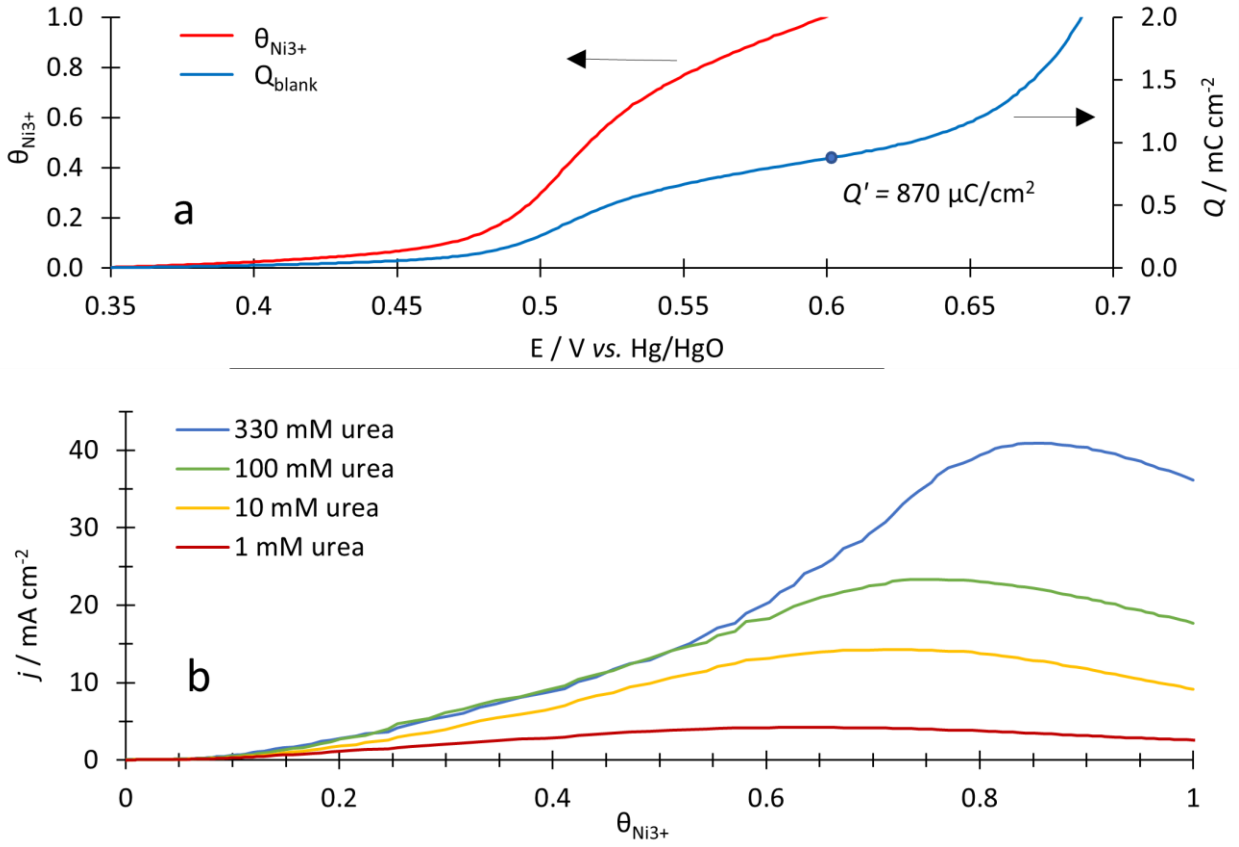

Figure 5.10 a) Q_{blank} and $\theta_{Ni^{3+}}$ plotted against E, with Q' labeled and used to calculate $\theta_{Ni^{3+}}$ (Equation 5.2), and b) current density as a function of $\theta_{Ni^{3+}}$.

To calculate the heterogenous rate constant (k_a) for the electrochemical oxidation rate (r) of urea, Equation 5.4 is used, which describes the reaction rate dependence of a reversible electrochemical reaction based on electrode potential, E [104]. The first term corresponds to the oxidation reaction and the second term corresponds to the reversible reduction reaction. When $E = E^0 + \eta$ and the $E^0 = \frac{RT}{nF} \ln \frac{k_c c_O}{k_a c_R}$, the equation describes reaction rate dependence on η rather than E and is referred to as the Butler-Volmer equation. To simplify Equation 5.4 in its application to UOR, it is assumed that only the oxidation reaction occurs, captured by the first

term. For this assumption to hold at room temperature, an overpotential of at least +0.117 V must be applied, which is confirmed in the following experiments. The rate equation is then simplified to Equation 5.5, where $j_0 = n_e F k_a c_R^{\alpha}$, n_e is the number of electrons transferred in the rate determining step, F=96,485 C/mole e^-, c_R is the concentration of the species becoming oxidized, α is the reaction order with respect to c_R, β is the transfer coefficient, T is absolute temperature, and R is the universal gas constant. Equation 5.5 is equivalent to the Tafel equation as a function of E rather than η. To calculate the UOR reaction rate constant (k_a), exchange current density (j_0), the (1- β)n_e combined term, and the reaction order (α) were experimentally determined below.

$$r = \frac{j}{n_e F} = k_a c_R^{\alpha} \exp\left[\frac{(1-\beta) n_e F E}{RT}\right] - k_c c_O \exp\left[\frac{(-\beta) n_e F E}{RT}\right] \tag{5.4}$$

$$\log(j) = \log(j_0) + \frac{(1-\beta) n_e F E}{RT} \tag{5.5}$$

Figure 5.11 shows a Tafel plot of 0.33 M urea in 1 M KOH, concentrations high enough to avoid mass transport effects. The data were collected at ν = 1 mV/s to approach steady state conditions during a potentiodynamic experiment. Based on Figure 5.11, an equilibrium potential E^0 = 0.292 V vs. Hg/HgO is experimentally determined. Due to the dependence of UOR on Ni^{3+}, it is not possible to calculate E^0 for UOR independent of $Ni(OH)_2$ oxidation, and therefore the measured E^0 represents the equilibrium potential of Ni^{2+} oxidation. Thus, to justify the dominant oxidation reaction assumption for Equation 5.5, kinetic data is analyzed above 0.41 V vs. Hg/HgO.

The Tafel plot shows a slope of 27.7 mV/decade (highlighted by red dashed line), which yields a calculated $(1-\beta)n_e$ = 2.1. Figure 5.11 inset is a linear-scale representation of the same data that highlights the calculated Tafel slope region to confirm it only captures oxidation onset. Additionally, exchange current density is experimentally determined to be $j_0 = 7.76\times10^{-12}\,\mathrm{A/cm^2}$, defined at the intersection of the Tafel slope and E^0 (Figure 5.11).

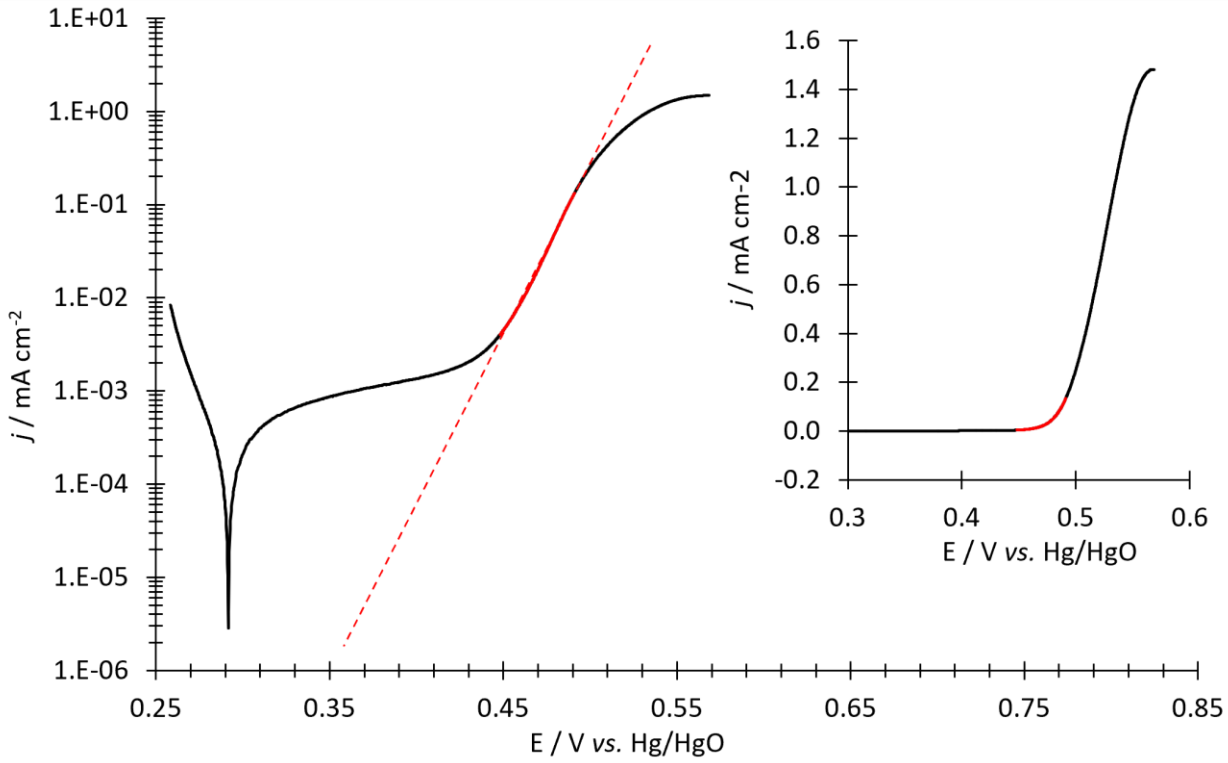

Figure 5.11 Tafel plot for 0.33 M urea in 1 M KOH, performed ν = 1 mV/s. A red dotted line highlights the Tafel slope and was calculated using red current data. The inset shows the same data on a linear current scale. The data demonstrates a Tafel slope of 27.7 mV/decade, E^0 = 0.292 V vs. Hg/HgO, and $j_0 = 7.76\times10^{-12}\,\mathrm{A/cm^2}$.

A double logarithmic plot of current density versus urea concentration (Figure 5.12) was used to determine α, based on slope. The slope of the double log plot increases with applied voltage until a maximum is achieved at potentials above 0.46 V vs. Hg/HgO. This agrees with the

previous discussion regarding a requirement of $\theta_{Ni^{3+}}$ > 0.08 for UOR reaction on a Ni WE, which corresponds to electrode potentials above 0.46 V vs. Hg/HgO. Thus, α = 0.39 is used for the reaction order with respect to urea. Based on the experimental results, a heterogeneous rate constant of $k_a = 3.1\times10^{-16}\,\mathrm{cm/s}$ is calculated for the oxidation of urea on a Ni WE in 1 M KOH.

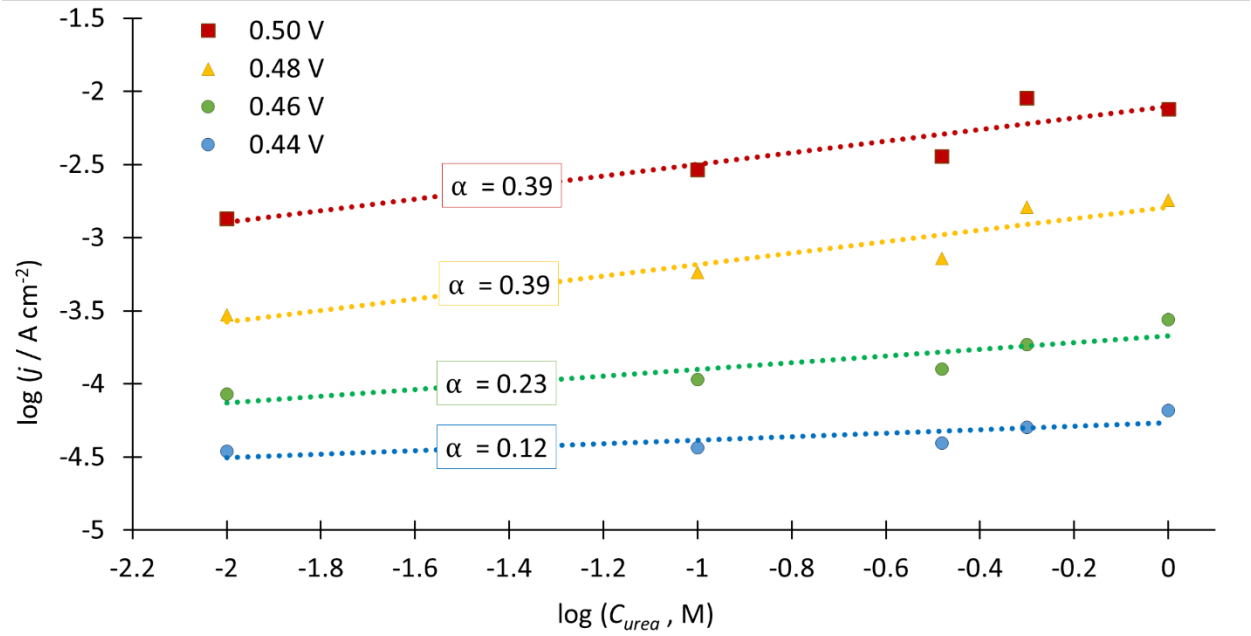

Figure 5.12 Double logarithmic plot of current density as a function of urea concentration in 1 M KOH to calculate α, reaction order with respect to urea (Equation 5.4). Reaction order increases with voltage until 0.48 V vs. Hg/HgO is met, which corresponds with favorable $\theta_{Ni^{3+}}$ for UOR on Ni.

To conclude the kinetic studies for UOR on a Ni disk WE, turn over frequency (TOF) is calculated according to Equation 5.6, where n_u is the number of urea molecules reacted, n_{Ni} is number of Ni surface sites reacted upon, and t is time. When n_u and n_{Ni} are defined by Equation 5.7 and Equation 5.8, respectively, N_{av} and F cancel accordingly. The number of urea molecules reacted was calculated based on mathematical difference of current with urea (j_u) above that of

the blank (j_b), assuming 100% Faradic efficiency (Equation 5.7). The number of Ni surface sites was calculated to be 5.43×10^{15} sites/cm^2 based on Q' (Equation 5.8) which corresponds to a roughness factor of about 3. A series of CAs were collected to calculate TOF at various urea concentrations, shown in Figure 5.13. Because j_p occurs at potentials that are anodically shifted with higher concentrations (Figure 5.9b) the E_{hold} potential used increases with concentration and is listed in Table 5.3 for each urea concentration. The calculated TOFs increase with urea concentration, C_u, to reach a maximum of 0.66 s^{-1} (Table 5.3).

$$\mathrm{TOF} = \frac{n_u}{n_{Ni}t} = \frac{\int_0^{60}(j_u - j_b)dt}{6Q't} \tag{5.6}$$

$$n_u = \frac{N_{av}}{6F}\int_0^{60}(j_u - j_b)dt \tag{5.7}$$

$$n_{Ni} = \frac{N_{av}}{F}Q' \tag{5.8}$$

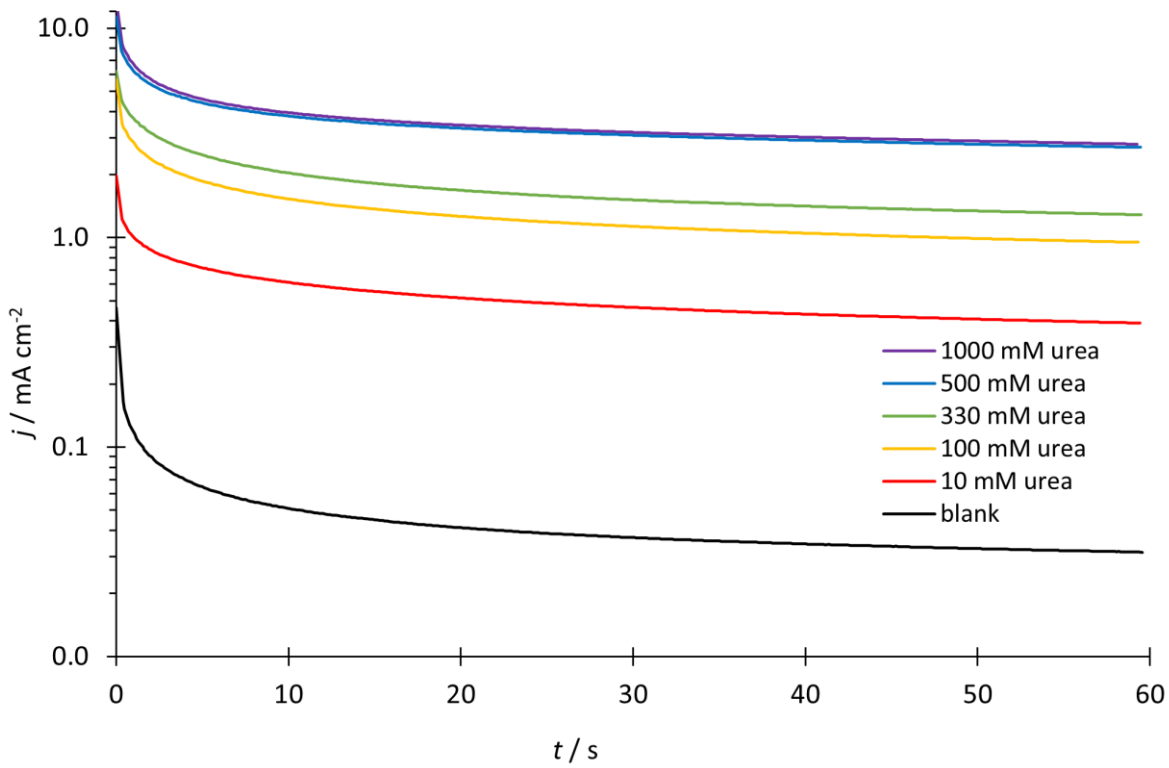

Figure 5.13 Potentiostatic CAs performed in 1 M KOH for 0–1M urea at various E_{hold} potentials, listed in Table 5.3.

C_u (mM)	E_{hold} (V vs. Hg/HgO)	TOF s^{-1}
10	0.55	0.09
100	0.57	0.24
330	0.57	0.32
500	0.58	0.64
1000	0.58	0.66

Table 5.3 Calculated TOF based on CAs in Figure 5.13 and Equation 5.6. TOF increases with urea concentration, C_u, and potentiostatic hold potential, E_{hold}

Chapter 6. OXIDATION OF UREA AND CREATININE ON NI FOAM-BASED ELECTROCATALYSTS

Reproduced with permission from Springer Nature.

Carpenter, K., Stuve, E.M. Electrooxidation of urea and creatinine on nickel foam-based electrocatalysts. J Appl Electrochem (2021). https://doi.org/10.1007/s10800-021-01545-1

Electrochemical degradation of urea from aqueous waste streams is an attractive technology, mainly due to scalability [11]. Wastewater contains large quantities of urine, of which the two most abundant organic compounds are urea and creatinine. An effective method for removal of organic compounds, including both urea and creatinine, is crucial for the technologies of wastewater denitrification [14, 15], portable dialysis [10, 12], and potable water recovery from urine [20]. A recent electrochemical study of urine compounds [105] showed that creatinine is a significant inhibitor of the urea oxidation reaction in alkaline conditions on a $NiCo_2O_4$ catalyst. Apart from this 2018 study, creatinine has not been studied electrochemically, leaving it ripe for electrocatalytic research. Development of catalysts that can simultaneously oxidize urea and creatinine will be valuable to multiple industries. Furthermore, because urine and dialysate concentrations differ substantially in both scale and solute ratios, investigating each concentration regime independently is required. This study seeks to address both topics to further inform technological development in wastewater treatment.

The electrochemical oxidation of urea is well-studied due to its technological relevance [26, 65, 75, 106]. To date, one of the best performing electrocatalysts is nickel hydroxide, $Ni(OH)_2$ [62, 86, 89]. At potentials above 0.45 V vs. Hg/HgO and pH 14, $Ni(OH)_2$ becomes electrochemically transformed into the catalytically active nickel oxyhydroxide (NiOOH), upon which urea oxidizes to form CO_2, N_2, and H_2O, regenerating the $Ni(OH)_2$ surface site in the process [61]. This complete urea electrooxidation is a 6-electron process. The analogous complete alkaline electrooxidation of creatinine is a 21-electron process, as indicated in Reaction 6.1. Due to the high kinetic barrier for multi-electron processes, it is unlikely that creatinine completely oxidizes, though no electrochemical mechanisms have been proposed.

$$C_4H_7N_3O_{(aq)} + 21OH^-_{(aq)} \rightarrow 4CO_{2(g)} + \frac{3}{2}N_{2(g)} + 14H_2O_{(l)} + 21e^- \qquad (6.1)$$

6.1 EXPERIMENTAL

6.1.1 *Materials*

All chemicals were purchased from Sigma-Aldrich. The Ni and Fe salts used were ultra-high purity (99.999% trace metal basis) while urea, creatinine, and potassium hydroxide, were ACS reagent grade. The hydrothermal growth and doping of nickel $Ni(OH)_2$ and 1% Fe-doped $Ni(OH)_2$, herein referred to as nickel hydroxy foam (NHF) and Fe-NHF, respectively is detailed in 3.3.1.

6.1.2 *Electrochemical Cell and Experimental Parameters*

All experiments reported in this chapter were performed in a 3-electrode cell utilizing a Ni foam, NHF, or Fe-NHF working electrode (WE), all with geometric areas of 1.0 cm^2. All electrochemical data reported in a figure were obtained from the same WE, so real electrode surface area remains consistent between scans. The active electrochemical surface area (ECSA) was estimated using the blank anodic scan charge [86]. ECSA calculations for each electrode prior to each experiment on all catalysts and dates are shown in Appendix D. The counter electrode (CE) was a homemade, high surface area Pt coil electrode. The reference electrode (RE) was a single junction Hg/HgO electrode (Pine research) with 4.24 M KOH filling solution, designed for stability in alkaline conditions; all voltages reported in text and figures are in reference to Hg/HgO (98 mV vs. NHE). The background electrolyte was 1 M KOH solution with 2–330 mM urea and/or 0.06–18 mM creatinine added. Urea and creatinine concentrations were chosen to mimic dilute dialysate and more concentrated urine.

All cyclic voltammograms (CVs) were performed at room temperature and ν= 10 mV/s within a potential window that minimized oxygen evolution. Each CV reported is the result of the third potential cycle; the current density did not depend on cycle number after the first cycle. CV experiments were repeated for dialysate concentrations on all catalysts over multiple electrodes and dates. Replicate experimental data are reported in the SI. The chronoamperometry (CA) voltage was chosen based on the current density maximum in the CVs. The cell was sparged with N_2 during both the potentiodynamic and potentiostatic experiments a) to prohibit CO_2 absorption in the alkaline electrolytes and b) to dislodge gas bubbles formed during reaction on the Ni foam-

based electrodes. Legends on electrochemical data figures denote concentrations for urea and creatinine using a format of Urea:Creatinine (mM:mM).

The oxygen evolution reaction (OER) competes with the urea oxidation reaction (UOR), especially at higher potentials. Nickel hydroxides, particularly iron-doped nickel hydroxides, are well-known OER catalysts in alkaline solutions with the ability to reduce OER overpotentials even when ECSA is accounted for [107, 108]. To interpret urea and creatinine oxidation independent of changes in OER overpotential, it is necessary to characterize the OER current of each experiment and subtract it from total oxidation charge to obtain an OER-corrected oxidation charge (Q_{ox}), graphically depicted in Figure . The linear OER region in each CV provides an internal reference to characterize OER based on calculated slope (m) and voltage intercept (E_1) as shown in Figure 6.1. Total oxidation charge is measured on the forward scan and the OER current (Figure 6.1, red shaded) is subtracted to obtain the OER-corrected charge density (Figure 6.1, hashed). Oxidation onset (E_0) is the voltage where current reaches 0.1 mA/cm^2. In dialysate concentration experiments, the upper potential limit (E_2) is defined as the local current density minimum prior to onset of linear OER. In urine-relevant concentration experiments on NHF and Fe-NHF, a local current density minimum does not exist and therefore E_2 is the highest potential scanned. Reduction charge density is measured on the return scan between the potential at which the current becomes reducing and the lowest potential.

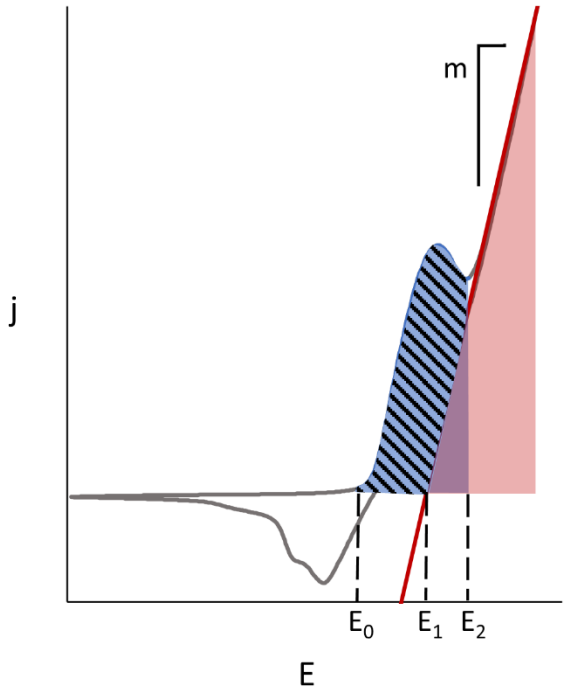

Figure 6.1 Graphical depiction of OER current density defined by slope (m) and voltage intercept (E_1) of linear OER region. The OER-corrected oxidation charge (Q_{ox}) is represented by the hashed region.

6.2 RESULTS

6.2.1 *Electrode Characterization*

Figure 6.2 shows the SEM images of clean Ni foam, NHF, and Fe-NHF, respectively. Hydrothermal growth of $Ni(OH)_2$ and $Fe(OH)_3$ appear in two varieties: microparticles (Figure 6.2b) and nanowalls [90] (Figure 6.2b, c). The hydroxy nanowalls are apparent at magnifications above ~2000x and coat all surfaces exposed to the hydrothermal bath. When nanowalls grow on hydroxy microparticles, the structures are referred to as "flowerlike" (Figure 6.2b) [83, 105, 109]. Morphologies for NHF and Fe-NHF are similar, though SEM comparison reveals fewer flowerlike structures on Fe-NHF (Figure 6.2b, c). The increased surface roughness of the NHF and Fe-NHF

compared to Ni foam are in good agreement with ECSA calculations reported in Table 6.1 and calculated in Appendix D. For this reason, current densities based on geometric area are not comparable between electrodes without normalizing by ECSA. Energy-dispersive spectroscopy element maps and spectra (Figure 6.3) of Fe-NHF reveal uniform distribution of Ni, Fe, and O throughout the sample. The EDS results indicate that Fe doping on the surface was 0.8%, in reasonable agreement with the intended level of 1%.

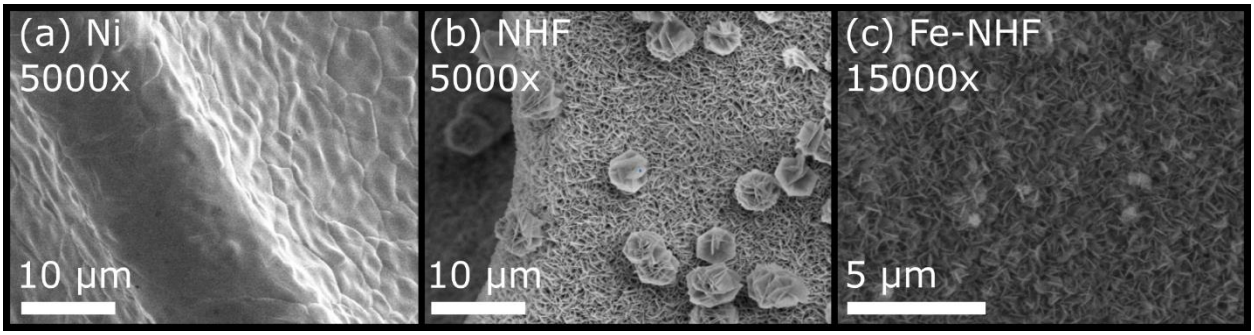

Figure 6.2 SEM images of a) Ni foam, b) NHF, and c) Fe-NHF with magnifications noted.

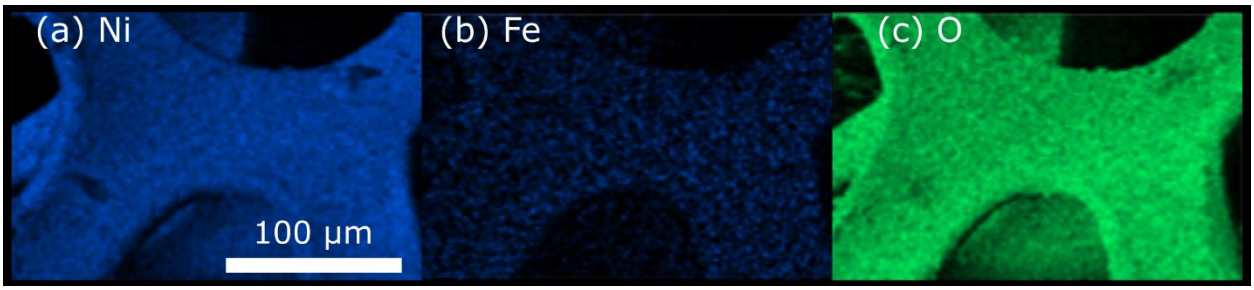

Figure 6.3 Fe-NHF electrode EDS elemental maps for surface species of a) Ni (L series), b) Fe (L series), and c) O (K series).

Electrode	ECSA (cm^2)
Ni Foam	58.0
NHF	894
Fe-NHF	502

Table 6.1 Electrochemical surface area (ECSA) for electrodes reported in all figures. The calculations for these electrodes and others used in repeated experiments are found in Table A.4.

6.2.2 *Ni Foam Electrodes*

The cyclic voltammograms in Figure 6.4 and Figure 6.5 were obtained on a Ni foam electrode in 1 M KOH. Figure 6.4 is the blank CV without urea and shows the redox conversion of $Ni(OH)_2$ to NiOOH, occurring between potentials of 0.43 V and 0.55 V. The oxidation peak shoulder is due to oxidation of α-$Ni(OH)_2$, while the main peak is a result of the oxidation of β-$Ni(OH)_2$. On the return scan, a double reduction peak is observed due to the reduction of β-NiOOH and γ-NiOOH [25]. Oxygen evolution begins at 0.62 V on the positive scan. The reverse scan of Figure 6.4 reveals the transition of NiOOH back into $Ni(OH)_2$, referred to as the Ni^{3+} reduction peak. The data from Figure 6.4 are also included in Figure 6.5 for reference against urea containing solutions. Urea concentrations in the range of healthy (2 mM) to uremic (10 mM) human serum and a typical urine concentration of 330 mM produce oxidation peaks that follow the leading edge of the Ni^{2+} oxidation peak. The maximum urea oxidation current density j_p increases with urea concentration and shifts to more positive potentials, as listed in Table 6.2. For the 330 mM urea concentration, urea oxidation current continues into the OER region. The return scans for the urea-containing solutions remain above the blank CV, although without the presence of peaks.

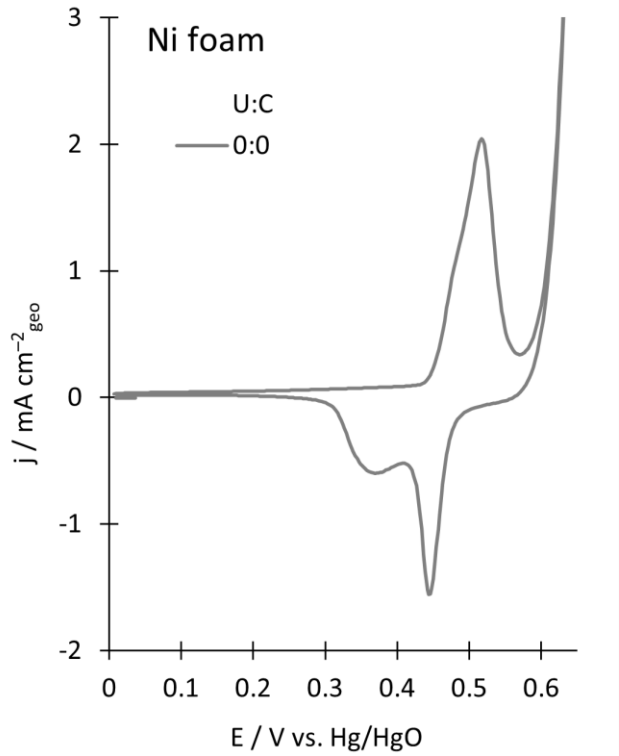

Figure 6.4 Cyclic voltammogram (CV) of 0 mM urea on Ni foam in 1 M KOH.

Two notable differences seen in the 330 mM urea data, with respect to the lower concentration curves, are that the return scan crosses over the forward scan at about 0.54 V, and the Ni^{3+} reduction peak is reduced in intensity by 63%, in line with results by other researchers [18, 62, 83, 86, 106]. These two features are not observed with dialysate-relevant solution due to the much lower urea concentration.

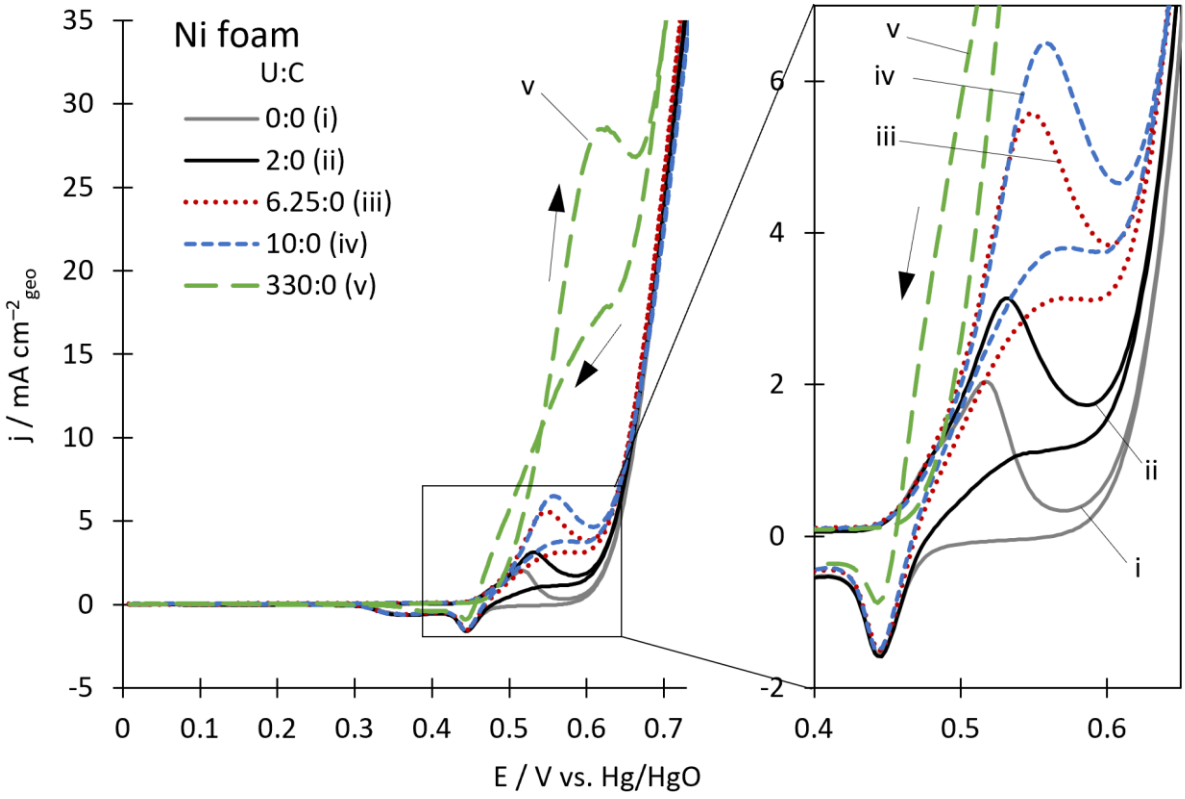

Figure 6.5 CVs of 0 (i), 2 (ii), 6.25 (iii), 10 (iv), and 330 (v) mM urea on Ni foam in 1 M KOH.

[Urea] (mM)	j_p (mA/cm$^2_{geo}$)	E_p (V vs. Hg/HgO)
0	2	0.52
2	3	0.53
6.25	6	0.55
10	7	0.56
330	28	0.62

Table 6.2 Peak current densities (j_p) and associated potentials (E_p) for each CV in Figure 6.5.

Figure 6.6 shows CVs of creatinine-only solutions with concentrations of 0.18 and 18 mM to capture the dialysate and urine-relevant concentration regimes, respectively. The potential of

the Ni^{2+} oxidation peak did not change with 0.18 mM creatinine concentration, but is anodically shifted by 10 mV for 18 mM creatinine. The 18 mM creatinine solution lacks the subtle oxidation shoulder at 0.48 V that occurs in the other two scans. The onset of OER is unchanged by creatinine. The shape of each oxidation curve resembles the blank CV, though with slightly increased current density throughout the entire positive and negative scans above 0.5 V. Comparison of 18 mM creatinine to the blank shows a 34% increase in oxidation charge and a 27% decrease in reduction charge, which may indicate that creatine oxidizes on Ni, though with severe kinetic limitations compared to urea (compare with Figure 6.5).

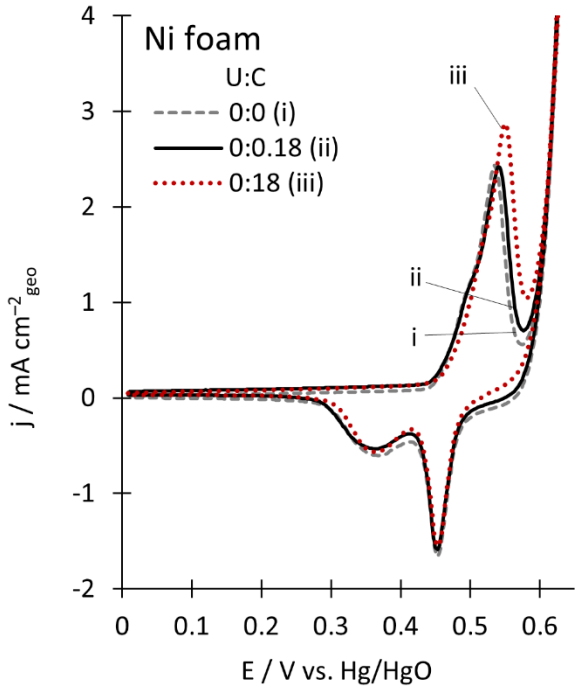

Figure 6.6 CVs of creatinine on Ni foam in 1 M KOH at dialysate- (0.18 mM) and urine-relevant (18 mM) concentrations.

Figure 6.7 shows that creatinine added to urea solution decreases the oxidation current on Ni foam in the urea oxidation region as compared to that for urea alone. Figure 6.7a

demonstrates a 7% decrease, and Figure 6.7b a 50% decrease, in oxidation charge when creatinine is present (Table 6.3). The presence of creatinine increases E_0 by 6 mV in Figure 6.7a, yet decreases E_0 by 24 mV in Figure 6.7b (Table 6.3). The oxidation kinetics of urea are more severely limited at higher concentrations (Figure 6.7b), implying that the oxidation rate of urea decreases with increasing creatinine concentration on Ni foam. At high concentrations, urea oxidation continues along with OER (Figure 6.7b) contributing to sustained increased current above the blank OER. In Figure 6.7b, the reduction peak for urea with creatinine is enhanced with respect to that for the urea-only CV, in agreement with lower overall urea oxidation (Table 6.3) [61].

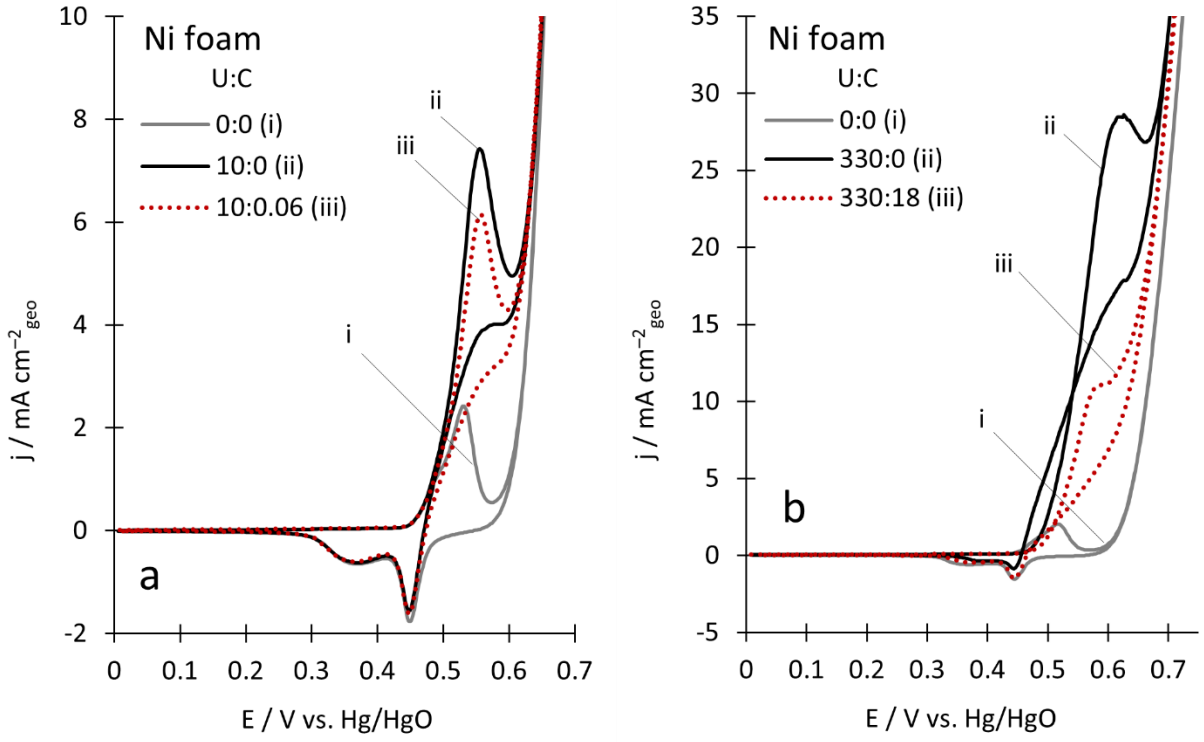

Figure 6.7 CVs of urea alone and with creatinine in 1 M KOH for a) dialysate-relevant concentrations and b) urine-relevant concentrations of each solute.

Urea:Creatinine (mM:mM)	Q_{ox} (mC/cm$^2_{geo}$)	Q_{red} (mC/cm$^2_{geo}$)	E_0 (mV)	Reference
10:0	59.8	–11.3	440	Figure 6.7a
10:0.06	55.6	–11.2	446	Figure 6.7a
330:0	302	–3.8	429	Figure 6.7b
330:18	150	–7.4	405	Figure 6.7b

Table 6.3 Oxidation charge density, (Q_{ox}), reduction charge density (Q_{red}), and oxidation onset (E_0) extracted from the CVs in Figure 6.7. Oxidation onset values are defined as the voltage where current density reached 0.1 mA/cm^2, in mV vs. Hg/HgO.

In Figure 6.8a, creatinine was added prior to urea rather than *vice versa* as in the experiments for Figure 6.7b. Figure 6.8b demonstrates that the order of solute introduction into the cell plays a role in oxidation potential on Ni. Addition of 330 mM urea to 18 mM creatinine (Figure 6.8a) did not match the data in Figure 6.8b with the same concentrations. A 30 mV increase in peak potential was observed when creatinine interacts with the Ni surface prior to urea, which contributes to lower overall charge passed in the urea oxidation region. It is unclear whether the difference in peak current densities of Figure 6.8b is attributed to minor concentration differences between the two different solutions or differences in electrode surface between the experiments.

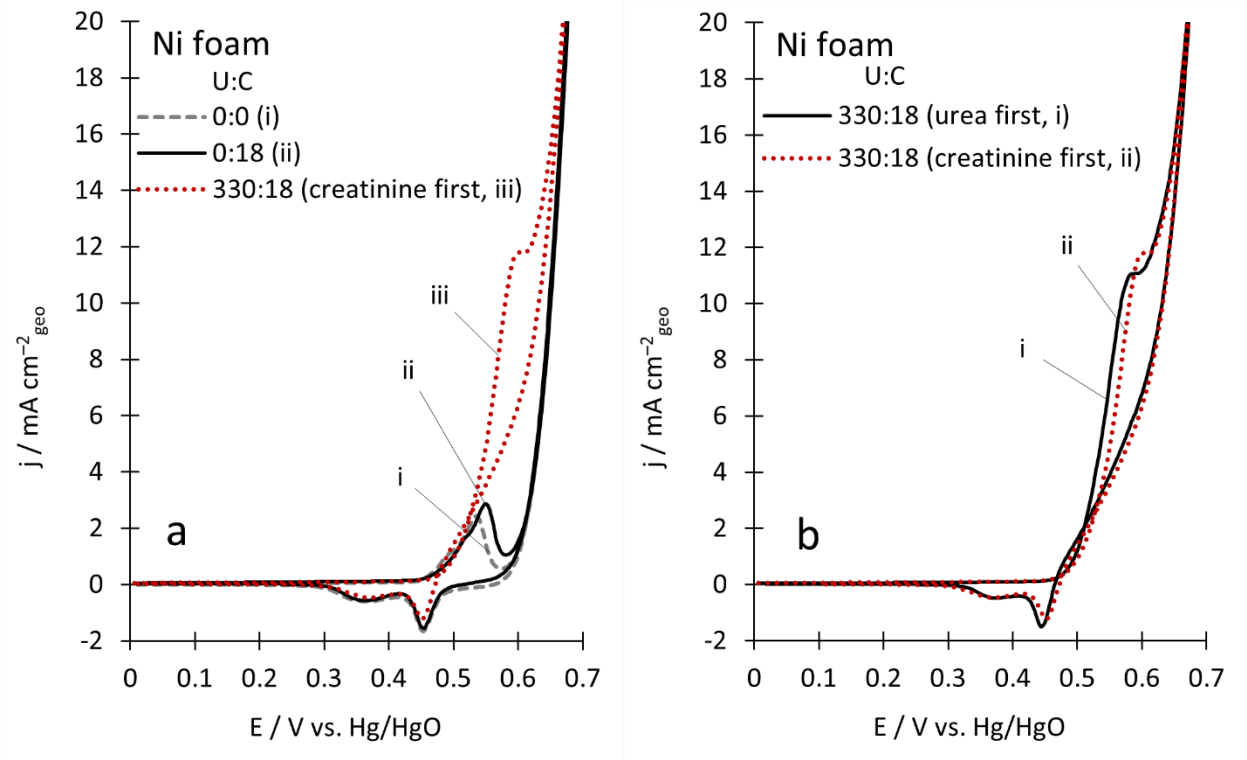

Figure 6.8 CVs of urine-relevant concentrations of creatinine and urea in 1 M KOH on Ni foam. a) 18 mM creatinine added before 0.33 M urea; b) comparison of urea and creatinine CVs from Figure 6.7b and Figure 6.8a

6.2.3 *NHF Electrodes*

On a NHF electrode, the presence of 0.18 mM creatinine had little effect on the Ni^{2+}/Ni^{3+} transition, as shown in Figure 6.9. A creatinine concentration of 18 mM increased the peak potential by 16 mV and contributed to a 14% oxidation charge increase with a 26% reduction charge decrease, similar to that observed on Ni foam (Figure 6.4). Comparison of urea-only (ii, Figure 6.10) and urea/creatinine solutions on NHF (iii and iv, Figure 6.10) shows that urea oxidation charge is suppressed by 2–13% in the presence of 0.06–0.18 mM creatinine. Creatinine-induced oxidation suppression on Ni foam (Figure 6.7a) was more evident: a 7% decrease with addition of 0.060 mM creatinine, as opposed to 2% on NHF (Figure 6.10). Although peak current

density differences are small in Figure 6.10, a trend emerges revealing that peak current density decreases with increasing creatinine concentration. This trend continues with the urine-relevant concentrations in Figure 6.11, showing a 36% charge decrease when 18 mM creatinine was added to 330 mM urea. The urine-relevant concentration experiments on NHF (Figure 6.11) demonstrate monotonically increasing behavior towards UOR without the oxidation peak seen on Ni foam (Figure 6.5, long dashed line). This associated higher reaction rate on NHF is due to the well-reported increased UOR activity of NHF compared to Ni catalyst [86], in addition to higher ECSA (Table 6.1). Figure 6.7 and Figure 6.10–Figure 6.11 demonstrate the existence of creatinine concentration-dependent UOR suppression on Ni foam and NHF, respectively.

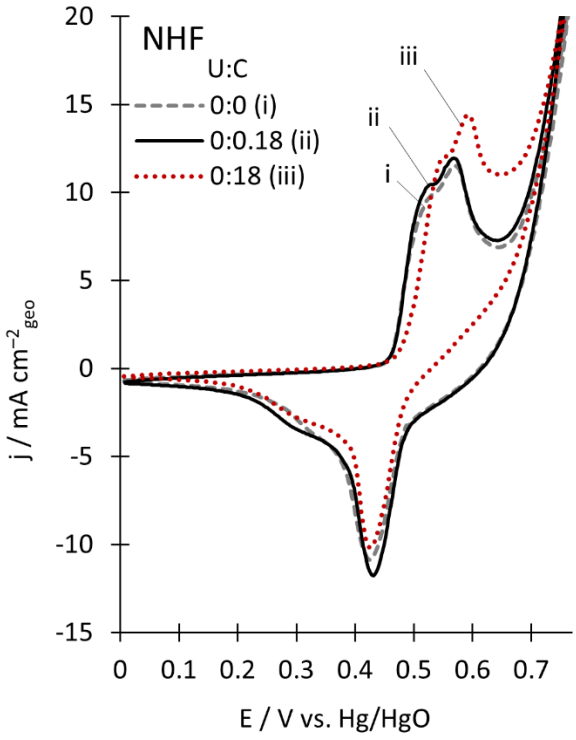

Figure 6.9 CVs of creatinine on NHF in 1 M KOH at dialysate- (0.18mM, ii) and urine-relevant (18 mM, iii) concentrations

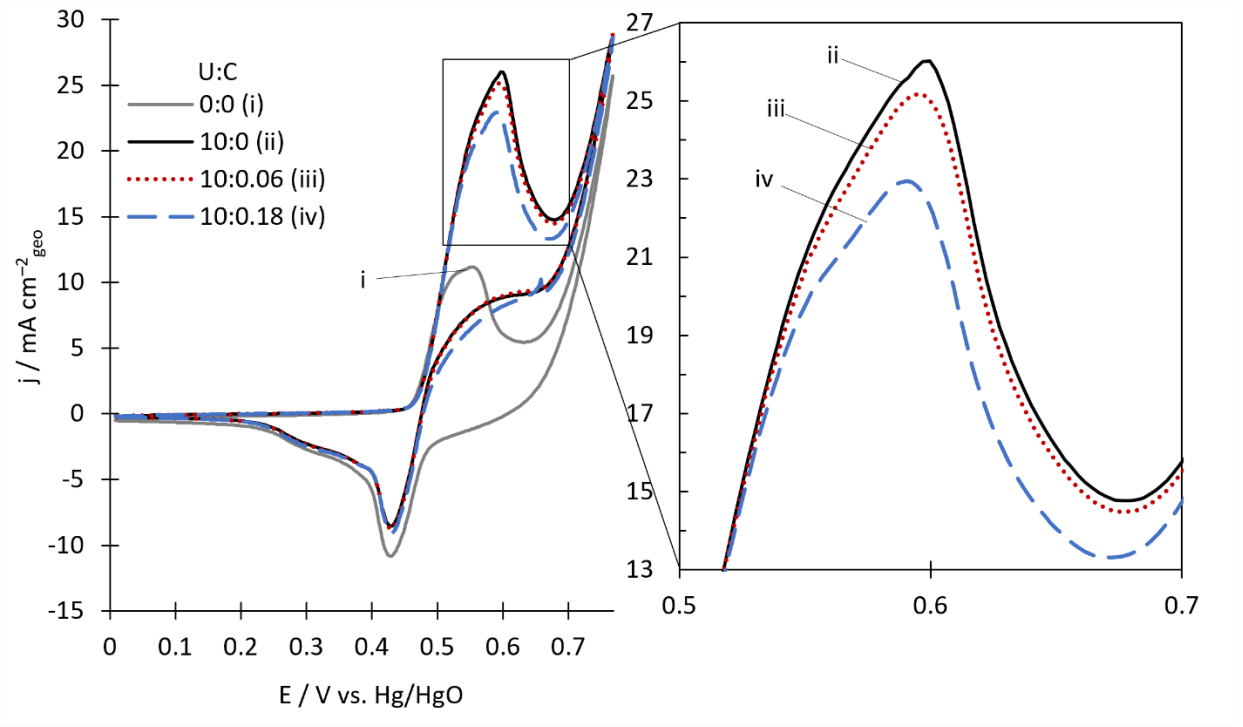

Figure 6.10 CVs of urea alone (ii) and urea with creatinine (iii, iv) in 1 M KOH on NHF for dialysate-relevant concentrations

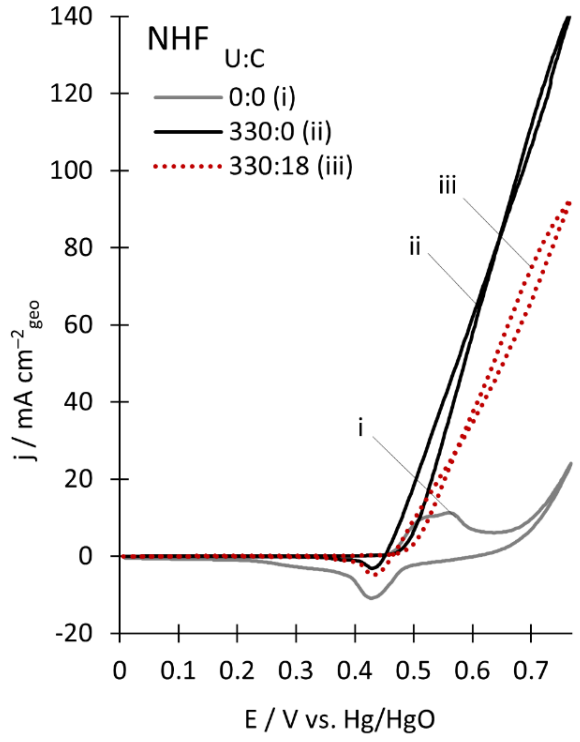

Figure 6.11 CVs of urea alone (ii) and urea with creatinine (iii) in 1 M KOH on NHF for urine-relevant concentrations

6.2.4 *Fe-NHF Electrodes*

Figure 6.12 and Figure 6.13–Figure 6.14 show CVs of creatinine-only and urea/creatinine, respectively, on a Fe-NHF electrode. Like the other Ni-based electrodes, the presence of 0.18 mM creatinine does not change the Ni^{2+}/Ni^{3+} couple on the Fe-NHF electrode significantly. A creatinine concentration of 18 mM increases the oxidation peak potential by 17 mV and peak current density by 4 mA/cm^2, yielding a 21% increase in oxidation charge and 16% decrease in reduction charge compared to the blank scan. In contrast to Figure 6.7 and Figure 6.10–Figure 6.11, Figure 6.13–Figure 6.14 reveal *enhanced* oxidation current between 0.55 and 0.70 V on the positive scan when creatinine is added to urea on the Fe-NHF electrode. A 18–29% charge increase is seen for the dialysate-relevant addition of 0.06–0.18 mM creatinine compared to 10 mM urea alone on a Fe-NHF electrode (Figure 6.13, Table A.6). The associated OER region remains unaffected and the presence of creatinine, independent of concentration, does not reduce oxidation on the return scan compared to the urea-only curve (Figure 6.13). Similarly, the high concentration experiment (Figure 6.14) exhibits an 8% increased oxidation charge when creatinine is added and indicates the possibility of co-oxidation of urea and creatinine, even in the OER region. The return scan for the creatinine-containing high concentration experiments (iii, Figure 6.14) crosses over itself, and the hysteresis causes it to fall below the return scan of the urea-only solution at voltages lower than 0.61 V. Additionally, the Ni^{3+} reduction peak below 0.45 V for the dual solute scans (iii, iv Figure 6.13 and iii Figure 6.14) have more negative reduction

current densities, which may indicate that fewer Ni^{2+} surface sites took place in the oxidation reactions of urea and creatinine [61], as discussed in 6.3.

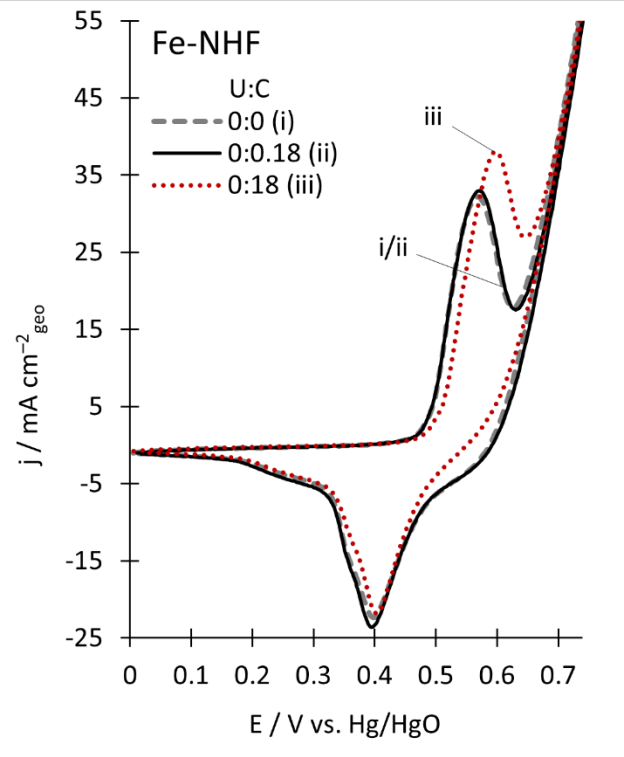

Figure 6.12 CVs of creatinine on a Fe-NHF electrode in 1 M KOH.

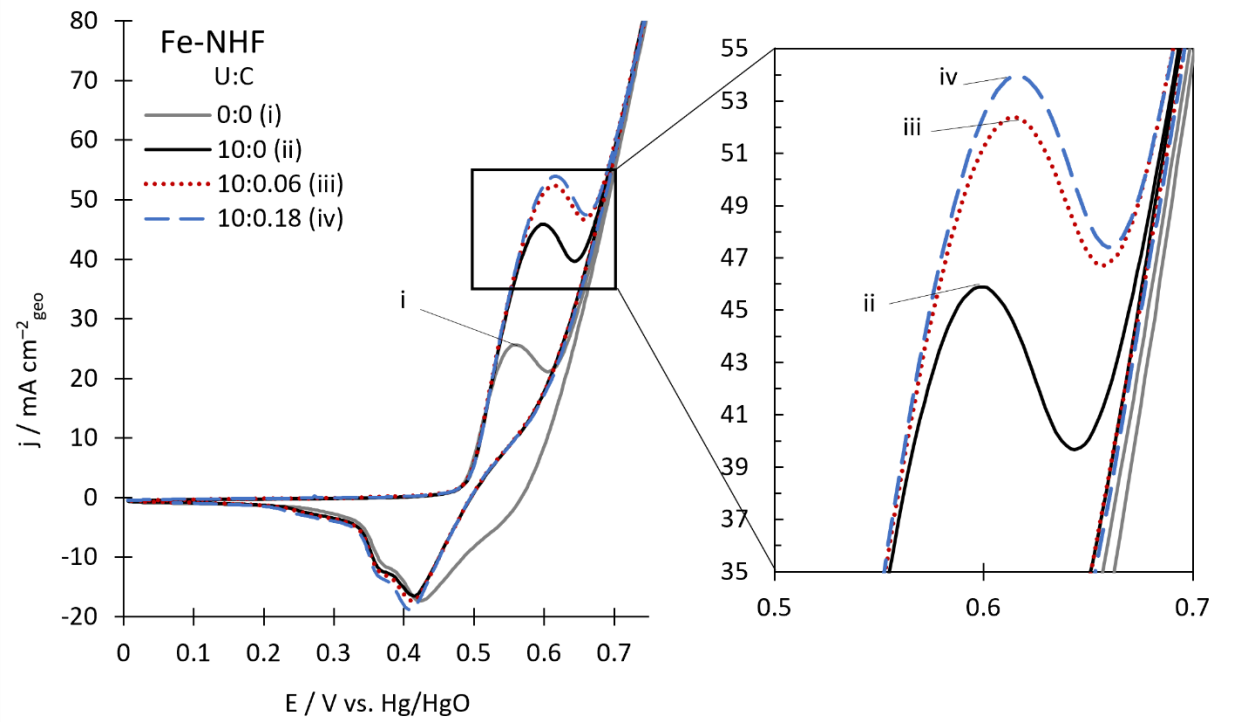

Figure 6.13 CVs of urea and creatinine in dialysate-relevant concentrations on a Fe-NHF electrode in 1 M KOH.

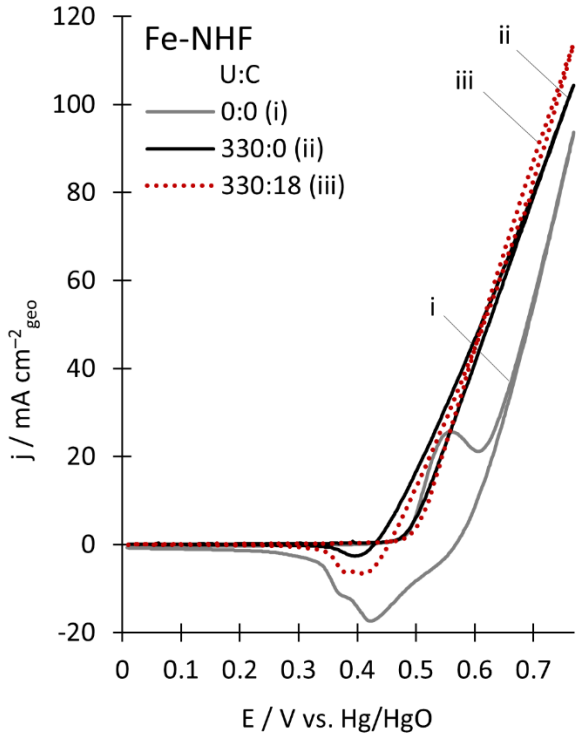

Figure 6.14 CVs of urea and creatinine in urine-relevant concentrations on a Fe-NHF electrode in 1 M KOH.

Experiments for dialysate concentrations on Ni foam, NHF, and Fe-NHF were repeated on multiple dates and electrodes. The full analysis for each experiment is documented in Appendix D (Tables A.5, Table A.6), and the results are summarized in Table 6.4. The average percent change in Q_{ox} is reported, based on catalyst type, for the creatinine containing experiments relative to the urea-only experiments performed on the same electrode and date. Additionally, Table 6.4 reports the spread in average change values and how many experiments were performed on each electrode (n). Electrochemical data varied with electrode and date; however, the creatinine-induced trends remain consistent and show increased Q_{ox} on Fe-NHF, minimal change in Q_{ox} on NHF, and reduced Q_{ox} on Ni foam.

Catalyst	Average Change Q_{ox}	Spread	n
Ni Foam	–14%	15%	3
NHF	–3%	2%	2
Fe-NHF	+14%	8%	3

Table 6.4 Combined results from multiple electrodes and dates summarizing how the presence of creatinine changes Q_{ox} in dialysate-relevant concentrations on each catalyst. "Spread" refers to the variation of measured average change percentages. Full analysis for individual experiments can be found in the SI.

During a constant potential hold at 0.6 V vs. Hg/HgO for 15 minutes, the NHF electrode exhibits continuous urea oxidation, as shown in Figure 6.15a. The presence of 0.18 mM creatinine reduces the current density for the duration of the experiment resulting in a 19% decrease in oxidation charge over the 15 minutes, in agreement with the potentiodynamic results in Figure 6.10. The Fe-NHF electrode (Figure 6.15b) shows increased OER (i) and UOR (ii) current density

at 0.6 V compared to the associated NHF current (Figure 6.15a), which can be attributed to 1.8x ECSA (Table 6.1) and better OER kinetics [107]. On Fe-NHF, the presence of 0.06 and 0.18 mM creatinine suppressed oxidation charge by 15% and 8%, in disagreement with the potentiodynamic charge enhancement seen in Figure 6.13 and reported in Table 6.4. The first 60 s of each CA is nearly indistinguishable from each other—aside from current noise, which is lower at higher creatinine concentrations. Longer timescales differentiate the curves. Creatinine maximally suppresses the reaction at 0.06 mM creatinine (Figure 6.15b, iii) with 0.18 mM creatinine (Figure 6.15, iv) showing an overall charge enhancement compared to 0.06 mM. Figure 6.15 confirms that a) creatinine does not limit overall oxidation as drastically on Fe-NHF as it does on NHF and that b) creatinine suppresses charge below that of UOR during a prolonged voltage hold on Fe-NHF, though evidence for co-electrooxidation is discussed in the next section.

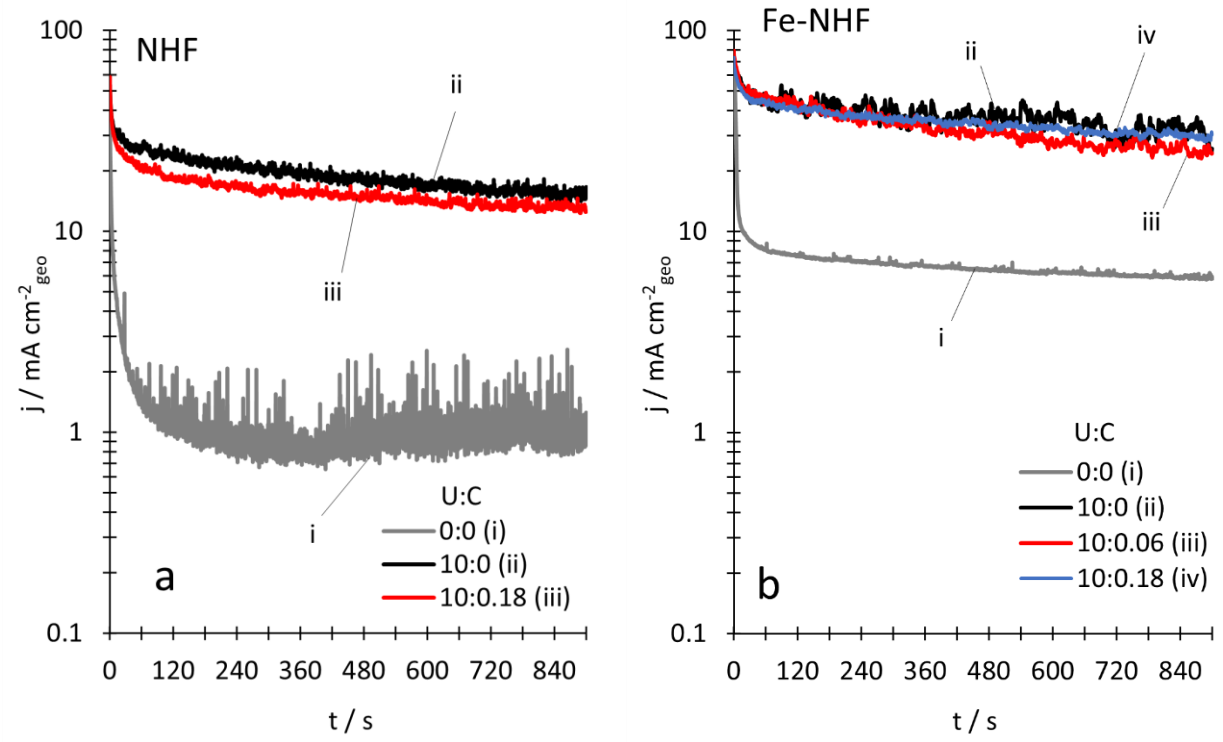

Figure 6.15 Chronoamperometry of urea on a) NHF and b) Fe-NHF electrodes at 0.6 V with and without dialysate-relevant creatinine concentrations in 1 M KOH.

6.3 DISCUSSION

Typical concentrations of urea and creatinine in human urine are 220 mM and 13 mM, respectively [20]; this study used 330 mM urea and 18 mM creatinine to better align with a 2018 study [105]. In dialysate, urea and creatinine exist in lower concentrations, about 10 mM and 0.06 mM, respectively, as used in this study. Additionally, 0.12 and 0.18 mM creatinine were used in this study to understand concentration-dependent trends; however, to improve clarity of Figure 6.10 and Figure 6.13, the 0.12 mM creatinine data are only listed in Tables A.5 and A.6. Thus, the dialysate concentration regime in this study defines a *solute ratio* (urea:creatinine) 3–9 times higher than that of urine. The dialysate concentrations are a) more dilute, leading to lower oxidation currents, and b) have a lower proportion of creatinine molecules leading to less creatinine-induced oxidation effects. Table 6.5 summarizes the electrochemical results reported in 6.2. Overall, the urine-relevant concentrations are more negatively (on Ni foam and NHF), and less positively (on Fe-NHF) affected by the addition of creatinine.

Electrode	**Experiment type**		**Creatinine effect on Q_{ox}**	
	potentiodynamic	potentiostatic	Dialysate-relevant	Urine-relevant
Ni Foam	x		–7%	–50%
NHF	x		–2%	–36%
		x	–19%	-
Fe-NHF	x		+18%	+8%
		x	–15%	-

Table 6.5 Summary of changes in electrochemical oxidation charge (Q_{ox}) with addition of creatinine on each electrode, within each concentration regime, and under different polarization conditions. “Dialysate-relevant” refers to 10 mM urea, 0.06 mM creatinine; “Urine-relevant” refers to 330 mM urea, 18 mM creatinine.

Spectroscopic investigation of creatinine and urea binding on $NiCo_2O_4$ in pH 14 [105] indicates that creatinine forms a strong inner-sphere complex, while urea interacts weakly with the surface through hydrogen bonds. As a result, when both solutes are present, the creatinine preferentially binds, limits urea access to the catalyst, and decreases overall current density. These results are in good agreement with our electrochemical results on Ni foam, and to a lesser extent on NHF, indicating that similar surface-specific molecular binding of creatinine may be limiting oxidation current. However, the introduction of 1 mol% Fe to the NHF catalyst appears to have lessened the creatinine/surface interactions, which allows the co-oxidation of urea and creatinine.

The urease enzyme contains two Ni^{2+} atoms at the active site [110], which are required for the enzymatic degradation of urea via hydrolysis. Although it has been understood for decades that Ni^{2+} is essential to the activity of urease, its role in selectivity has yet to be fully realized [52]. It bears significance that nickel and Ni-containing electrodes often outperform noble metals and nanostructures materials [11, 30, 32, 111] as electrocatalysts for urea. Similarly, creatininase natively has two Zn^{2+} atoms in the active site, yet it has been found that enzyme activity increases when the metal centers are replaced by $Mn^{2+} > Co^{2+} > Mg^{2+} > Fe^{2+} > Ni^{2+} = Zn^{2+}$ [112]. Like with urease, the metal cofactors in creatininase are known to be essential, but their role in catalyst selectivity is uncertain. Thus, it is hypothesized that surface interactions with the listed metal ions could improve binding of creatinine, even on electrocatalytic surfaces. The $NiCo_2O_4$ catalyst exhibited strong interactions with creatinine, which supports this hypothesis, and reaction rate increased at voltages above 0.65 V vs. Hg/HgO in pH 14 [105]. The Fe-NHF

electrode in this study behaved similarly at the same conditions (iii, Figure 6.13). At lower potentials, the adsorbed creatinine molecules compete with urea molecules to cause significant current suppression on $NiCo_2O_4$ and minor suppression on Fe-NHF at urine-relevant concentrations.

The increased current density during a potential sweep on Fe-NHF for creatinine-containing solutions (Figure 6.13–Figure 6.14, Table 6.4) can be attributed to concurrent reactions of creatinine and urea. The 0.06 mM creatinine (iii, Figure 6.13) shows a significant increase in current density with respect to the urea-only CV. The higher concentration of 0.18 mM creatinine (iv, Figure 6.13) yields an even higher current density, as expected.

In comparison with the chronoamperometry results of Figure 6.15b, added creatinine results in a slightly lower current density at times beyond approximately 120 s relative to that of the urea-only case. This indicates the possibility of site blocking caused by stronger adsorption of creatinine, in line with the study by Schranck et al. [105] that reported strong creatinine blocking at urine-relevant concentrations. The site blocking indicated here is not complete, however, as continued reaction of creatinine is evident by virtue of the increased current density for the 10:0.18 solution (iv, Figure 6.15b) relative to that of the 10:06 solution (iii, Figure 6.15b) at times beyond approximately 300 s. Further evidence of incomplete site blocking is seen in current densities of urea/creatinine solutions more than four times that of the blank solution (i, Figure 6.15b) at all times measured.

The differing time scales of measurement for the CV (Figure 6.13) and CA (Figure 6.15b) results may explain the difference in creatinine-induced behavior observed in these two cases.

Namely, the CV measurement occurred over a period of 10 s, which is much less than that of the CA measurement of 120 s (the onset of creatinine-induced current decease) and beyond. This is explained by a slow build-up of site blocking that has little effect at 10 s, but becomes noticeable at 120 s.

6.4 CONCLUSIONS

The electrolysis of urea and creatinine on Ni-based electrodes was investigated electrochemically at both dialysate- and urine-relevant concentrations. On a Ni foam electrode, the presence of creatinine limited urea oxidation reaction in both concentration regimes. A NHF electrode was more active towards urea oxidation, and oxidation charge was less suppressed by creatinine than for the Ni foam. A Fe-NHF electrode was most active toward both urea and creatinine oxidation, with the presence of creatinine enhancing charge during potentiodynamic experiments yet suppressing charge slightly during a 15 minute voltage hold for dialysate-relevant concentrations. This behavior is attributed to concurrent urea and creatinine electrooxidation in the presence of site blocking by creatinine, which takes noticeable effect at times greater than 120 s at 0.6 V vs. Hg/HgO.

Chapter 7. URC DESIGN AND PERFORMANCE

Nickel demonstrates superior urea oxidation reaction kinetics in alkaline solution compared to Pt in the three-electrode cell (Chapter 5). Therefore, all anodes developed for the URC were primarily Ni-based. Platinum is a highly active HER catalyst and was used as the URC cathode. To visualize the relationship between three-electrode cell experiments and the URC experiments discussed in this chapter, Figure 7.1 shows CVs for UOR/OER on Ni (red/black) and HER on Pt (grey) in 1 M KOH. When viewed on the same potential scale, the potential region from HER onset (E < 0.0 V vs. RHE) to UOR onset (E > 01.4 V vs. RHE) is 1.4 V and is approximated by the dashed lines (Figure 7.1). Therefore, a two-electrode cell that utilizes a Pt cathode and a Ni anode requires at least 1.4 V to perform UOR (at the anode) and HER (at the cathode) simultaneously.

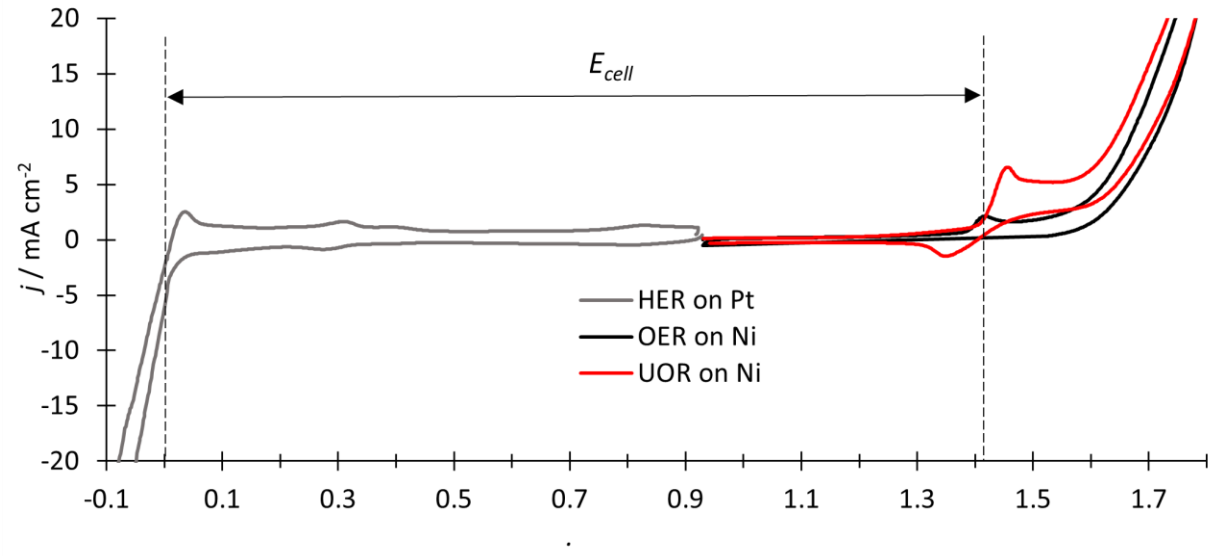

Figure 7.1 CVs showing HER on Pt (grey), OER on Ni (black), and UOR on Ni (red) in 1 M KOH and v=20 mV/s. The dashed lines approximate cell voltage (E_{cell}) for a two-electrode cell performing HER at the cathode and UOR at the anode.

Figure 7.1 accounts for electrode activation overpotentials within the three-electrode cell environment; however, activation overpotentials in the URC deviate from these due to local pH, and reactant concentration differences. Additionally, other inefficiencies and non-idealities exist in a two-electrode cell that contribute to a larger combined cell overpotential. These include electrolyte resistance to ion migration, electronic resistance due to component connections, and mass transport limitations from reactant flow channel to catalytic sites. Aside from the URC components used, there are many factors that contribute to overpotentials including the morphology of the catalyst layer, cell compression, hydration of the AEM, and operational parameters. As a result, operating URC cell voltages used in the following applied experiments vary from 1.6–2.0 V. Section 7.1 summarizes the progression of URC electrodes, with different URC configurations named according to the anode catalyst including: NiO/Pt, Ni foam, and NHF.

7.1 Electrode Progression

7.1.1 *NiO/Pt Anode URC*

A smooth Ni disk was needed to calculate UOR rates as a function of applied voltage, solute concentration, and temperature (5.3); however, URC device development requires high ECSA electrodes to maximize urea degradation rate within a portable device. Initially inspired by alkaline fuel cell and electrolyzer technology [113, 114], ink formulations were developed for both anode and cathode and sprayed with an airbrush onto an AEM to create a catalyst coated

membrane (CCM). The CCMs were made to 5 cm^2 and paired with gas diffusion layers (GDL), according to fuel cell convention. Table 7.1 summarizes the initial URC anode, cathode, and GDLs; these components combine with the AEM to form the membrane electrode assembly (MEA). Each catalyst powder was supported on carbon black (XC-72R) for high surface area and conductivity. Figure 7.2 shows SEM images of the anode catalyst layer at the magnifications noted. These micrographs reveal even catalyst layer dispersion at low magnification and well-developed microstructure at high magnification.

	Anode	**Cathode**
Catalyst	NiO/Pt (2:1)	Pt
Loading (mg/cm^2)	0.6	0.4
Catalyst Layer Components (%mass)	15% NiO 7.5% Pt 67.5% carbon black 10% PTFE binder	19% Pt 76% C black 5% PTFE binder
Gas Diffusion Layer	Ni foam	Stainless Steel Mesh

Table 7.1 URC electrodes were first developed using the catalyst coated membrane (CCM) preparation technique and a GDL on each electrode.

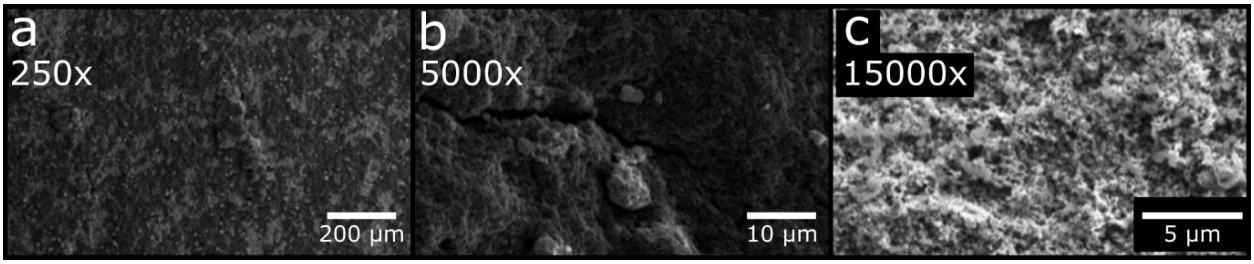

Figure 7.2 SEM images of 15% NiO/Pt supported on carbon sprayed onto AEM for URC CCM.

Utilizing the 5 cm^2 MEAs described by Table 7.1, a potential step experiment was performed on the URC from 1.3 V to 1.8 V, in 0.1 V increments for 300 s (Figure 7.1, inset). The background electrolyte used was 0.1 M $KHCO_3$ to imitate the ionic strength of dialysate with a biocompatible electrolyte. Urea concentrations of 6.25, and 20 mM were used to imitate healthy and severely uremic urea concentrations, respectively. The blank in Figure 7.1 demonstrates no significant reaction in the range of 1.3–1.5 V. The blank demonstrates an oxidation shoulder in the 1.6 V step which corresponds to the Ni^{2+} oxidation. At 1.6 V, once all the surface Ni^{2+} sites are oxidized to Ni^{3+}, current settles to 0.5 mA/cm^2. With increased cell potential to 1.7–1.8 V, OER kinetics increase in the blank. As expected, the urea-containing solutions exhibit concentration enhanced current response at 1.6–1.7 V, when Ni^{3+} surface sites are available. When 1.8 V is reached, OER dominates as indicated by all anolyte solutions exhibiting the same current response regardless of urea concentration. Oxygen evolution is favored in this URC configuration due to the presence of Pt, a well-known OER catalyst, in the anode CL (Table 7.1). Based on Figure 7.1, the ideal cell potential to maximize UOR and minimize OER is 1.6 V.

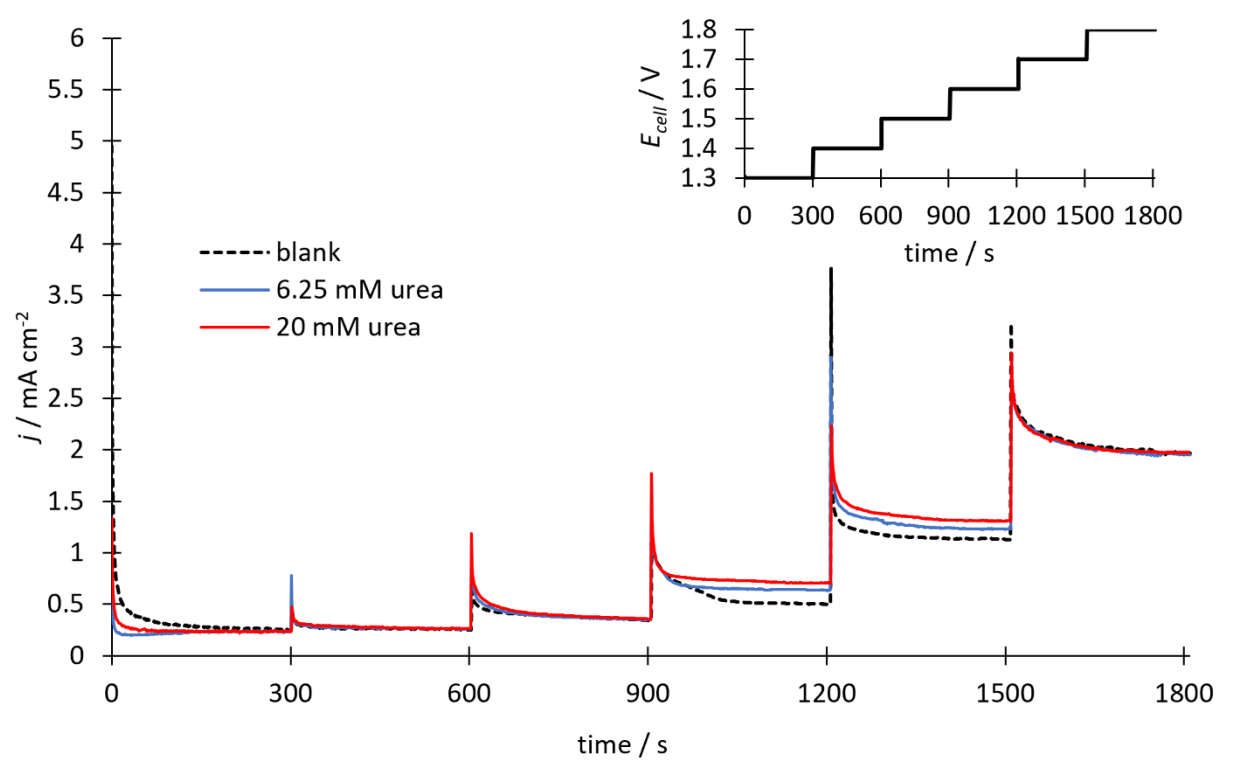

Figure 7.3 Potential step (inset) performed from 1.3–1.8 V on NiO/Pt URC with 0, 6.25, and 20 mM urea in 0.1 M $KHCO_3$. Each step held for 300 s.

To assess the urea oxidation capacity of the NiO URC, a 4-hour potential hold experiment was performed at 1.6 V with anolyte concentrations of 0, 6.25, and 20 mM urea in 0.1 M $KHCO_3$ (Figure 7.4). In agreement with Figure 7.1, the resulting current increases with urea concentration at 1.6 V. The 20 mM urea solution experiences significant reduction in current beginning at about 1 hour while the 6.25 mM urea solution exhibits more throughout the 4-hour experiment. The observed URC decline in current, particularly at 20 mM urea, is attributed to Pt poisoning. Previous three-electrode cell Pt studies (Chapter 4) conclude that Pt becomes poisoned when the electrode remains at a high potential, as enforced in the E_{hold} experiment (Figure 7.4). Concentration dependence of the poisoning is understood to be due to a higher UOR rate and

therefore a faster buildup of partial oxidation products. Additionally, as observed in Chapter 5, cell temperature plays a significant role in UOR kinetics on Ni. During these early URC experiments, temperature fluctuated from 35–40 °C. Based on the understanding of URC sensitivity to temperature, discussed further in 7.2.2, it can be assumed that current fluctuations are influenced by temperature changes.

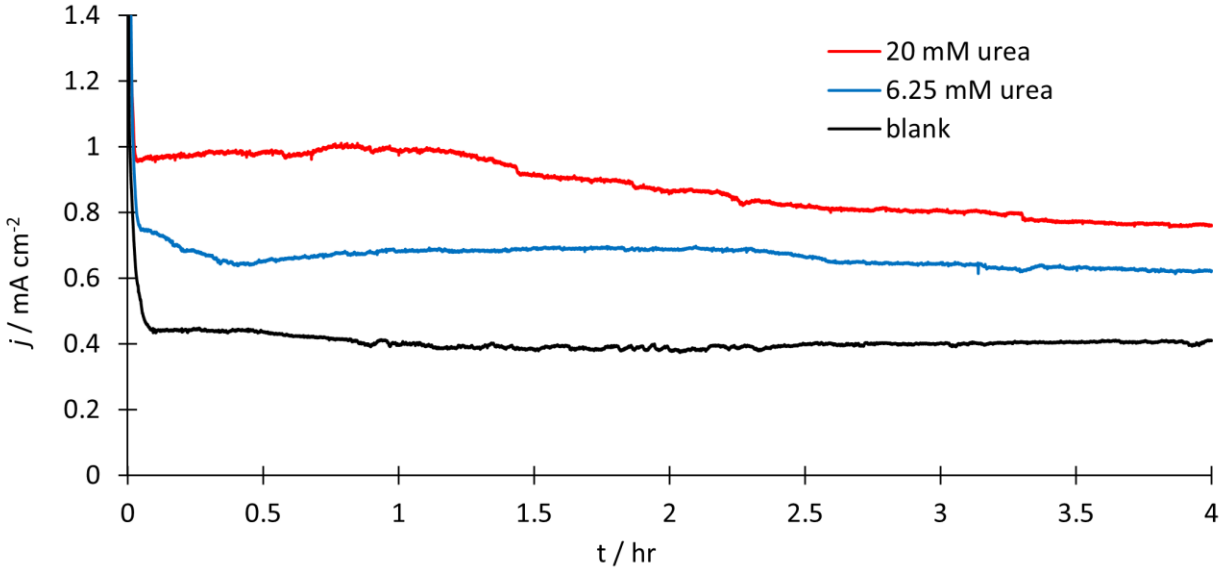

Figure 7.4 Potential hold experiment performed on NiO/Pt URC at 1.6 V for 0, 6.25, 20 mM urea in 0.1 M $KHCO_3$ to maximize UOR and minimize OER, as informed by Figure 7.3.

Based on the difference between the 6.25 mM urea and blank data in Figure 7.4, the average electrolytic current (j_{EO}) is about 0.2 mA/cm^2, which corresponds to a urea reaction rate ($\hat{r}$) of 0.075 mg/hr cm^2 (Equation 4.2) and an associated required electrode area (A) of about 8,400 cm^2 (Equation 4.3). The envisioned urea removal device has n number of 50 cm^2 cells in a stack configuration, where n is no greater than 10 to achieve portability. These initial URC results agree well with the mechanistic and kinetic insights gained in the three-electrode cell

experiments on Pt and Ni; however, the low $\hat{r}$ corresponds to significant electrode area required to remove 15 g urea/day from a patient (Table 7.2) and thus motivates further electrocatalyst improvements.

Urea concentration (mM)	6.25
$\boldsymbol{j_{EO}}$ **(mA/cm^2)**	0.2
Anode	NiO/Pt (2:1)
$\hat{r}$ **(mg/hr cm^2)**	0.075
$\boldsymbol{A}$ **(cm^2)**	8,400
$\boldsymbol{n}$	168

Table 7.2 Summary of NiO/Pt URC performance over 4-hour potential hold at 1.6 V. The urea electrooxidation current (j_{EO}) is used to calculate approximate device dimensions of A and n number of 50 cm^2 cells.

7.1.2 *Ni Foam Anode URC*

Although GDLs are not conventionally used in water electrolyzers [115], their incorporation in early experiments was coincidentally beneficial for URC development. Cell performance increased when Ni foam was used as the anode GDL, in tandem with a sprayed NiO/Pt anode catalyst layer (Table 7.1). And, surprisingly, when two Ni foam layers were used, the URC current further improved. This result implied that Ni foam was providing a reacting surface and performing UOR directly within the anolyte solution. To test the hypothesis, Ni foam painted with ionomer was pressed directly against the AEM for use as a catalyst. Additionally, ionomer was used in the Pt ink recipe and loading was increased to 1.0 mg Pt/cm^2 (Table 7.3) to limit HER activation overpotential at the cathode. The anionic exchange ionomer on the anode and cathode allows the activity of OH^- to remain high at the reacting sites without highly alkaline anolyte solution. The resulting URC configuration is summarized in Table 7.3 and referred to as the Ni foam URC.

	Anode	Cathode
Catalyst	Ni	Pt
Loading (mg/cm^2)	N/A	1.0
Catalyst Layer Components (%mass)	Ni foam painted with ionomer	19% Pt 76% C black 5% ionomer
Gas Diffusion Layer	N/A	Stainless Steel Mesh

Table 7.3 The anode sprayed CL was replaced with Ni foam and painted with ionomer. Additionally, Pt ink was made with ionomer rather than PTFE binder, and loading was increased to 1.0 mg/cm^2.

Figure 7.5a shows the current response to a potential stair-step experiment performed on the Ni foam URC from 1.2–1.85 V (inset) at 0 and 6.25 mM urea in 0.1 M $KHCO_3$. Low voltages (E_{cell} < 1.4 V) and smaller voltage steps were included in these experiments to establish formation of ionic pathways in the ionomer and AEM, which benefit from a slow, gradual potential increase [116]. Beginning at a cell voltage of 1.45 V, the urea solution provides higher currents than the blank, marking the onset of UOR. The increasing current density observed during potential steps beginning at 1.7 V resembles that of URC break-in procedure results. The break-in procedure, detailed in Appendix E, is performed prior to other experiments for new MEAs and establishes ionic channels within the AEM and ionomer. Break-in success is confirmed by lower overall cell resistance. The observance of current instability in Figure 7.5a indicates that the painted ionomer anode did not achieve ionic conductivity sufficient to support current densities above 5 mA/cm^2. As a result, ionic gradients formed during URC operation as OH^- anions replaced the $Br^-/HCO_3^-/CO_3^{2-}$ ions within the ionomer. These transient gradients eventually disappear with continued use as Br^- is flushed from the ionomer and a steady state flux of OH^- becomes established. Figure 7.5b shows the j_{EO} for 6.25 mM urea at each voltage step. Although overall current increases with higher potentials (Figure 7.5a) there is no enhancement in UOR for 6.25 mM urea past 1.65

V (Figure 7.5b). It is therefore concluded that a cell potential of 1.65 V maximizes UOR while minimizing OER.

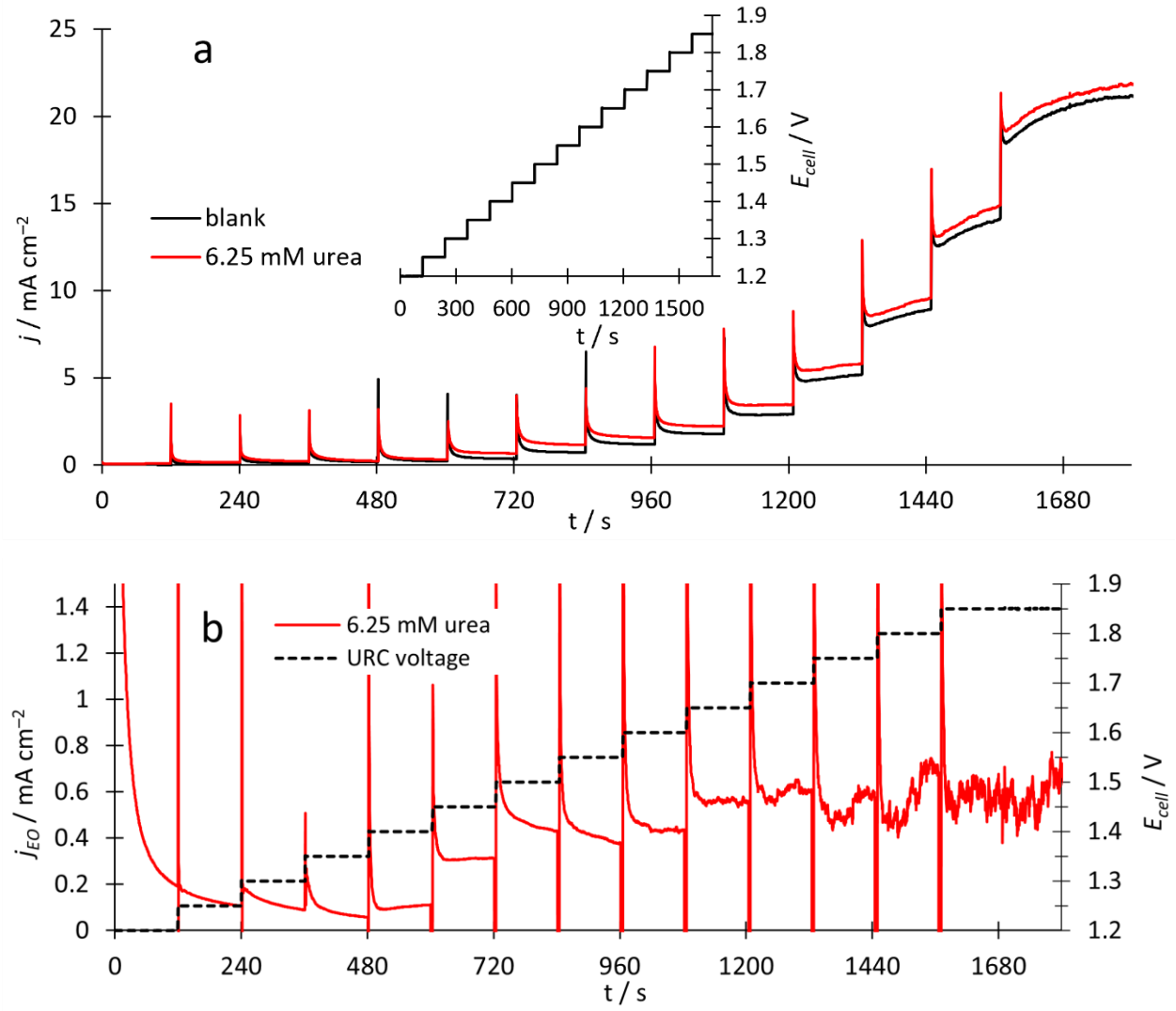

Figure 7.5 a) Current response to a potential step performed on Ni foam URC from 1.2–1.85 V on URC (inset) with 0 and 6.25 mM urea in 0.1 M $KHCO_3$, and b) the resulting j_{EO}.

A series of potential hold experiments were performed on the Ni foam URC at 1.65 V for 30 minutes (Figure 7.6a). The blank and red 6.25 mM urea curves were performed at 5.3 ml/min anolyte flowrate (Q), while the blue 6.25 mM urea curve was subjected to increasing Q every 10

minutes, as shown in Figure 7.6b. The constant flow 6.25 mM urea exhibits an average j_{EO} = 1 mA/cm^2. The same 6.25 mM urea concentration reaches a maximum total current density of 3.6 mA/cm^2 at 16 ml/min. The summary of UOR performance for the Ni foam URC is provided in Table 7.4 where 1 mA/cm^2 is used for j_{EO} to ensure flowrate enhancement is not included when comparing against the 5.3 ml/min blank. Overall, the Ni foam URC configuration demonstrates lower UOR onset and improved overall reaction rates compared to the NiO/Pt URC configuration.

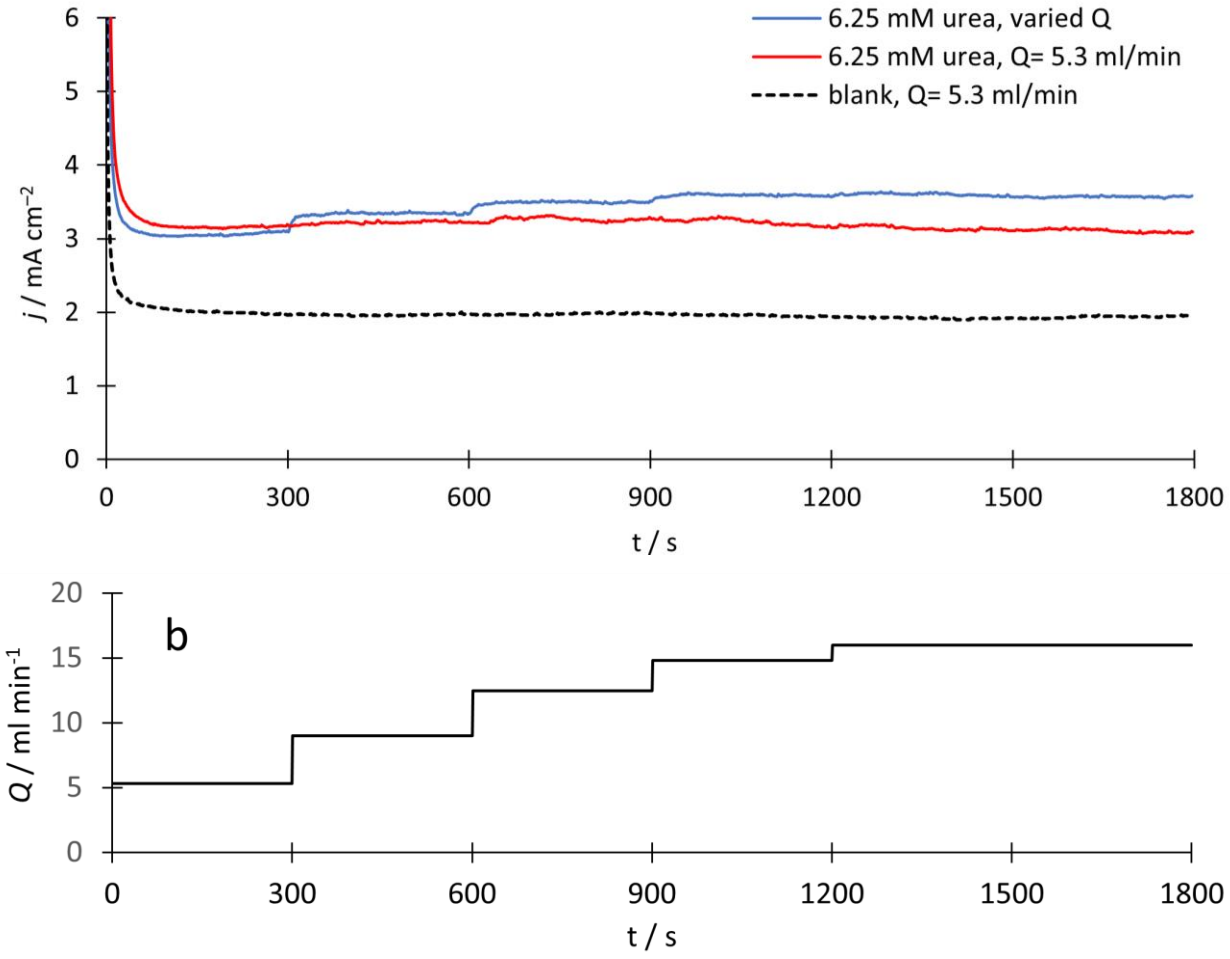

Figure 7.6 a) Potential hold experiment performed on Ni foam URC at 1.65 V for 0 and 6.25 mM urea in 0.1 M $KHCO_3$ to maximize UOR and minimize OER, as informed by Figure 7.5, and b) the flowrate (Q) over time for the "varied Q" curve.

Urea concentration (mM)	6.25
$\boldsymbol{j_{EO}}$ **(mA/cm²)**	1.0
Anode	Ni foam and ionomer
$\hat{r}$ **(mg/hr cm²)**	0.373
$\boldsymbol{A}$ **(cm²)**	1680
$\boldsymbol{n}$	34

Table 7.4 Summary of Ni foam URC performance during 30 minute potential hold at 1.65 V (Figure 7.6). The measured j_{EO} is used to calculate $\hat{r}$ and approximate device dimensions A and n.

In addition to improvements in UOR, skipping the anode spraying process minimizes electrode preparation time. In an effort to omit spraying altogether, a Pt/C ink painted Ni foam cathode was tested. Although the preparation time decreased and the electrochemical performance was maintained, the cell durability suffered on account of frequent AEM punctures. The improved urea reaction rates in the Ni foam URC compared to that of the NiO/Pt are largely attributed to higher electrode surface and flow within the porous Ni foam, which may help decrease the diffusion layer adjacent to the electrode to improve urea transport. These promising results motivated the development of a more active urea oxidation catalyst upon the same, porous Ni foam substrate.

7.1.3 *NHF Anode URC*

A hydrothermal method was adapted (Appendix A) to grow $Ni(OH)_2$ on Ni foam for URC anodes. The NHF anodes both improve UOR kinetics and increase the ECSA compared to Ni foam (Chapter 6). Additionally, the cathode CL was sprayed onto carbon cloth to create gas diffusion electrodes (GDE, Appendix B) instead of CCMs. The CCM preparation technique resulted in ~20% damaged AEMs prior to mounting into the URC. Fabrication of electrodes that are separate from

the AEM enables electrode replacement separate from AEM replacement. As a result, AEMs are used for months and show fantastic durability when kept hydrated. Table 7.5 summarizes the NHF URC.

	Anode	**Cathode**
Catalyst	$Ni(OH)_2$	Pt
Loading (mg/cm^2)	1.0	1.0
Catalyst Layer Components (%mass)	NHF	19% Pt 78% C black 3% ionomer
Gas Diffusion Layer	N/A	Carbon cloth

Table 7.5 Summary of electrodes used in the NHF URC. The anode is hydrothermally grown NHF, and the cathode is a Pt CL sprayed onto the carbon cloth GDL rather than the AEM directly. Each electrode active area is 25 cm^2.

Figure 7.7 shows the results of a potential step experiment performed on the NHF URC with 0, 2, and 6.25 mM urea in 0.1 M $KHCO_3$. When subjected to a potential step experiment, the NHF URC exhibits superior reaction rates and UOR stability compared to the NiO/Pt and Ni foam URC iterations. Figure 7.7 demonstrates an oxidation onset of 1.45 V for the 6.25 mM urea solution. The j_{EO} for each urea concentration and E_{cell} are plotted as a function of time in Figure 7.7b. Unlike the high voltage trends for NiO/Pt URC (Figure 7.3) and Ni foam URC (Figure 7.5), UOR rate appears to increase along with OER through a final cell voltage of 1.85 V. The maximum j_{EO} for 6.25 mM urea is about 3.5 mA/cm^2 which occurs at a cell voltage of 1.85 V, as listed in Table 7.6.

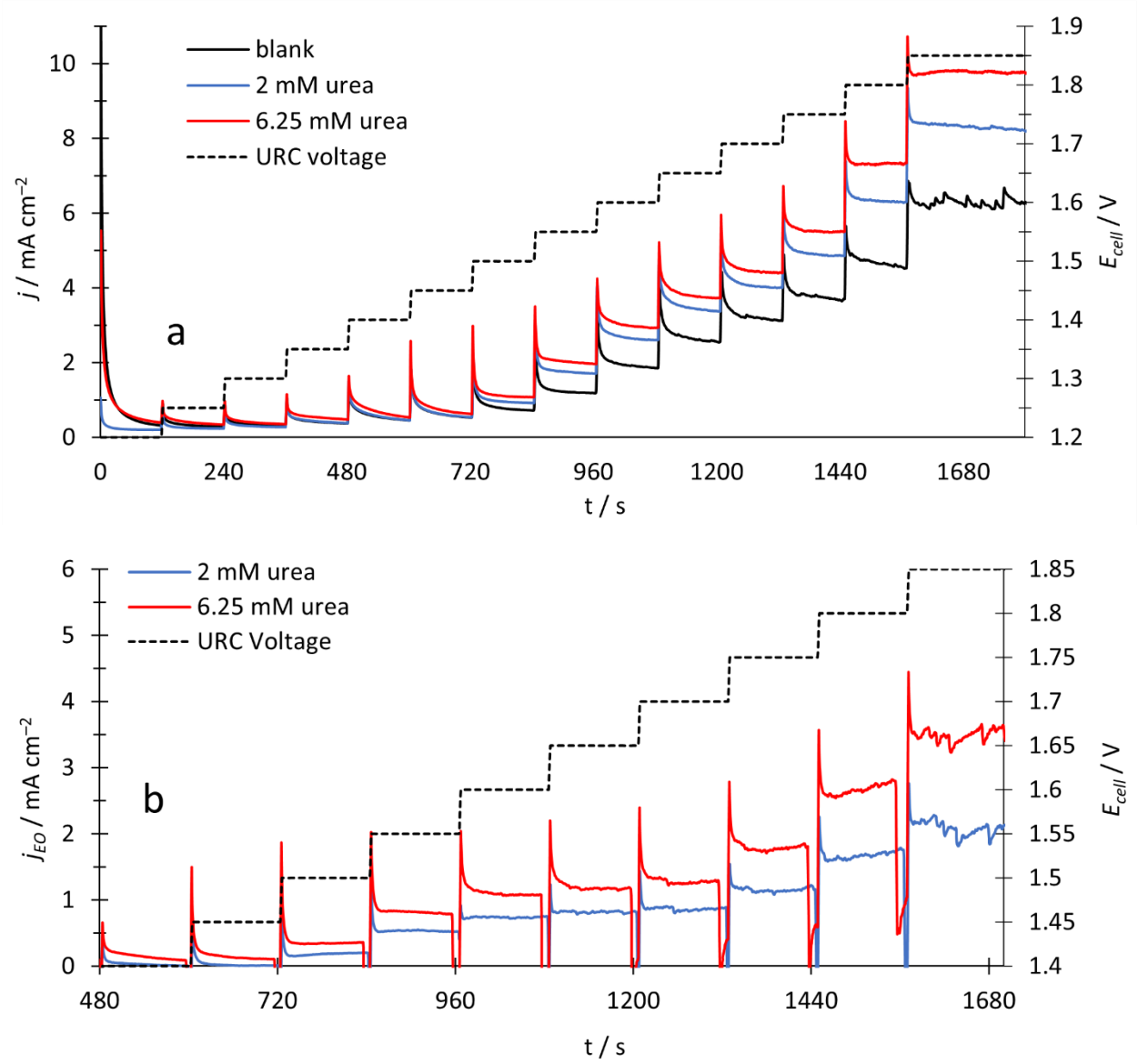

Figure 7.7 a) Potential step from 1.20–1.85 V in 50 mV increments for 120 s performed on the NHF URC with 0, 2, and 6.25 mM urea in 0.1 M $KHCO_3$ and b) the resulting j_{EO} at E_{cell} > 1.4 V for 2 and 6.25 mM urea.

In summary, the NHF URC significantly outperforms the sprayed NiO/Pt and the Ni foam catalyst configurations (Table 7.6). The NHF anode improves UOR kinetics within the URC to reach a manageable required electrode area of less than 500 cm^2. The fabrication methods for each

electrode utilizes techniques that provide the most durable URC and are more easily scaled than spraying CCMs. It takes one researcher about two days to produce ten 50 cm^2 anodes and cathodes. Throughout the remainder of this document the URC refers to the NHF URC configuration.

Urea concentration (mM)	6.25
j_{EO} (mA/cm²)	3.5
Anode	NHF
$\hat{r}$ (mg/hr cm²)	1.3
A (cm²)	480
Number of 50 cm² cells	10

Table 7.6 Summary of NHF URC performance and design dimensions based on the measured j_{EO} at 1.85 V at 18 ml/min.

7.2 Anolyte Control and Sensitivity

The experiments reported in 7.1 were all performed at temperatures between 35–40 °C in 0.1 M $KHCO_3$, and anolyte flowrates of 5–20 ml/min. With a working URC prototype established, the sensitivity of cell performance to background electrolyte, temperature, pH, and flowrate are summarized in this section.

7.2.1 *Background Electrolyte*

The presence of a background electrolyte affects the URC ohmic resistance (R_{ohm}) which can be measure via polarization curve (Figure 7.8a) and electrochemical impedance spectroscopy (EIS, Figure 7.8b). The linear region of the polarization curve for each anolyte (dotted lines with noted slope, Figure 7.8a) represents the total URC ohmic resistance, including both electric and

ionic resistances. The same cell was use for all measurements in Figure 7.8 and therefore it is assumed that differences in ohmic resistance are solely attributed to changes in ionic resistance, both within the AEM and the liquid anolyte. The R_{ohm} measured for each anolyte is listed in Table 7.7. Pure water has a cell resistance of 19.5 Ωcm^2, about three times higher than the 0.1 M KOH and 0.1 M $KHCO_3$. Additionally, the 0.1 M $KHCO_3$ solution has a slightly higher R_{ohm} compared to that of the same ionic strength KOH. This is due to the reduced conductivity of the AEM in a mixed $CO_3^{2-}/HCO_3^-/OH^-$ form compared to a fully hydroxylated AEM [117]. The more dramatic effect between the $KHCO_3$ and KOH polarization curves is due to the high activation overpotential observed in the former electrolyte, which is about 0.4 V larger than the KOH (Figure 7.8a). This observation agrees with alkaline electrolyzer modeling results that report an accumulation of HCO_3^-/CO_3^{2-} at the anode, as these anions do not partake in alkaline OER. As a result, there exists a Nernstian voltage loss due to the pH gradient across the membrane, which requires a larger overpotential to overcome [115].

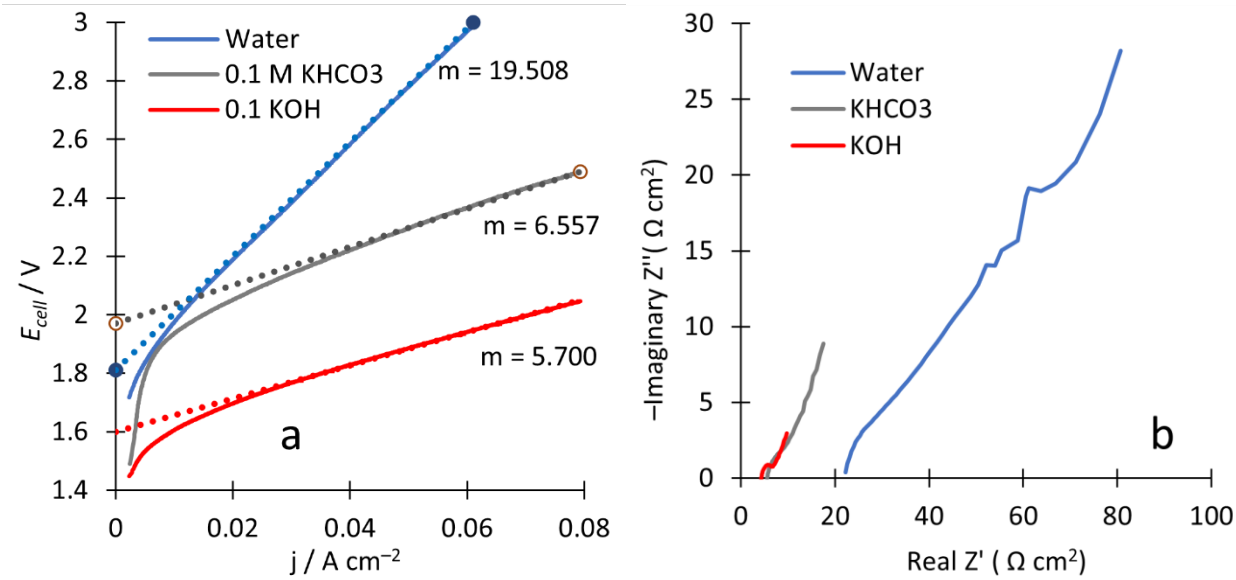

Figure 7.8 The data show two methods for measuring URC ohmic resistance (R_{ohm}) including a) polarization curves and b) EIS performed on the URC with the listed anolytes at a flowrate of 20 ml/min and temperature of 37 °C. EIS was performed at 1.5 V from 10^3 Hz-0.1 Hz using a 5 mV perturbation.

The EIS results (Figure 7.8b) generally confirm those observed in the polarization curve. A perturbation of 5 mV was applied at a 1.5 V bias, where OER onset occur in the URC. The high frequency intercept with the real Z' axis provides a measurement for R_{ohm}, listed in Table 7.7. In reasonable agreement with Figure 7.8a, EIS reveals minimal change in R_{ohm} between the KOH and $KHCO_3$ electrolytes and a large increase in cell resistance when pure water is fed to the URC anode. Based on these results, it becomes clear that the anionic species in the AEM and ionomer play a subtle role in ionomer conductivity and a more significant role in establishing local pH gradients at the anode surface. For this reason, and to mimic the total ionic strength of dialysate fluid, 0.1 M $KHCO_3$ is used as anolyte background electrolyte for the remainder of URC experiments in this chapter.

	water	**0.1 M $KHCO_3$**	**0.1 M KOH**	**source**
R_{ohm} **(Ω cm²)**	19.5	6.6	5.7	Figure 7.8a
R_{ohm} **(Ω cm²)**	22.5	5.5	4.3	Figure 7.8b

Table 7.7 Comparison of URC ohmic resistance measurements using polarization and EIS (Figure 7.8).

7.2.2 *Temperature and pH*

Precise control of cell temperature, anolyte temperature, and anolyte pH are crucial during URC operation because the UOR rate is increased at higher temperatures and pH.

Analyzing the effects of anolyte flowrate on urea removal rate (7.2.3) is not productive without precise control and understanding of the system pH and temperature. A typical 6-hour URC experiment under pH and temperature control is shown in Figure 7.9. Human body physiological temperature of 37 °C and pH of 7.4 are used. It takes about 2 hours to slowly heat the anolyte feed solution from 22 °C to 37 °C (green circles, Figure 7.9). As the anolyte temperature approaches 37 °C, the pH (red squares, Figure 7.9) is set to 7.4 using a CO_2 sparge described in Chapter 3. Once the pH and anolyte temperature reach their setpoints, voltage is applied to the URC and the experiment runs for 6 hours while anolyte temperature, URC temperature, and anolyte pH are controlled, and current density is measured. Controlling the pH and temperature of the anolyte increases the stability of the measured current density, which can achieve constant current for many hours.

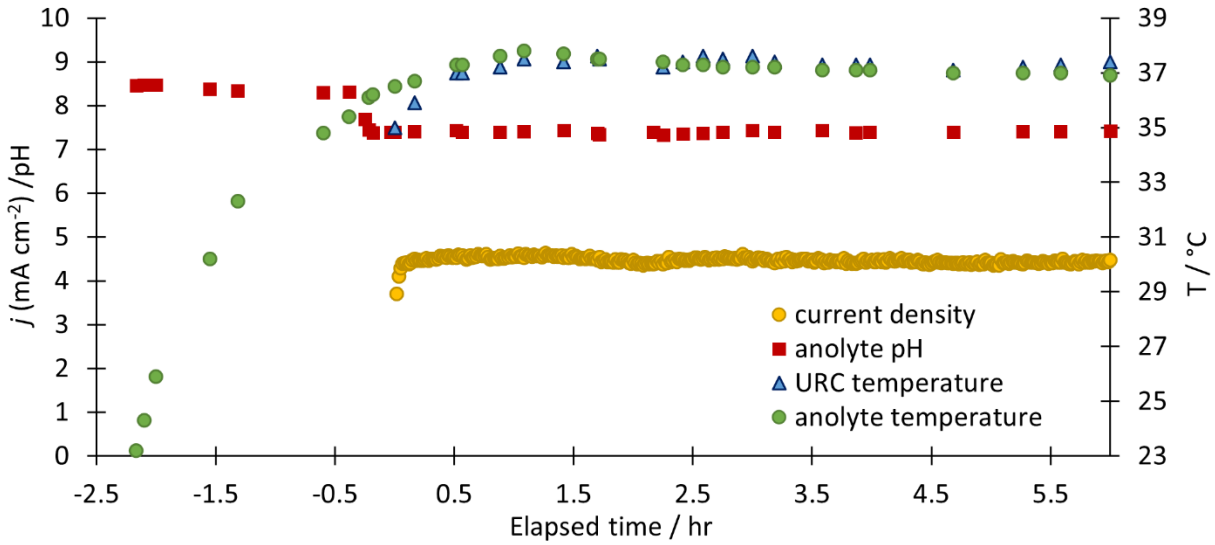

Figure 7.9 Anolyte feed temperature, URC temperature, anolyte pH, and current density before and during a 6-hour 1.9 V URC potential hold. The cell voltage was applied at 0 hr. Current density and pH share the primary y-axis and temperature is shown on the secondary y-axis.

Recording the temperature and pH throughout a long experiment enables a qualitative current sensitivity analysis to be performed as against cell temperature, anolyte feed temperature, and anolyte pH. Although pH is temperature dependent, the reported values have been temperature compensated using the anolyte feed temperature, where pH is measured. Figure 7.10 shows the same data plotted in Figure 7.9 from 0 to 6 hours. The small scale used for each variable in Figure 7.10a–c enables the observation how small fluctuations in the controlled variables correlate with the measured current density. Based on Figure 7.10a, it is evident that the anolyte feed temperature has less effect on current density compared to anolyte pH (Figure 7.10b) and URC temperature (Figure 7.10c). The gradual relaxation of the anolyte temperature from about 38 °C (1 hr) to 37 °C (6 hr) has no apparent correlation with current density during the same time. In contrast, a smaller, more rapid URC temperature decline by 0.5 °C around hour 2 is strongly correlated with decreased current at the same time. Once inside the URC, the cell temperature overrides anolyte feed temperature and therefore a stronger relationship between j and T_{cell} is observed compared to T_{feed}. Furthermore, anolyte temperature exhibits the most stability due to the large 4 L reservoir size and heat capacity. The dip in current observed around hour 2 is also tracked by pH (Figure 7.10b). These trends support the conclusions from previous three-electrode studies that confirm a strong dependence on both temperature and pH for UOR on Ni. Data from a different 1.9 V pH- and temperature-controlled URC experiment is provided in Figure 7.11. The data agree with Figure 7.10, which reveal a correlation of T_{feed} > pH > T_{cell}.

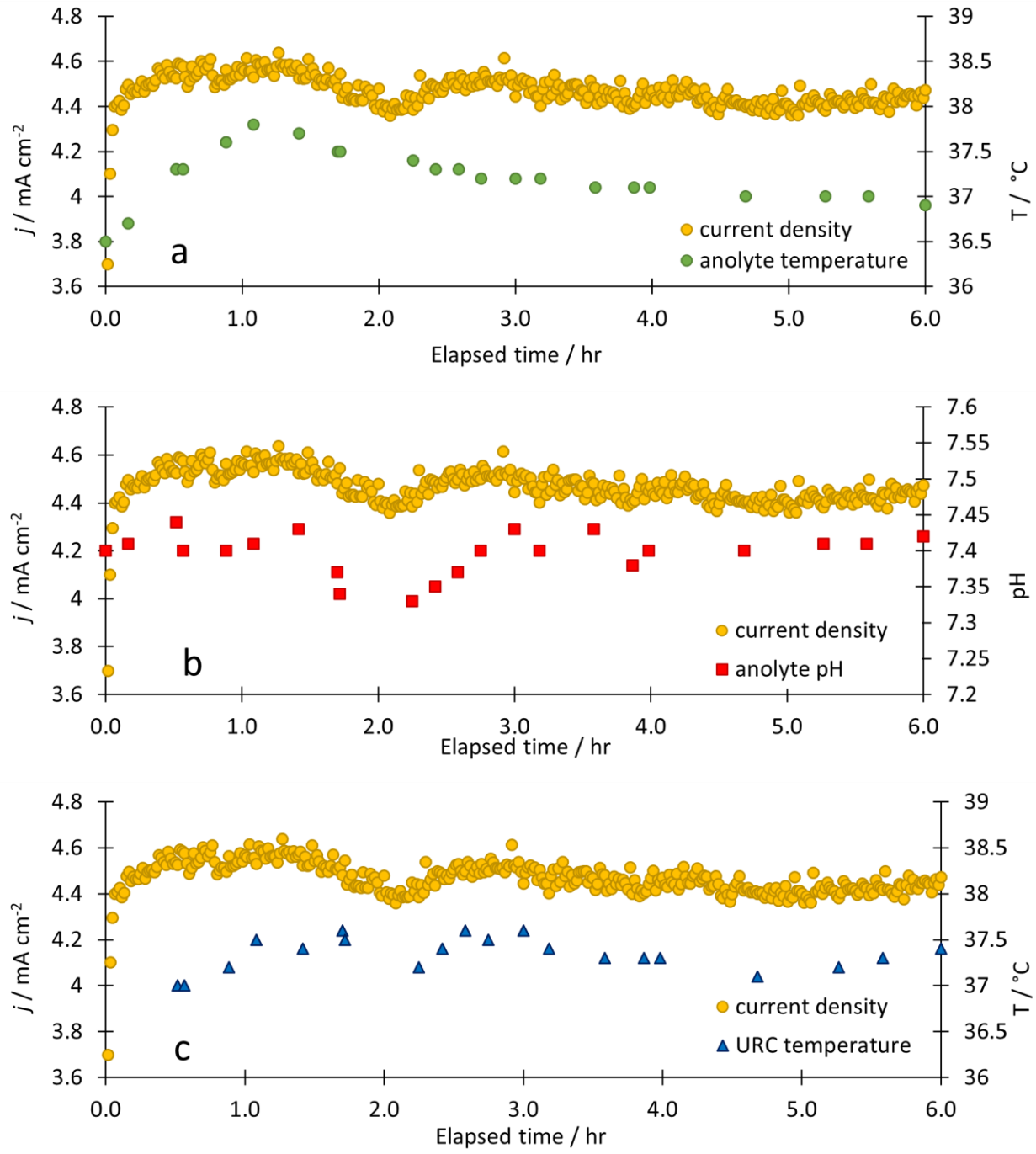

Figure 7.10 Current density sensitivity to a) anolyte feed temperature, b) anolyte pH, and c) URC temperature plotted over a 6-hour URC experiment at 1.9 V. The scale on each plot is smaller than Figure 7.9 to track how small fluctuations affect current density. Current density is plotted on the primary y-axis, pH and T are plotted on the secondary y-axis.

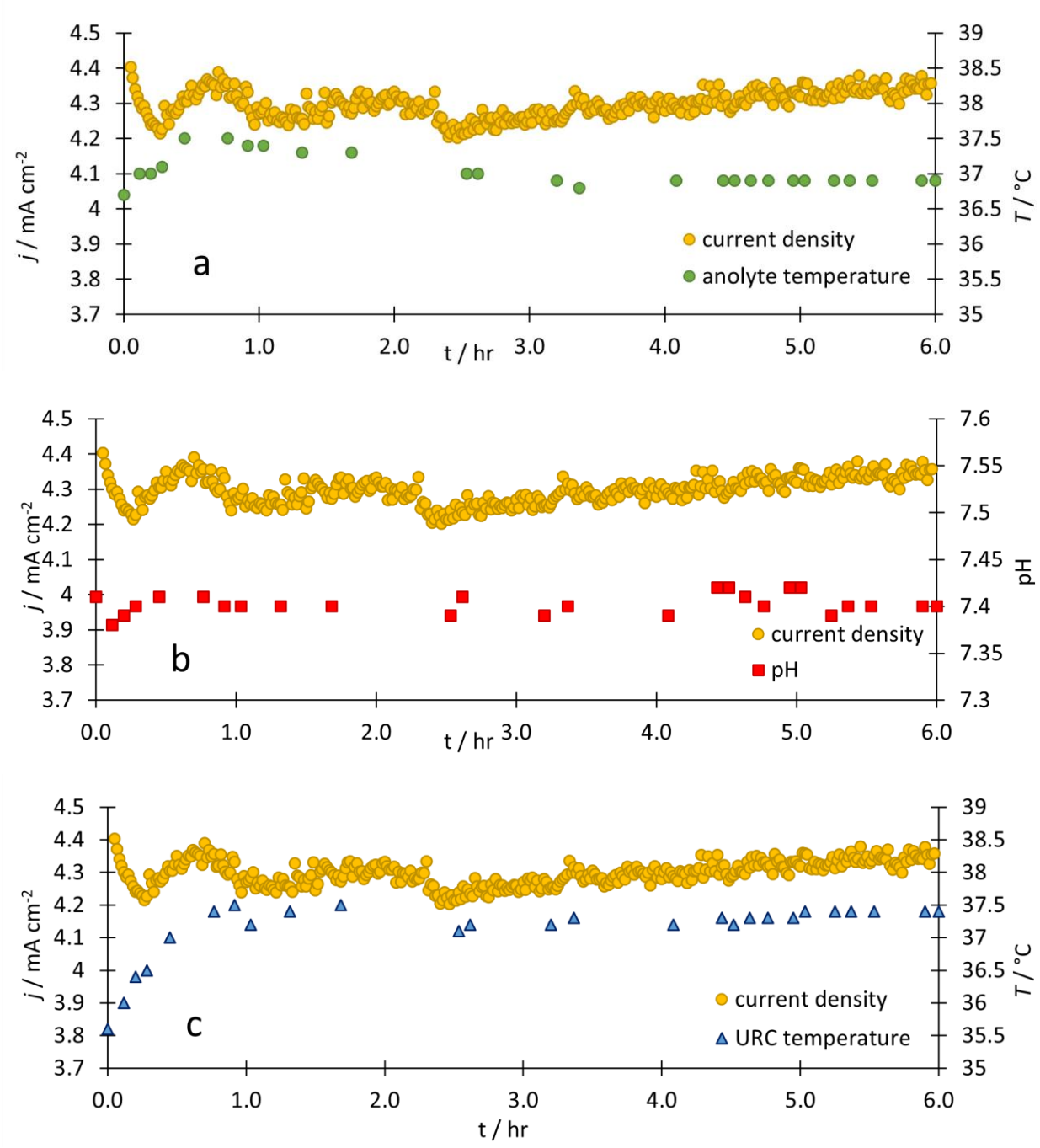

Figure 7.11 Current density sensitivity to a) anolyte feed temperature, b) anolyte pH, and c) URC temperature plotted over a 6-hour URC experiment at 1.9 V. Current density is plotted on the primary y-axis, pH and T are plotted on the secondary y-axis.

7.2.3 *Flowrate Effect on Urea Degradation*

An analysis of URC flowrate constraints within a portable device and the effect of acceptable flowrates on urea removal rate is discussed in this section. Figure 7.12 shows a simplified process flow diagram of regenerative dialysis including a blood loop, dialysate loop, and a recirculation loop within the dialysate loop to account for a low conversion reactor. The flow rate of solution coming out of the dialyzer (Q_1) is 17 ml/min assuming a dialyzer exit flow concentration of 10 mM urea and a total mass of 15 g urea/day. Therefore, when a recirculation loop is included, Q_2 > 17 ml/min. Additionally, maximum flowrate into the device should not exceed 400 ml/min due to safe dialysate flowrates. The portable urea removal device has n cells, each with individual, parallel flow channels. Therefore, the flowrate within any given cell is $\frac{Q_2}{n}$. The number of cells, n, required in the device should not exceed 10 and depends on the urea removal rate per cell. Based on the above constraints and assuming n =10, the flow within each cell must be 2–40 ml/min.

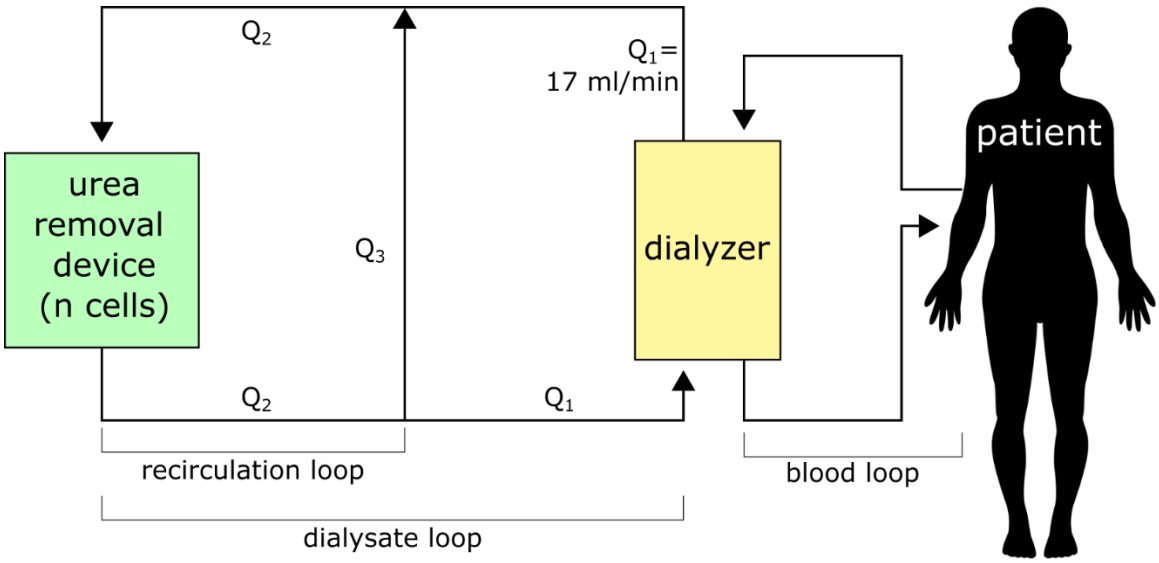

Figure 7.12 The simplified process flow diagram for regenerative dialysis including a blood loop, dialysate loop, and recirculation loop. Based on the qualification that Q_1 =17 ml/min, $Q_2 > Q_1$, and $Q_2 < 400$ ml/min, the flowrate through each of ten cells within the device must be 2–40 ml/min.

While operating under temperature- and pH-controlled conditions, the effect of flowrate was analyzed during experiments in the URC at a constant potential of 1.9 V. The initial urea concentration was 10 mM and final concentration was measured directly at the end of each experiment. The urea removal rate ($\hat{r}$) is plotted in Figure 7.13 on the primary y-axis and the associated total electrode area required to remove 15 g urea per day is also calculated for each flowrate and plotted on the secondary y-axis. The error bars represent standard deviations based on 3–6 urea concentration measurements from the same experiment. The results reveal that increasing flowrates in the 20–40 ml/min regime results in a slight positive effect on total urea degraded. Furthermore, a low flow rate of 3 ml/minute (two separate experiments performed) decreases $\hat{r}$ by more than 50%. Flowrate experiments in the 3–20 ml/min flow regime were not

performed. The decreased performance of the URC at low flowrates could be due to mass transport limitations as observed in Chapter 5. It is likely that the high porosity of the Ni foam substrate, in combination with flowrates of at least 20 ml/min, disrupt and minimize the urea diffusion layer within the anode to enable higher reaction rates.

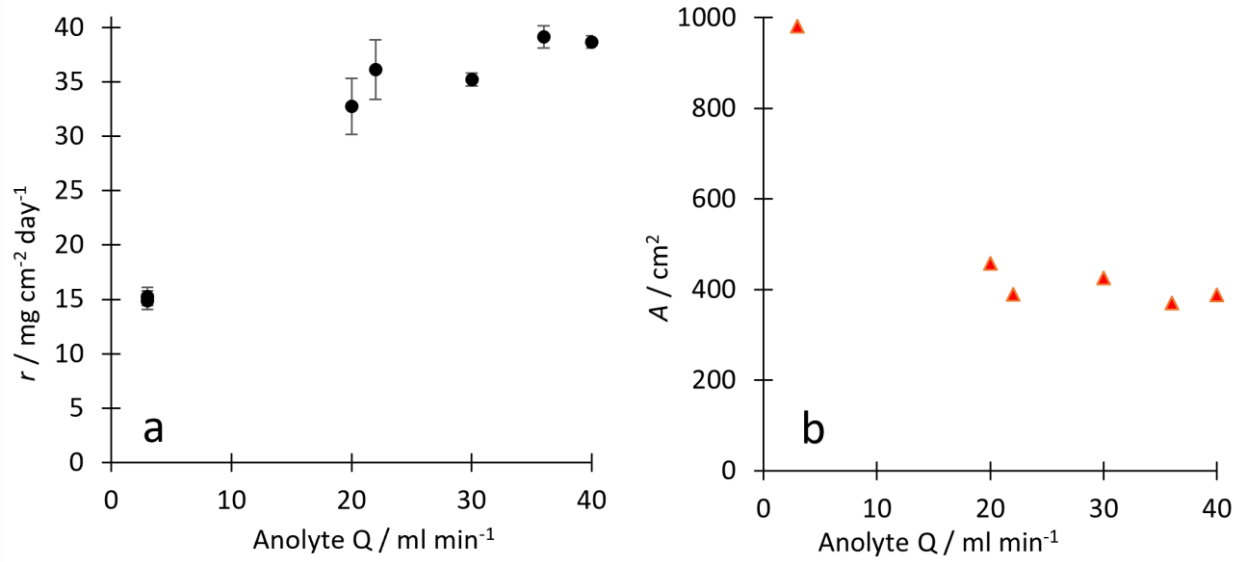

Figure 7.13 a) The urea removal rate, $\hat{r}$, and b) associated total area required to remove 15 g/day (A) is shown as a function of anolyte flowrate from 3–40 ml/min. Data collected during 1.9 V URC experiments under pH and temperature control and summarized in Table 7.8.

Q (ml/min)	$\hat{r}$ (mg/ day cm^2)	A (cm^2)	n
3	14.9	1007	21
3	15.3	981	20
20	32.8	458	10
22	36.2	389	8
30	35.2	426	9
36	39.1	370	8
40	38.7	388	8

Table 7.8 Summary of specific urea removal rates ($\hat{r}$), required electrode area (A), and number of 50 cm^2 cells (n) to remove 15 g urea/day at flowrates 3–40 ml/min, based on Figure 7.13 .

The flow analysis results, summarized in Table 7.8, indicate that a urea removal device operating under pH- and temperature-control in 0.1 M $KHCO_3$ can achieve 15 grams urea removal in 24 hours when n = 10 (50 cm^2) cells and Q > 20 ml/min. Experiments were not performed for longer than 6 hours due to the involvement of multiple manual controls and a 2 hour heating period. However, many different 6-hour experiments were performed on the same URC, with consistent results indicating that NHF electrodes maintain their urea oxidation activity throughout the aging process.

Chapter 8. NICKEL CORROSION

A switch of anolyte background electrolyte to more closely represent dialysate introduced corrosion issues in the URC. Human serum contains 0.137 M NaCl and only 25 mM $KHCO_3$. To more accurately mimic serum chloride concentration, the URC background electrolyte was switched from 0.1 M $KHCO_3$ to 0.1 M NaCl and operated at 2.0 V and 37 °C. After 1 hour of operation, the anolyte feed solution had turned green, a color signifying the presence of Ni^{2+} ion in the solution due to corrosion. Figure 8.1 shows a photograph of the Ni foam anode before (a) and after (b) this experiment. Without any pH or chloride concentration precautions, the URC was unknowingly subjected to severely corrosive conditions. Before performing further URC experiments, the three-electrode cell was first employed to study chloride-induced Ni corrosion.

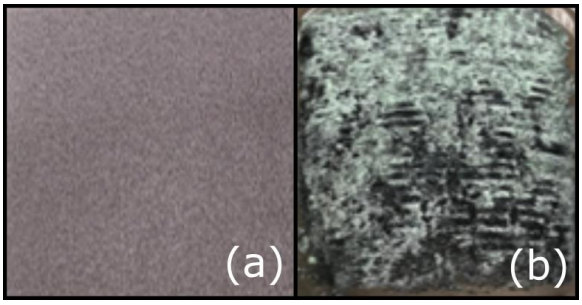

Figure 8.1 Photographs of a) Ni foam before use in URC, and b) corroded Ni foam anode after use in URC at 2.0 V for 1 hour with 0.1 M NaCl background electrolyte and 10 mM urea. Green deposits may be $NiCl_2$ or $Ni(OH)_2$ from Ni corrosion in neutral Cl^- solution (see Reaction 8.2).

The two primary forms of Ni corrosion in an aqueous environment are dissolution and pitting corrosion. Nickel dissolution is oxidation of Ni metal to form Ni^{2+} ions in solution and is

described by Reaction 8.1. Nickel dissolution to produce 10^{-6} M Ni^{2+} occurs at potentials above –0.40 V vs. SHE, independent of pH [118]. At an electrode voltage of 0 V vs. SHE, a neutral to alkaline medium transforms Ni into a mixed surface phase of $Ni(OH)_2$/NiO. This oxidized surface phase passivates the bulk Ni material through growth of a subsurface NiO layer species. Increased electrode potentials above 1.3 V vs. SHE oxidize the NiO/$Ni(OH)_2$ phase further into NiOOH, Ni_3O_4, and NiO_2. In summary, when pH and potentials create an environment that energetically favors an oxidized phase of Ni, a passivation layer protects the surface against dissolution.

$$\mathrm{Ni}_{(\mathrm{s})} \rightarrow \mathrm{Ni}^{2+}_{(aq)} + 2e^{-} \tag{8.1}$$

The presence of chloride is known to cause *pitting corrosion* in most metal/aqueous environments [119–121]. Pitting corrosion is a localized, accelerated form of corrosion that occurs when an oxide, organic, or otherwise passivating layer is penetrated and dissolution proceeds within the “pit”. The localized pit environment may have completely different solute concentrations compared to the bulk solution and create extremely corrosive environments. Although the mechanism for chloride-induced pit nucleation is not well understood, it can be caused by physical passive layer breakdown or chemical attack [122]. Once formed, propagation may proceed according to Reactions 8.1–8.2 [121]. Initially, metal dissolution (Reaction 8.1) occurs within the nucleated pit which causes the pit to achieve a relative positive charge compared to the surrounding environment when the electrons travel to a local cathode. In response, chloride ions migrate to the pit and react chemically according to Reaction 8.2, which lowers the pH and encourages further dissolution.

$$\mathrm{NiCl}_{2(aq)} + 2\,\mathrm{H_2O} \rightarrow \mathrm{Ni(OH)}_{2(aq)} + 2\mathrm{HCl}_{(aq)} \tag{8.2}$$

Although Reaction 8.2 does not involve charge transfer, the associated reduction in local pH favors dissolution, which is electrochemical and therefore increases current. Because of the localized and accelerated nature, pitting corrosion results in erratic current spikes and irregularities, and the affected surface area can be accompanied by larger diameter, hidden pits beneath the surface. Low chloride concentration and high pH are ideal conditions to avoid pitting corrosion formation and propagation. Ratios of chloride to hydroxide concentrations are therefore sometimes used to describe solutions that will prevent corrosion, which vary based on type of metal, temperature, and pit environment [119, 121].

8.1 Corrosion of Nickel Disk Working Electrode

To understand what effect $KHCO_3$ has on Ni corrosion, CVs were performed on a Ni disk in 100 mM $KHCO_3$ and 25 mM $KHCO_3$ (Figure 8.2a,b). The blank scans have no NaCl and are compared against 0.15 M NaCl in the same concentration of $KHCO_3$. In both cases the Ni^{2+}/Ni^{3+} peaks are observed. With 100 mM $KHCO_3$, there is also an oxidation peak at 1.9 V vs. RHE which is due to the reversible formation of a $NiCO_3$ layer, reported previously for Ni electrodes in bicarbonate solutions [123, 124]. Although 25 mM $KHCO_3$ does not exhibit the $NiCO_3$ peak in Figure 8.2b, the $NiCO_3$ layer reversibly grows with a gradually increased anodic potential limit and cycling (discussed below, in reference to Figure 8.4). This peak is referred to as the carbonate peak. When 0.15 M NaCl is incorporated into the 100 mM $KHCO_3$ solution, the intensity of all three oxidation and reduction peaks increase and maintain their electrochemical reversibility and

stability over three scans. It is therefore concluded that the carbonate layer formed on Ni in 100 mM $KHCO_3$ provides a corrosion protection against 0.15 M NaCl at 22 °C.

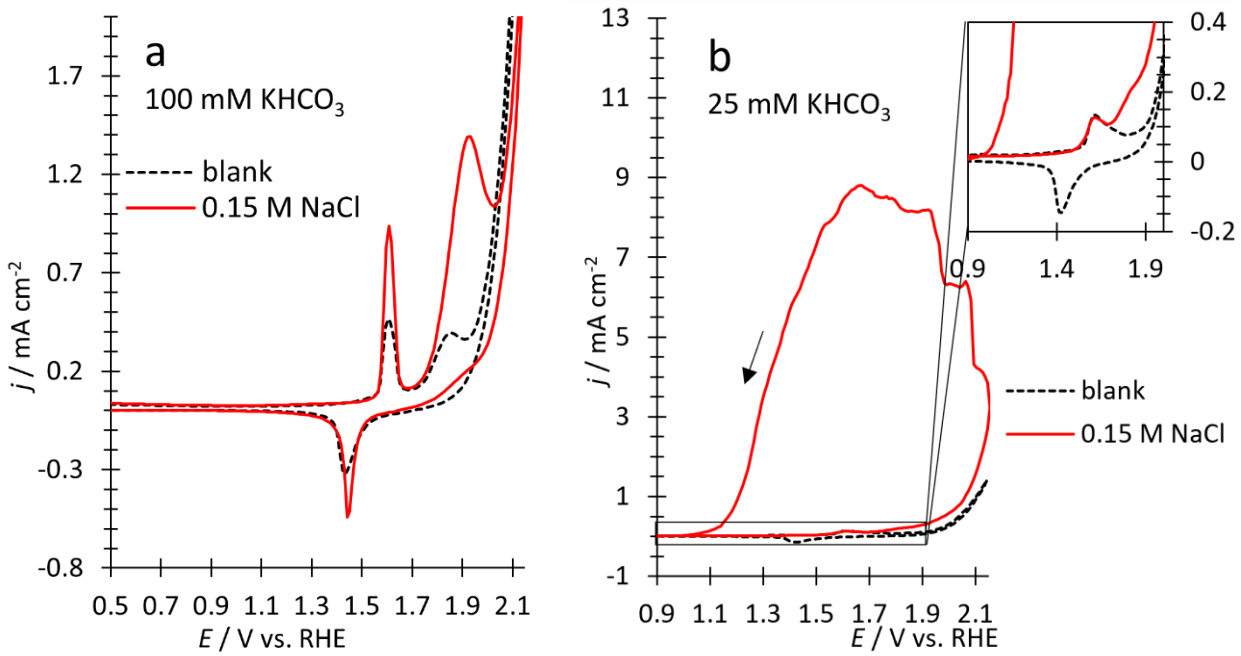

Figure 8.2 CVs performed on Ni disk in a) 100 mM $KHCO_3$ and b) 25 mM $KHCO_3$ with and without 0.15 M NaCl at v = 10 mV/s. Arrow indicates reverse scan corrosion current direction in (b).

When 0.15 M NaCl is added to the 25 mM $KHCO_3$, the electrode begins to corrode at the Ni^{3+} oxidation peak on the forward scan (Figure 8.2b, inset). The corrosion current (j_{corr}) continues to grow during the reverse scan and reaches a maximum of j_{corr} = 9 mA/cm^2. At potentials low enough, a *protection potential* (E_p) is reached, where the electrode potential and local pH no longer favor corrosion. The E_p observed in Figure 8.2b is 1.0 V vs. RHE. Corrosion is an electrochemically irreversible and unstable process—further scans produce more dramatic, unreproducible corrosion current, and electrochemical plating of Ni occurs only at potentials

lower than –0.257 V vs. SHE. Figure 8.2b reveals that 25 mM bicarbonate does not lead to $NiCO_3$ layer formation and as a result, 0.15 M NaCl induces corrosion.

A series of CVs were performed in 0.15 M NaCl with 0–100 mM $KHCO_3$ (Figure 8.3). The inset of Figure 8.3 reveals that mild corrosion begins on the reverse scan in 50 mM bicarbonate at 1.7 V vs. RHE and continues until E_p = 1.0 V vs. RHE. Although the corrosion for the 25 mM $KHCO_3$ achieves more sustained and increased j_{corr}, the protection potential is unchanged for 25 and 50 mM $KHCO_3$. Corrosion is the most severe without any bicarbonate to protect the Ni WE. The corrosion onset for 0 mM $KHCO_3$ is observed about 0.7 V vs. RHE on the forward scan and continues to increase on the reverse scan. To preserve the Ni disk WE, a slightly lower anodic potential was used for the 0 mM $KHCO_3$ CV. A maximum j_{corr} of 53 mA/cm^2 is achieved at 1.5 V vs. RHE and E_p = 0.6 V vs. RHE. The 0–50 mM $KHCO_3$ CVs in Figure 8.3 do not exhibit a Ni^{3+} reduction peak due to the current being largely dominated by corrosion in the reverse scan potential range. It can be concluded from Figure 8.3 that increased concentration of $KHCO_3$ from 0–50 mM result in lower j_{corr} and later corrosion onset, while concentration of 100 mM $KHCO_3$ prevents Ni corrosion altogether.

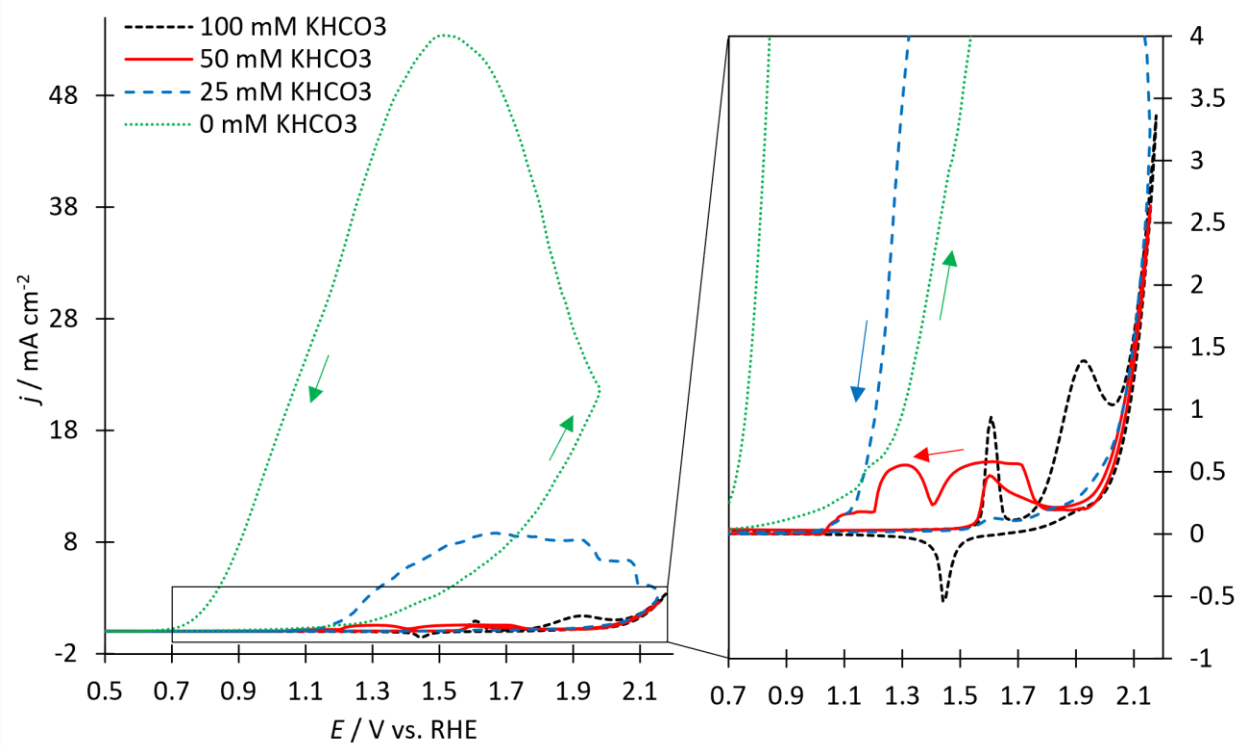

Figure 8.3 CVs performed on Ni disk with 0.15 M NaCl and 0–100 mM $KHCO_3$, performed at ν = 10 mV/s. The first CV is shown for 0, 25, and 50 mM $KHCO_3$. Colored arrows correspond to colored lines to differentiate forward and reverse scan current. The pH of each solution increased from 6.55 to 9.92 with increased $KHCO_3$ concentration and was used to calculate E vs. RHE.

The CVs represented in Figure 8.2 and Figure 8.3 were performed on Ni WEs that were polished immediately prior to use in the three-electrode cell, according to the standard protocol described in Chapter 3. Polishing the Ni WE disks removes the oxide layer on the electrode, which aids in electrode passivation according to the Ni Pourbaix diagram [118]. Therefore, to observe how the development of an oxide/carbonate layer on Ni affects chloride-induced corrosion, the CVs shown in Figure 8.4 and Figure 8.5 were not polished prior to experiments. The solution in both figures was 25 mM $KHCO_3$ and 0.15 M NaCl, used to mimic dialysate concentrations. The anodic potential limit was extended by 50 mV for each new scan in both Figure 8.4 and Figure

8.5. Figure 8.4 reveals that a gradual anodic increase from 1.6–1.96 V vs. RHE acts to reversibly develop the oxide/carbonate layer and passivate the electrode at potentials that otherwise favored corrosion at the same concentration (Figure 8.2b). The Ni^{2+} oxidation peak does not grow with increasing cycle number as observed in alkaline, chloride-free solution (Chapter 5); however, the carbonate layer becomes more developed with cycling as the Ni^{3+} reduction peak concurrently grows. It is therefore concluded that the slow, reversible mixed oxide/carbonate layer development allows Ni to achieve potentials of 1.96 V vs. RHE without corrosion. When compared to Figure 8.2b, it is evident that Ni is more vulnerable to corrosion when polished and exposed to potentials above 1.7 V vs. RHE without a protective layer. The oxide/carbonate layer developed in Figure 8.4 provides about 200 mV of corrosion protection compared to a polished electrode in the same conditions (Figure 8.2b).

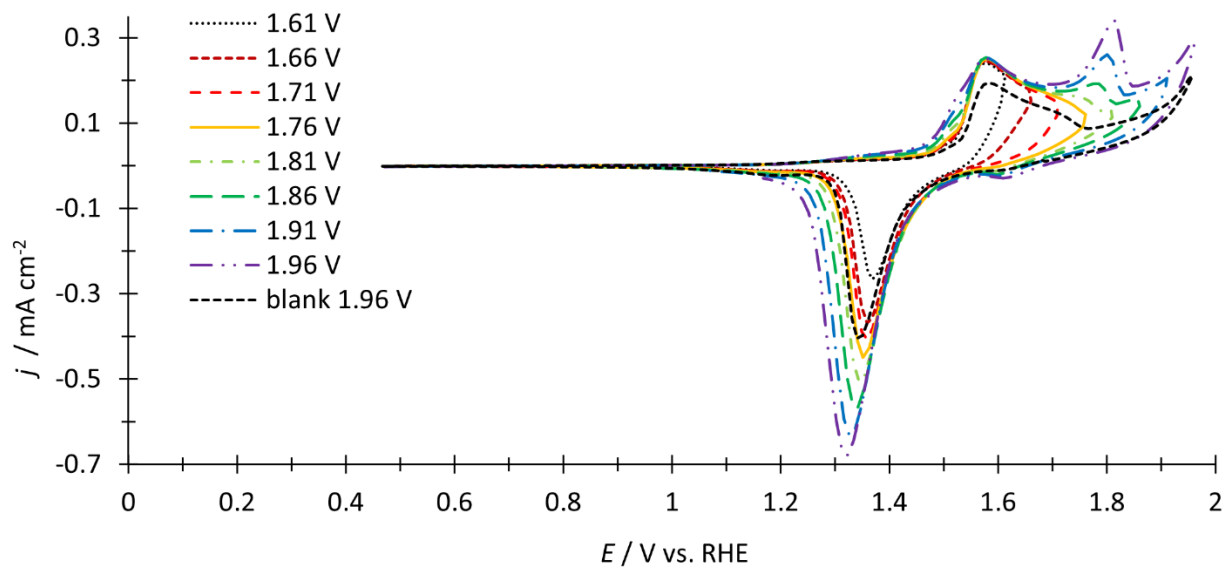

Figure 8.4 CVs performed on Ni in 0.15 M NaCl and 25 mM $KHCO_3$ with the anodic limit increased by 50 mV for each new CV; performed at v = 10 mV/s. The blank does not contain NaCl. Solution pH was 9.63 and was used to calculate E vs. RHE.

The same type of anodic limit increase experiment was performed with the inclusion of a potential hold at –0.23 V vs. RHE for 60 s prior to each scan. This reducing potential is low enough to electrochemically reduce the surface oxide/carbonate layers without plating Ni onto the electrode from Ni^{2+} ions that may be in solution from corrosion in previous scans. The results in Figure 8.5 show Ni corrosion beginning on the reverse scan of the 1.76 V vs. RHE CV with an E_p of 1.0 V vs. RHE, consistent with previous findings in bicarbonate solution. The following 1.81 V vs. RHE CV shows corrosion current even at the beginning of the Ni^{2+} oxidation peak on the forward scan. This is in general agreement with pitting corrosion, which affects a localized electrode region and grows more severe as the pit grows irreversibly in a corrosive environment [119]. The onset of corrosion in the 1.76 V vs. RHE CV made the electrode more vulnerable to pitting corrosion at earlier potentials in the following 1.81 V vs. RHE CV. A maximum j_{corr} is observe at 3 mA/cm^2. The maximum corrosion current is less than half of the 8 mA/cm^2 observed in Figure 8.2b. The difference is likely due to a combination of a) lower anodic limit, b) partial passive layer reduction during 60 s hold, and c) erratic corrosion phenomenon. The results from Figure 8.3 and Figure 8.5 show that both physical and electrochemical removal of the oxide layer makes Ni more susceptible to corrosion, while Figure 8.4 demonstrates that oxide/carbonate layer growth can increase the corrosion-free potential window.

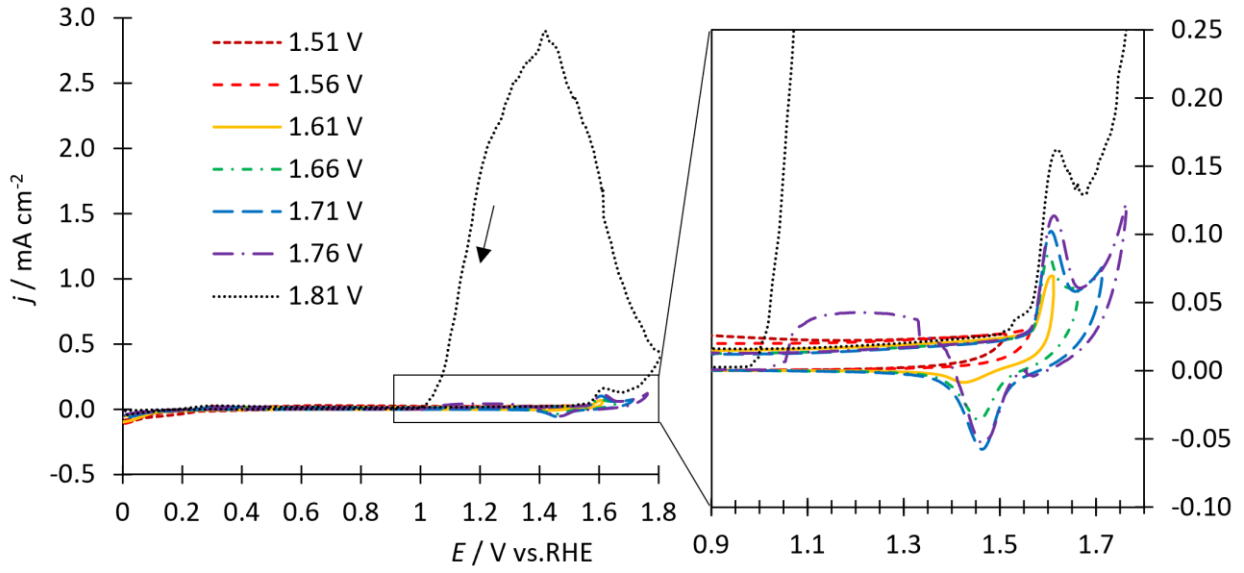

Figure 8.5 CVs performed on Ni in 0.15 M NaCl and 25 mM $KHCO_3$ with the anodic limit increased by 50 mM for each new CV. Between each CV the electrode potential was held at –0.23 V vs. RHE for 60 s to reduce surface oxide/carbonate layer. All scans performed at ν = 10 mV/s. Arrow indicates the direction of j_{corr} in the 1.8 V vs. RHE reverse scan. Solution pH was 9.62 and was used to calculate E vs. RHE.

The three-electrode cell experiments discussed in this section address Ni corrosion in chloride solutions within approximate URC operating conditions. The presence of 100 mM $KHCO_3$ provides Ni corrosion protection due to reversible carbonate/oxide layer passivation. This finding agrees with the higher performance and stability of the URC when using a 0.1 M $KHCO_3$ electrolyte. A lower, physiologically relevant bicarbonate concentration of 25 mM is less protective, though can avoid corrosion up to 1.96 V vs. RHE if the oxide/carbonate layer is allowed to gradually develop in the presence of Cl^-. The $Ni(OH)_2$ catalyst of NHF is more resistant to corrosion as a passivating oxide species. The Ni foam substrate, however, is more susceptible to corrosion in neutralized anolyte conditions. The next section examines the effect of chloride within the URC.

8.2 NICKEL CORROSION IN URC

8.2.1 *Chloride-Induced Corrosion*

The URC was operated under pH and temperature control while NaCl was "spiked" into the anolyte feed (Figure 8.6). Each NaCl dose was provided from a saturated NaCl solution. Table 8.1 lists each NaCl addition time, the equivalent concentration percentage relative to a physiologic concentration of 0.137 M Cl^-, and the cumulative Cl^- % for the experiment. The current was monitored for chloride-induced corrosion to understand what range of chloride concentration is acceptable for use within the URC before corrosion occurs. Figure 8.6a shows URC operation in 100 mM $KHCO_3$ and Figure 8.6b shows operation with 25 mM $KHCO_3$. Cell temperature and pH are also included to account for URC current sensitivity to those parameters.

In Figure 8.6a, the URC experienced a tubing failure at 1.5 hr which took about one hour to fix, so cell temperature and current density are omitted during that time. The cell temperature took until about 4.25 hr to stabilize again. Due to the tubing mishap, the third NaCl addition occurred about two hours after the second. Figure 8.6a shows stable URC current (when accounting for the temperature fluctuations due to tubing issue) through the first 1.75% Cl^- addition at 4.48 hr (Table 8.1). After 4.48 hr, the current density climbs without an associated increase in cell temperature or pH. Therefore, the increase in current density from 4.5–6 hr is due to chloride-induced corrosion. The strength of Cl^- additions after 4.73 hr increased, which contributed to more severe corrosion during this time. Nickel measurements were not performed directly, however by the end of the experiment the anolyte solution was a faint green color, a definitive sign of Ni corrosion. This experiment, while more qualitative than quantitative,

demonstrates that the URC cannot operate with chloride at physiological concentrations, even in the presence of 100 mM $KHCO_3$. This conflicts with three-electrode experiments discussed in the previous section, likely due to the pH control enforcing a neutral environment rather than the natural 8–10 pH of 25–100 mM $KHCO_3$ that occurs when the bicarbonate solution is exposed to atmospheric CO_2.

Experiment	***t* (hr)**	**% of 0.137 M**	**Cumulative Cl^-**
Figure 8.6a	1.0	0.25	0.25%
Figure 8.6a	1.25	0.25	0.50%
Figure 8.6a	3.48	0.25	0.75%
Figure 8.6a	3.73	0.25	1.00%
Figure 8.6a	3.98	0.25	1.25%
Figure 8.6a	4.23	0.25	1.50%
Figure 8.6a	4.48	0.25	1.75%
Figure 8.6a	4.73	0.25	2.00%
Figure 8.6a	4.98	0.5	2.50%
Figure 8.6a	5.23	0.5	3.00%
Figure 8.6a	5.6	1.0	4.00%
Figure 8.6b	4.18	0.5	0.5%
Figure 8.6b	5.13	0.5	1.0%
Figure 8.6b	5.57	0.5	1.5%

Table 8.1 Table listing chloride additions during URC operation in 100 and 25 mM $KHCO_3$.

In the 25 mM $KHCO_3$ experiment (Figure 8.6b), the first Cl^- addition was not added until the cell temperature stabilized, at 4.18 hr. Even at this low 0.5% total chloride addition, the cell current was observed to increase without an associated increase in cell temperature or pH. Furthermore, at 5.13 hr, when cumulative Cl^- concentration was 1% of physiological, the current increases while a decrease in cell temperature occurs. It can therefore be concluded that in 25 mM $KHCO_3$ anolyte, the URC can not operate without corrosion at 1% of physiological Cl^-

concentration. As expected with lower bicarbonate concentration, this is less than the 1.75% Cl^- limit observed in the 100 mM $KHCO_3$ experiment.

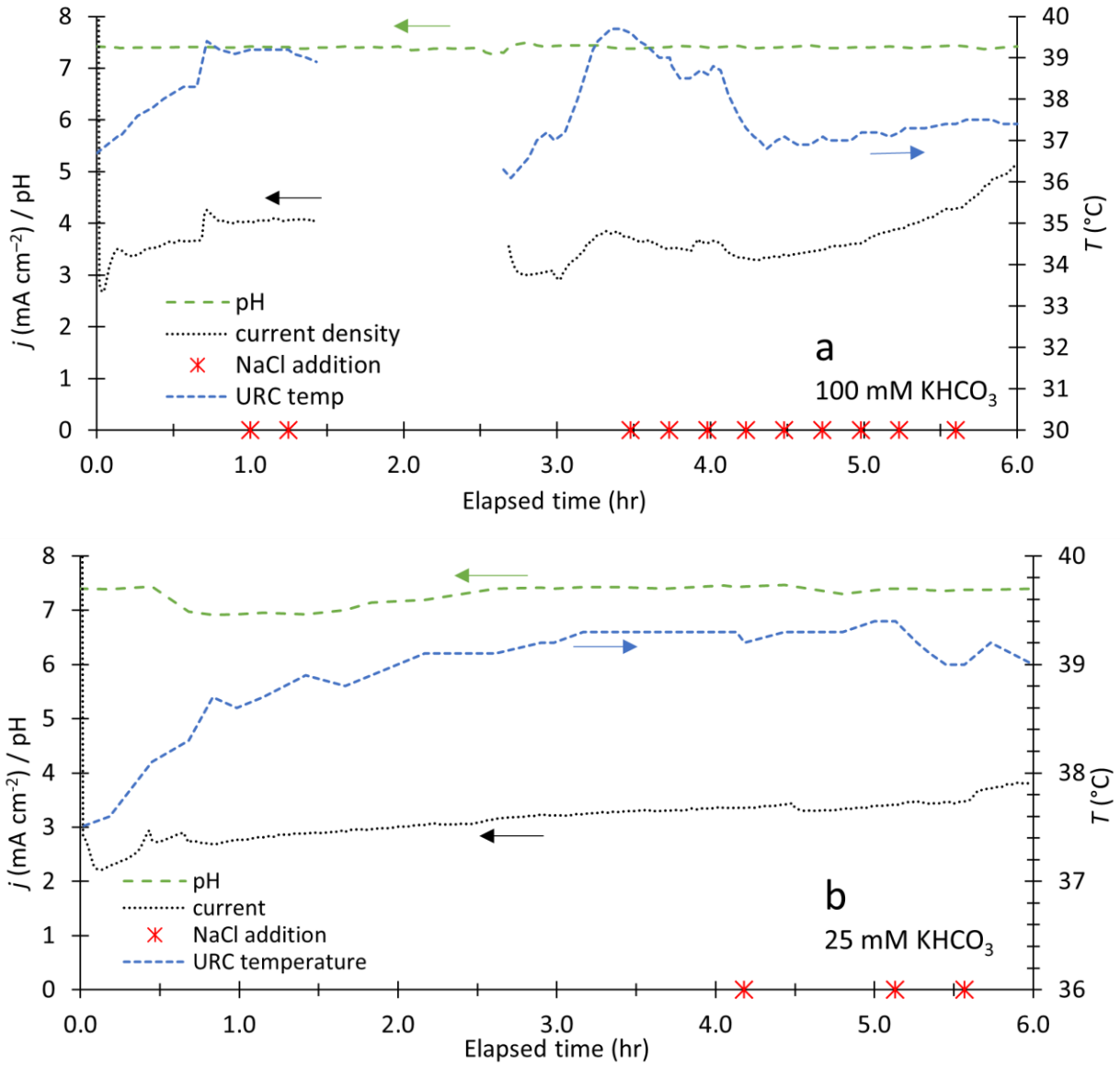

Figure 8.6 URC operating under current and pH control with 10 mM urea in a) 100 mM $KHCO_3$ and b) 25 mM $KHCO_3$, operated at 1.9 V. Chloride additions marked with red asterisks with amount listed in Table 8.1. Temperature and current data from 1.5–2.6 hr in (a) omitted for clarity due to rapid fluctuations from tubing failure; chloride was not added during this time.

8.2.2 *Nickel Dissolution*

Nickel concentrations were measured directly using inductively coupled plasma optical emission spectroscopy (ICP-OES) while the URC was not operating. The solution was recirculated at a high flowrate of 50 ml/min with different anodes in the URC to understand if Ni dissolution (E^0 = –0.4 V vs. SHE) occurs even without applied potential or chloride. Dissolution refers to the process of Ni corrosion to produce Ni^{2+} in the absence of a chemical reaction product, for example $NiCl_2$. The four anodes tested included Ni foam, used NHF, unused NHF, and unused NHF subjected to a 2-hour sonication bath cleaning during which the bath water was replaced at 1 hour. Measurements were taken in triplicates and averaged at 0, 1, and 2 hours to record the amount of Ni dissolution over time. Figure 8.7 reveals that Ni dissolution does occur in DI water without an applied potential—at surprisingly high rates. A new NHF electrode without sonication cleaning produces the highest amount of Ni, 0.486 mg in 2 hours. After a two-hour sonication cleaning, a new NHF electrode produces 0.175 mg in 2 hours, a reduction of 64% from the untreated new NHF. The lowest Ni producing electrodes are the used NHF and Ni foam which produce 0.078 and 0.060 mg in 2 hours, respectively. The adult human toxicity limit for Ni is 4.3 µg/kg bodyweight/day [125]; therefore, for an average 70 kg adult, the minimum (Ni foam) dissolution rate requires only 10 hours to achieve the toxic limit. While this toxic limit is assumed to be a direct ingestion of Ni, prolonged blood exposure to Ni ions is generally unacceptable for a medical device. Based on the nearly indistinguishable dissolution rate of the used NHF and the Ni foam, it appears that the large majority of Ni originates from the foam substrate rather than

the $Ni(OH)_2$ catalyst. As such, replacing the Ni foam substrate with that of a more corrosion resistant alloy may prevent Ni dissolution.

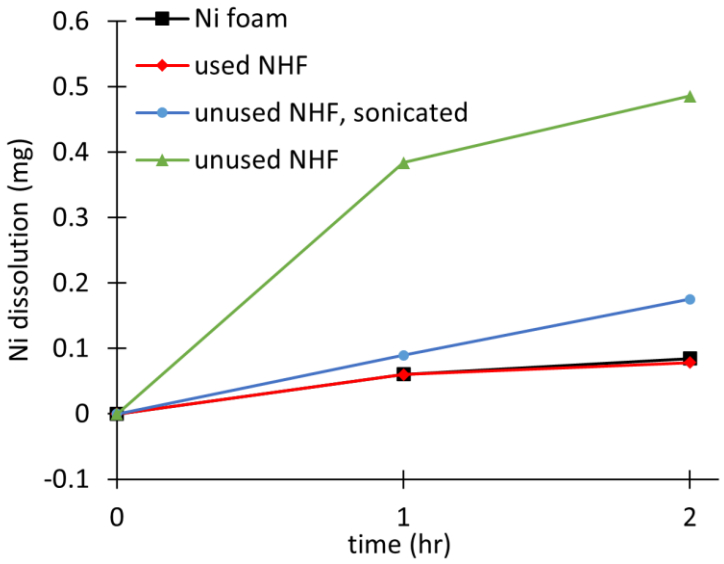

Figure 8.7 Direct Ni ICP measurements performed on 200 ml of DI water circulating in URC at 50 ml/min with different anodes and no applied voltage.

The data presented in this final chapter are concerning for the advancement of a medical device using the as-developed NHF anode. In summary, to avoid Ni corrosion in the URC, more than 99% of the Cl^- ions must be removed from dialysate prior to reaction in the URC *and* the Ni foam substrate must be replaced by a corrosion-resistant, electrically conductive material. Although Ni is the underlying component in the most active UOR electrocatalysts, its tendency to corrode in neutral and chloride containing environments means that unmodified Ni cannot be used as a catalyst support in a portable dialysis device. Further studies should be performed to identify alternative formulation of catalyst supports that are less susceptible to corrosion.

Chapter 9. CONCLUSIONS, CHALLENGES, AND FUTURE WORK

The research discussed in this document advances the understanding of urea electrooxidation for the application of regenerative dialysis. Electrooxidation of urea was independently explored on both Pt and Ni in a well-controlled, three-electrode cell to gain insights into the UOR reaction mechanisms, kinetic parameters, and deactivation modes on each electrocatalyst. Based on the catalytic studies, a bench-scale URC was designed and optimized to achieve sufficient urea clearance for a portable dialysis device. The URC demonstrated the ability to remove urea from a solution maintained at physiologic urea concentration, temperature, and pH. It was also established that physiologic pH and chloride concentrations create an environment where corrosion of the electrocatalyst is favorable, which is problematic for both patient health and reactor durability. Chloride-induce corrosion and dissolution must be addressed for the future progress of a portable dialysis device. The research is summarized below and concludes with future research ideas.

Initial UOR studies were performed on Pt in an alkaline environment to mimic that of an alkaline AEM. The maximum UOR rate on Pt is 0.03 mA/cm^2, which occurs at 1.17 V vs. RHE in 0.1 M KOH. This corresponds to a specific urea reaction rate of 3.1×10^{-9} g/s·cm^2 and would require a sizeable electrode area of 5.6×10^{4} cm^2 to remove 15 grams/day. Furthermore, it was

shown that the oxidation of Pt competes with UOR and poisions the catalytic surface in the urea oxidation potential regime, above 0.9 V vs. RHE. Platinum oxide posioning is an electrochemically reversible process, and the surface can be regenerated by exposing the electrode to a potential below 0 V vs. RHE for 60 s. When Pt was incorportated into a NiO anode in early URC development, Pt poisioning contributed to a 20% reduction in oxidation current throughout a 4-hour experiment. Additionally, Pt is a well-known OER catalyst that was observed to favor OER at URC potentials above 1.8 V, therby limiting UOR.

Urea oxidation on a Ni catalyst was demonstrated to have much faster kinetics than on Pt, though with a 0.4 V increase in overpotential. The significant overpotential for UOR on Ni is due to the requirement of Ni^{3+} reaction sites, which is favorable at potentials greater than 1.26 V vs. RHE in 0.1 M KOH. When these potentials are achieved on Ni, UOR kinetics are hundreds of times faster as compared to Pt, which contributes to a mass transport limitation at physiologic urea concentrations in 0.1 M KOH. Furthermore, UOR was shown to have a low reaction order of 0.39 with respect to urea, yet exhibits significant enhancement with increased temperature and pH. The use of NHF further enhances the UOR rate by virtue of improved kinetics, higher ECSA, and reduced mass transport limitation. In addition to urea oxidation, the 1% Fe-doped $Ni(OH)_2$ catalysts showed a unique ability to perform urea and creatinine co-oxidation at short time scales in physiologic solute concentrations in 1 M KOH. The high-performing Ni-based catalysts motivated the development of Ni-based URC anodes.

The URC was designed to utilize an AEM to provide an alkaline environment without the need for and alkaline anolyte. The highest performing URC consisted of a NHF anode and a Pt/C

cathode supported on carbon cloth. In a controlled environment of 0.1 M $KHCO_3$, pH of 7.4, and temperature of 37 °C, the URC exhibited stable and reproducible urea removal rates throughout 6-hour experiments. Anolyte flowrates in the 20–40 ml/min range led to urea removal rates of about 35 mg/day/cm^2, reasonable for a portable device with an active area of 400 cm^2. The minimum flowrate constraint of 3 ml/min generates a urea removal rate of only 15 mg/day cm^2, which is not sufficient for a portable dialysis device. The improved urea removal at moderate/high flowrates is hypothesized to be an effect of boundary layer disruption at the anode. The mass transport limit measured on Ni during three-electrode cell experiments indicates that the URC operation conditions are also mass transport limited. Therefore, a moderate flow rate against a highly porous NHF anode could minimize the diffusion layer thickness and explain the observed increased urea degradation rates. Flowrates above 20 ml/min per cell produce diminishing reaction rate returns as the diffusion layer becomes insignificant. Furthermore, the faradic efficiency of UOR decreases with higher flow rates.

Some initial chloride corrosion experiments were performed both in the three-electrode cell and in the URC. Although mild surface passivation can be achieved through a well-developed oxide/carbonate layer on Ni, chloride-induced pitting corrosion and Ni dissolution are problematic at the URC operating conditions. The neutral pH, elevated temperature, and applied cell voltage create an environment within the URC where corrosion is observed at concentrations of under 1 mol% Cl^- compared to physiologic 0.137 M Cl^-. Furthermore, the Ni foam substrate of NHF appears to be a source of dissolution in the absence of an applied cell potential. Therefore, immediate future research must address the Ni corrosion issue.

The Ni dissolution rates measured in Chapter 8 indicate that Ni foam corrosion in neutral, non-chloride containing solution produces about 0.55 mA/cm^2 of corrosion current. This Ni dissolution rate requires only about 10 hours to achieve average human bodyweight Ni toxicity accumulation. Incorporation of a downstream, activated carbon filter can prevent Ni entrance into the dialyzer, but will not improve electrode degradation. Nickel chelating agents are physiologically safe for ingestion, yet indiscriminately bind other electrolytes in the dialysate. Therefore, a corrosion-resistant, electrically conductive, porous catalyst support is of primary interest. According to the current URC design, the high alkalinity of the anode/membrane interface creates a region of corrosion protection. However, the decreasing pH gradient with increased distances from the AEM is where the anode is more susceptible to corrosion. Due to lack of contact with the ionomer, this region does not benefit from having a catalytic surface and therefore replacing the Ni foam with a corrosion-resistant alloy is desirable.

The design of the URC represents the first of its kind Ni-based electrochemical urea reactor for the application of portable dialysis. Although Ni corrosion poses a challenge for future medical applications, the membrane-based device design and operation remain useful for a noncorrosive anode. Furthermore, the underlying urea oxidation research on Ni and Pt is directly applicable to agricultural, industrial, and municipal waste stream remediation with less stringent size, pH, temperature, and concentration requirements. As discussed in Chapter 2, urea is concentrated in industrial and agricultural waste streams. When fed to the environment untreated, urea-rich waste causes eutrophication which triggers a chain of destructive local

ecosystem responses including agal blooms, dead zones, acidification, and fish kills. Plus, the bacterial transformation of urea into N_2O and NO_x contribute to global catastrophic environmental destruction including smog, acid rain and climate change. The urea reactor and underlying urea oxidation research discussed in this manuscript are directly applicable to wastewater treatment, including but not limited to dialysate regeneration.

REFERENCES

1. Gura V, Rivara MB, Bieber S, Munshi R, Smith NC, Linke L, Kundzins J, Beizai M, Ezon C, Kessler L, Himmelfarb J (2016) A wearable artificial kidney for patients with end-stage renal disease. JCI Insight 1: . https://doi.org/10.1172/jci.insight.86397

2. (2020) 2019 Annual Data Report. United States Renal Data System

3. Kooman JP, Joles JA, Gerritsen KG (2015) Creating a wearable artificial kidney: where are we now? Expert Rev Med Devices 12:373–376 . https://doi.org/10.1586/17434440.2015.1053466

4. Pauly RP (2013) Survival comparison between intensive hemodialysis and transplantation in the context of the existing literature surrounding nocturnal and short-daily hemodialysis. Nephrol Dial Transplant 28:44–47 . https://doi.org/10.1093/ndt/gfs419

5. Stephens RL, Jacobsen SC, Atkin-thor E, Kolff W (1976) Portable/wearable artificial kidney (WAK) - initial evaluation. Proc Eur Dial Transpl Assoc Eur Dial Transpl Assoc 12:511–518

6. Murisasco A, Baz M, Boobes Y, Bertocchio P, el Mehdi M, Durand C, Reynier JP, Ragon A (1986) A continuous hemofiltration system using sorbents for hemofiltrate regeneration. Clin Nephrol 26 Suppl 1:S53-57

7. Davenport A, Gura V, Ronco C, Beizai M, Ezon C, Rambod E (2007) A wearable haemodialysis device for patients with end-stage renal failure: a pilot study. Lancet Lond Engl 370:2005–2010 . https://doi.org/10.1016/S0140-6736(07)61864-9

8. Smakman R, van Doorn AW (1986) Urea removal by means of direct binding. Clin Nephrol 26 Suppl 1:S58-62

9. Cheah WK, Sim Y-L, Yeoh F-Y (2016) Amine-functionalized mesoporous silica for urea adsorption. Mater Chem Phys 175: . https://doi.org/10.1016/j.matchemphys.2016.03.007

10. Wester M, Simonis F, Lachkar N, Wodzig WK, Meuwissen FJ, Kooman JP, Boer WH, Joles JA, Gerritsen KG (2014) Removal of urea in a wearable dialysis device: a reappraisal of electro-oxidation. Artif Organs 38:998–1006 . https://doi.org/10.1111/aor.12309

11. Urbańczyk E, Sowa M, Simka W (2016) Urea removal from aqueous solutions—a review. J Appl Electrochem 46: . https://doi.org/10.1007/s10800-016-0993-6

12. Keller RW, Yao SJ, Brown JM, Wolfson SK, Zeller MV (1980) Electrochemical removal of urea from physiological buffer as the basis for a regenerative dialysis system. J Electroanal Chem Interfacial Electrochem 116:469–485 . https://doi.org/10.1016/S0022-0728(80)80271-3

13. Yao SJ, Wolfson SK, Tokarsky JM, Ahn BK (1974) De-ureation by electrochemical oxidation. Bioelectrochem Bioenerg 1:180–186 . https://doi.org/10.1016/0302-4598(74)85019-1

14. Dbira S, Bensalah N, Ahmad MI, Bedoui A (2019) Electrochemical Oxidation/Disinfection of Urine Wastewaters with Different Anode Materials. Materials 12: . https://doi.org/10.3390/ma12081254

15. Boggs BK, King RL, Botte GG (2009) Urea electrolysis: direct hydrogen production from urine. Chem Commun 0:4859–4861 . https://doi.org/10.1039/B905974A

16. Sayed ET, Eisa T, Mohamed HO, Abdelkareem MA, Allagui A, Alawadhi H, Chae K-J (2019) Direct urea fuel cells: Challenges and opportunities. J Power Sources 417:159–175 . https://doi.org/10.1016/j.jpowsour.2018.12.024

17. Kumar GG, Farithkhan A, Manthiram A (2020) Direct Urea Fuel Cells: Recent Progress and Critical Challenges of Urea Oxidation Electrocatalysis. Adv Energy Sustain Res 1:2000015 . https://doi.org/10.1002/aesr.202000015

18. Liu D, Liu T, Zhang L, Qu F, Du G, Asiri AM, Sun X (2017) High-performance urea electrolysis towards less energy-intensive electrochemical hydrogen production using a bifunctional catalyst electrode. J Mater Chem A 5:3208–3213 . https://doi.org/10.1039/C6TA11127K

19. (1977) Electrolytic pretreatment of urine

20. Putnam DF (1971) Composition and concentrative properties of human urine

21. O.J. Murphy, Hitchens GD, Kaba L Selective Removal of Organics for Water Reclamation. https://ntrs.nasa.gov/citations/19900014481. Accessed 14 Jan 2021

22. Yao SJ, Wolfson SK, Ahn BK, Liu CC (1973) Anodic Oxidation of Urea and an Electrochemical Approach to De-ureation. Nature 241:471–472 . https://doi.org/10.1038/241471a0

23. Fels M (1978) Recycle of dialysate from the artificial kidney by electrochemical degradation of waste metabolites: small-scale laboratory investigations. Med Biol Eng Comput 16:25–30

24. Fels M (1982) Recycle of dialysate from the artificial kidney by electrochemical degradation of waste metabolites: Continuous reactor investigations. Med Biol Eng Comput 20:257–263 . https://doi.org/10.1007/BF02442789

25. Hall DS, Lockwood DJ, Bock C, MacDougall BR (2015) Nickel hydroxides and related materials: a review of their structures, synthesis and properties. Proc Math Phys Eng Sci R Soc 471: . https://doi.org/10.1098/rspa.2014.0792

26. Yao SJ, Wolfson SK, Krupper MA, Wu KJ (1984) Controlled-potential controlled-current electrolysis: In vitro and in vivo electrolysis of urea. Bioelectrochem Bioenerg 13:15–24 . https://doi.org/10.1016/0302-4598(84)85111-9

27. Patzer JF, Wolfson SK, Yao SJ (1990) Reactor control and reaction kinetics for electrochemical urea oxidation. Chem Eng Sci 45:2777–2784 . https://doi.org/10.1016/0009-2509(90)80170-J

28. Skundin AM (1994) Anodic-oxidation of urea in neutral solutions. Russ J Electrochem 1145–1147

29. Bolzan AE, Iwasita T (1988) Determination of the volatile products during urea oxidation on platinum by on line mass spectroscopy. Electrochimica Acta 33:109–112 . https://doi.org/10.1016/0013-4686(88)80040-9

30. Simka W, Piotrowski J, Nawrat G (2007) Influence of anode material on electrochemical decomposition of urea. Electrochimica Acta 52:5696–5703 . https://doi.org/10.1016/j.electacta.2006.12.017

31. Cataldo Hernández M, Russo N, Panizza M, Spinelli P, Fino D (2014) Electrochemical oxidation of urea in aqueous solutions using a boron-doped thin-film diamond electrode. Diam Relat Mater 44:109–116 . https://doi.org/10.1016/j.diamond.2014.02.006

32. Li H, Yu Q, Yang B, Li Z, Lei L (2015) Electro-catalytic oxidation of artificial human urine by using BDD and IrO2 electrodes. J Electroanal Chem 738:14–19 . https://doi.org/10.1016/j.jelechem.2014.11.018

33. Cho K, Hoffmann MR (2014) Urea Degradation by Electrochemically Generated Reactive Chlorine Species: Products and Reaction Pathways. Environ Sci Technol 48:11504–11511 . https://doi.org/10.1021/es5025405

34. Amstutz V, Katsaounis A, Kapalka A, Comninellis C, Udert KM (2012) Effects of carbonate on the electrolytic removal of ammonia and urea from urine with thermally prepared IrO<Subscript>2</Subscript> electrodes. J Appl Electrochem 42:787–795 . https://doi.org/10.1007/s10800-012-0444-y

35. A. Viktorov V, N. Varin A, M. Grinval'd V, P. Maksimov E, N. Fomicheva N, K. Zavalishin Y, M. Leshchinskii G, I. Razhev I, G. Noskov S, Sh. Shadiev B, V. Rodin V, I. Strelkov S, V. Shukov O, D. Turyaev A, V. Shishkin S (2003) Current State and Prospects for Development of Domestic Equipment for Hemodialysis with Dialyzate Regeneration. Biomed Eng 37:16–21 . https://doi.org/10.1023/A:1023777427647

36. V.M G, A.A Y, G.M L (2002) Design Principles of an Electrochemical Dialyzate Regenerator for an Artificial Kidney Apparatus. Biomed Eng 36:199–206 . https://doi.org/10.1023/A:1021179918359

37. Grinval'd VM, Leshchinskii GM, Rodin VV, Strelkov SI, Yakovleva AA (2003) Development and Testing of a Unit for Electrochemical Oxidation of Products of Hemodialysis. Biomed Eng 2:67–72 . https://doi.org/10.1023/A:1024727513884

38. Maksimov EP, Leshchinskii GM, Grinval'd VM, Fomicheva NN, Shadiev BS (2003) Correction of Dialyzate Composition during Electrochemical Regeneration. Biomed Eng 37:73–76 . https://doi.org/10.1023/A:1024779530723

39. Wester M, van Gelder MK, Joles JA, Simonis F, Hazenbrink DHM, van Berkel TWM, Vaessen KRD, Boer WH, Verhaar MC, Gerritsen KGF (2018) Removal of urea by electro-oxidation in a miniature dialysis

device: a study in awake goats. Am J Physiol-Ren Physiol 315:F1385–F1397 . https://doi.org/10.1152/ajprenal.00094.2018

40. Colmenares LC, Wurth A, Jusys Z, Behm RJ (2009) Model study on the stability of carbon support materials under polymer electrolyte fuel cell cathode operation conditions. J Power Sources 190:14–24 . https://doi.org/10.1016/j.jpowsour.2009.01.078

41. Wickman B, Grönbeck H, Hanarp P, Kasemo B (2010) Corrosion Induced Degradation of Pt/C Model Electrodes Measured with Electrochemical Quartz Crystal Microbalance. J Electrochem Soc 157:B592 . https://doi.org/10.1149/1.3309730

42. Vidotti M, Silva MR, Salvador RP, Torresi SIC de, Dall'Antonia LH (2008) Electrocatalytic oxidation of urea by nanostructured nickel/cobalt hydroxide electrodes. Electrochimica Acta 53:4030–4034 . https://doi.org/10.1016/j.electacta.2007.11.029

43. Ding R, Qi L, Jia M, Wang H (2014) Facile synthesis of mesoporous spinel NiCo2O4 nanostructures as highly efficient electrocatalysts for urea electro-oxidation. Nanoscale 6:1369–1376 . https://doi.org/10.1039/C3NR05359H

44. Wang L, Li M, Huang Z, Li Y, Qi S, Yi C, Yang B (2014) Ni–WC/C nanocluster catalysts for urea electrooxidation. J Power Sources 264:282–289 . https://doi.org/10.1016/j.jpowsour.2014.04.104

45. Wu M-S, Lin G-W, Yang R-S (2014) Hydrothermal growth of vertically-aligned ordered mesoporous nickel oxide nanosheets on three-dimensional nickel framework for electrocatalytic oxidation of urea in alkaline medium. J Power Sources 272:711–718 . https://doi.org/10.1016/j.jpowsour.2014.09.009

46. Guo F, Ye K, Cheng K, Wang G, Cao D (2015) Preparation of nickel nanowire arrays electrode for urea electro-oxidation in alkaline medium. J Power Sources 278:562–568 . https://doi.org/10.1016/j.jpowsour.2014.12.125

47. Wang L, Du T, Cheng J, Xie X, Yang B, Li M (2015) Enhanced activity of urea electrooxidation on nickel catalysts supported on tungsten carbides/carbon nanotubes. J Power Sources 280:550–554 . https://doi.org/10.1016/j.jpowsour.2015.01.141

48. Ye K, Zhang D, Guo F, Cheng K, Wang G, Cao D (2015) Highly porous nickel@carbon sponge as a novel type of three-dimensional anode with low cost for high catalytic performance of urea electro-oxidation in alkaline medium. J Power Sources 283:408–415 . https://doi.org/10.1016/j.jpowsour.2015.02.149

49. Guo F, Ye K, Du M, Huang X, Cheng K, Wang G, Cao D (2016) Electrochemical impedance analysis of urea electro-oxidation mechanism on nickel catalyst in alkaline medium. Electrochimica Acta 210:474–482 . https://doi.org/10.1016/j.electacta.2016.05.149

50. Glibert P, Harrison J, Heil C, Seitzinger S (2006) Escalating Worldwide use of Urea – A Global Change Contributing to Coastal Eutrophication. Biogeochemistry 77:441–463 . https://doi.org/10.1007/s10533-005-3070-5

51. Donald DB, Bogard MJ, Finlay K, Leavitt PR (2011) Comparative effects of urea, ammonium, and nitrate on phytoplankton abundance, community composition, and toxicity in hypereutrophic freshwaters. Limnol Oceanogr 56:2161–2175 . https://doi.org/10.4319/lo.2011.56.6.2161

52. Zambelli B, Musiani F, Benini S, Ciurli S (2011) Chemistry of Ni2+ in Urease: Sensing, Trafficking, and Catalysis. Acc Chem Res 44:520–530 . https://doi.org/10.1021/ar200041k

53. Pan B, Lam SK, Mosier A, Luo Y, Chen D (2016) Ammonia volatilization from synthetic fertilizers and its mitigation strategies: A global synthesis. Agric Ecosyst Environ 232:283–289 . https://doi.org/10.1016/j.agee.2016.08.019

54. AR5 Climate Change 2013: The Physical Science Basis — IPCC. https://www.ipcc.ch/report/ar5/wg1/. Accessed 16 Feb 2021

55. Prosser JI, Hink L, Gubry-Rangin C, Nicol GW (2020) Nitrous oxide production by ammonia oxidizers: Physiological diversity, niche differentiation and potential mitigation strategies. Glob Change Biol 26:103–118 . https://doi.org/10.1111/gcb.14877

56. Yi Q, Huang W, Zhang J, Liu X, Li L (2007) A novel titanium-supported nickel electrocatalyst for cyclohexanol oxidation in alkaline solutions. J Electroanal Chem 610:163–170 . https://doi.org/10.1016/j.jelechem.2007.07.009

57. Vaze AS, Sawant SB, Pangarkar VG (1997) Electrochemical oxidation of isobutanol to isobutyric acid at nickel oxide electrode: improvement of the anode stability. J Appl Electrochem 27:584–588 . https://doi.org/10.1023/A:1018406914144

58. Schäfer H-J (1987) Oxidation of organic compounds at the nickel hydroxide electrode. In: Electrochemistry I. Springer, Berlin, Heidelberg, pp 101–129

59. King RL, Botte GG (2011) Hydrogen production via urea electrolysis using a gel electrolyte. J Power Sources 196:2773–2778 . https://doi.org/10.1016/j.jpowsour.2010.11.006

60. Hall DS, Bock C, MacDougall BR (2013) The Electrochemistry of Metallic Nickel: Oxides, Hydroxides, Hydrides and Alkaline Hydrogen Evolution. J Electrochem Soc 160:F235 . https://doi.org/10.1149/2.026303jes

61. Vedharathinam V, Botte GG (2012) Understanding the electro-catalytic oxidation mechanism of urea on nickel electrodes in alkaline medium. Electrochimica Acta 81:292–300 . https://doi.org/10.1016/j.electacta.2012.07.007

62. Vedharathinam V, Botte GG (2013) Direct evidence of the mechanism for the electro-oxidation of urea on Ni(OH)2 catalyst in alkaline medium. Electrochimica Acta 108:660–665 . https://doi.org/10.1016/j.electacta.2013.06.137

63. Vedharathinam V, Botte GG (2014) Experimental Investigation of Potential Oscillations during the Electrocatalytic Oxidation of Urea on Ni Catalyst in Alkaline Medium. J Phys Chem C 118:21806–21812 . https://doi.org/10.1021/jp5052529

64. Wang D, Botte GG (2014) In Situ X-Ray Diffraction Study of Urea Electrolysis on Nickel Catalysts. ECS Electrochem Lett 3:H29–H32 . https://doi.org/10.1149/2.0031409eel

65. King RL, Botte GG (2011) Investigation of multi-metal catalysts for stable hydrogen production via urea electrolysis. J Power Sources 196:9579–9584 . https://doi.org/10.1016/j.jpowsour.2011.06.079

66. Wang D, Yan W, Botte GG (2011) Exfoliated nickel hydroxide nanosheets for urea electrolysis. Electrochem Commun 13:1135–1138 . https://doi.org/10.1016/j.elecom.2011.07.016

67. Yan W, Wang D, Botte GG (2012) Nickel and cobalt bimetallic hydroxide catalysts for urea electro-oxidation. Electrochimica Acta 61:25–30 . https://doi.org/10.1016/j.electacta.2011.11.044

68. Wang D, Yan W, Vijapur SH, Botte GG (2012) Enhanced electrocatalytic oxidation of urea based on nickel hydroxide nanoribbons. J Power Sources 217:498–502 . https://doi.org/10.1016/j.jpowsour.2012.06.029

69. Yan W, Wang D, Botte GG (2012) Electrochemical decomposition of urea with Ni-based catalysts. Appl Catal B Environ 127:221–226 . https://doi.org/10.1016/j.apcatb.2012.08.022

70. Wang D, Yan W, Vijapur SH, Botte GG (2013) Electrochemically reduced graphene oxide–nickel nanocomposites for urea electrolysis. Electrochimica Acta 89:732–736 . https://doi.org/10.1016/j.electacta.2012.11.046

71. Yan W, Wang D, Diaz LA, Botte GG (2014) Nickel nanowires as effective catalysts for urea electro-oxidation. Electrochimica Acta 134:266–271 . https://doi.org/10.1016/j.electacta.2014.03.134

72. Yan W, Wang D, Botte GG (2015) Template-assisted synthesis of Ni–Co bimetallic nanowires for urea electrocatalytic oxidation. J Appl Electrochem 45:1217–1222 . https://doi.org/10.1007/s10800-015-0846-8

73. Barakat NAM, Alajami M, Haj YA, Obaid M, Al-Meer S (2017) Enhanced onset potential NiMn-decorated activated carbon as effective and applicable anode in urea fuel cells. Catal Commun Complete:32–36 . https://doi.org/10.1016/j.catcom.2017.03.027

74. Barakat NAM, El-Newehy MH, Yasin AS, Ghouri ZK, Al-Deyab SS (2016) Ni&Mn nanoparticles-decorated carbon nanofibers as effective electrocatalyst for urea oxidation. Appl Catal Gen 510:180–188 . https://doi.org/10.1016/j.apcata.2015.11.015

75. Lan R, Tao S, Irvine JTS (2010) A direct urea fuel cell – power from fertiliser and waste. Energy Environ Sci 3:438–441 . https://doi.org/10.1039/B924786F

76. Xu W, Wu Z, Tao S (2016) Urea-Based Fuel Cells and Electrocatalysts for Urea Oxidation. Energy Technol 4:1329–1337 . https://doi.org/10.1002/ente.201600185

77. Xu W, Zhang H, Li G, Wu Z (2016) A urine/Cr(VI) fuel cell — Electrical power from processing heavy metal and human urine. J Electroanal Chem 764:38–44 . https://doi.org/10.1016/j.jelechem.2016.01.013

78. Guo F, Cao D, Du M, Ye K, Wang G, Zhang W, Gao Y, Cheng K (2016) Enhancement of direct urea-hydrogen peroxide fuel cell performance by three-dimensional porous nickel-cobalt anode. J Power Sources 307:697–704 . https://doi.org/10.1016/j.jpowsour.2016.01.042

79. Ye K, Zhang H, Zhao L, Huang X, Cheng K, Wang G, Cao D (2016) Facile preparation of three-dimensional Ni(OH)2/Ni foam anode with low cost and its application in a direct urea fuel cell. New J Chem 40:8673–8680 . https://doi.org/10.1039/C6NJ01648K

80. Xu W, Zhang H, Li G, Wu Z (2014) Nickel-cobalt bimetallic anode catalysts for direct urea fuel cell. Sci Rep 4:5863 . https://doi.org/10.1038/srep05863

81. Guo F, Cheng K, Ye K, Wang G, Cao D (2016) Preparation of nickel-cobalt nanowire arrays anode electro-catalyst and its application in direct urea/hydrogen peroxide fuel cell. Electrochimica Acta 199:290–296 . https://doi.org/10.1016/j.electacta.2016.01.215

82. Lan R, Irvine JTS, Tao S (2012) Ammonia and related chemicals as potential indirect hydrogen storage materials. Int J Hydrog Energy 37:1482–1494 . https://doi.org/10.1016/j.ijhydene.2011.10.004

83. Ye K, Wang G, Cao D, Wang G (2018) Recent Advances in the Electro-Oxidation of Urea for Direct Urea Fuel Cell and Urea Electrolysis. Top Curr Chem 376:42 . https://doi.org/10.1007/s41061-018-0219-y

84. Sahu JN, Mahalik K, Patwardhan AV, Meikap BC (2008) Equilibrium and Kinetic Studies on the Hydrolysis of Urea for Ammonia Generation in a Semibatch Reactor. http://pubs.acs.org/doi/full/10.1021/ie800481z. Accessed 17 Feb 2018

85. Uribe FA, Gottesfeld S, Zawodzinski TA (2002) Effect of Ammonia as Potential Fuel Impurity on Proton Exchange Membrane Fuel Cell Performance. J Electrochem Soc 149:A293–A296 . https://doi.org/10.1149/1.1447221

86. Singh RK, Schechter A (2018) Electrochemical investigation of urea oxidation reaction on β Ni(OH)2 and Ni/Ni(OH)2. Electrochimica Acta 278:405–411 . https://doi.org/10.1016/j.electacta.2018.05.049

87. Nagao M, Kobayashi K, Hibino T (2014) A Direct Urine Fuel Cell Operated at Intermediate Temperatures. Chem Lett 44:363–365 . https://doi.org/10.1246/cl.141067

88. Krieg BJ, Taghavi SM, Amidon GL, Amidon GE (2014) In Viv o Predictive Dissolution: Transport Analysis of the CO 2 , Bicarbonate In Vivo Buffer System. J Pharm Sci 103:3473–3490 . https://doi.org/10.1002/jps.24108

89. Xie J, Liu W, Lei F, Zhang X, Qu H, Gao L, Hao P, Tang B, Xie Y (2018) Iron-Incorporated α-Ni(OH)2 Hierarchical Nanosheet Arrays for Electrocatalytic Urea Oxidation. Chem – Eur J 24:18408–18412 . https://doi.org/10.1002/chem.201803718

90. Zhan S, Zhou Z, Liu M, Jiao Y, Wang H (2019) 3D NiO nanowalls grown on Ni foam for highly efficient electro-oxidation of urea. Catal Today 327:398–404 . https://doi.org/10.1016/j.cattod.2018.02.049

91. Ren J-T, Yuan G-G, Weng C-C, Chen L, Yuan Z-Y (2018) Uniquely integrated Fe-doped Ni(OH)2 nanosheets for highly efficient oxygen and hydrogen evolution reactions. Nanoscale 10:10620–10628 . https://doi.org/10.1039/C8NR01655K

92. Yan W, Wang D, Diaz LA, Botte GG (2014) Nickel nanowires as effective catalysts for urea electro-oxidation. Electrochimica Acta 134:266–271 . https://doi.org/10.1016/j.electacta.2014.03.134

93. Li Z-F, Wang Y, Botte GG (2017) Revisiting the electrochemical oxidation of ammonia on carbon-supported metal nanoparticle catalysts. Electrochimica Acta 228:351–360 . https://doi.org/10.1016/j.electacta.2017.01.020

94. Priyantw N, Malavipathirana S (1996) Effect of chloride irons on the electrochemical behaviour of platinum surfaces. J Natn Sci Coun Sri Lanka 24:237–246

95. Sigurdarson JJ, Svane S, Karring H (2018) The molecular processes of urea hydrolysis in relation to ammonia emissions from agriculture. Rev Environ Sci Biotechnol 17:241–258 . https://doi.org/10.1007/s11157-018-9466-1

96. Kinetic Interpretation of a Negative Time Constant Impedance of Glucose Electrooxidation | The Journal of Physical Chemistry B. https://pubs.acs.org/doi/10.1021/jp8069173. Accessed 24 Feb 2021

97. Danaee I, Jafarian M, Forouzandeh F, Gobal F, Mahjani MG (2008) Electrocatalytic oxidation of methanol on Ni and NiCu alloy modified glassy carbon electrode. Int J Hydrog Energy 33:4367–4376 . https://doi.org/10.1016/j.ijhydene.2008.05.075

98. Gira MJ, Tkacz KP, Hampton JR (2016) Physical and electrochemical area determination of electrodeposited Ni, Co, and NiCo thin films. Nano Converg 3:6 . https://doi.org/10.1186/s40580-016-0063-0

99. Hahn F, Beden B, Croissant MJ, Lamy C (1986) In situ uv visible reflectance spectroscopic investigation of the nickel electrode-alkaline solution interface. Electrochimica Acta 31:335–342 . https://doi.org/10.1016/0013-4686(86)80087-1

100. Bard AJ, Faulkner LR (2001) Electrochemical Methods Fundamentals and Applications

101. Gosting LJ, Akeley DF (1952) A Study of the Diffusion of Urea in Water at 25° with the Gouy Interference Method1. J Am Chem Soc 74:2058–2060 . https://doi.org/10.1021/ja01128a060

102. Soper AK, Castner EW, Luzar A (2003) Impact of urea on water structure: a clue to its properties as a denaturant? Biophys Chem 105:649–666 . https://doi.org/10.1016/S0301-4622(03)00095-4

103. Ramondo F, Bencivenni L, Caminiti R, Pieretti A, Gontrani L (2007) Dimerisation of urea in water solution: a quantum mechanical investigation. Phys Chem Chem Phys 9:2206–2215 . https://doi.org/10.1039/B617837E

104. Newman J, Thomas-Alyea KE (2004) Electrochemical Systems, 3rd Edition, 3rd ed. Hoboken, NJ: John Wiley & Sons, Inc.

105. Schranck A, Marks R, Yates E, Doudrick K (2018) Effect of Urine Compounds on the Electrochemical Oxidation of Urea Using a Nickel Cobaltite Catalyst: An Electroanalytical and Spectroscopic Investigation. Environ Sci Technol 52:8638–8648 . https://doi.org/10.1021/acs.est.8b01743

106. Xu W, Wu Z, Tao S (2016) Urea-Based Fuel Cells and Electrocatalysts for Urea Oxidation. Energy Technol 4:1329–1337 . https://doi.org/10.1002/ente.201600185

107. Kou T, Wang S, Hauser JL, Chen M, Oliver SRJ, Ye Y, Guo J, Li Y (2019) Ni Foam-Supported Fe-Doped β-Ni(OH)2 Nanosheets Show Ultralow Overpotential for Oxygen Evolution Reaction. ACS Energy Lett 4:622–628 . https://doi.org/10.1021/acsenergylett.9b00047

108. Mahala C, Devi Sharma M, Basu M (2019) Fe-Doped Nickel Hydroxide/Nickel Oxyhydroxide Function as an Efficient Catalyst for the Oxygen Evolution Reaction. ChemElectroChem 6:3488–3498 . https://doi.org/10.1002/celc.201900857

109. Wang G, Ye K, Shao J, Zhang Y, Zhu K, Cheng K, Yan J, Wang G, Cao D (2018) Porous Ni2P nanoflower supported on nickel foam as an efficient three-dimensional electrode for urea electro-oxidation in alkaline medium. Int J Hydrog Energy 43:9316–9325 . https://doi.org/10.1016/j.ijhydene.2018.03.221

110. Nim YS, Wong K-B (2019) The Maturation Pathway of Nickel Urease. Inorganics 7:85 . https://doi.org/10.3390/inorganics7070085

111. Wright JC, Michaels AS, Appleby AJ (1986) Electrooxidation of urea at the ruthenium titanium oxide electrode. AIChE J 32:1450–1458 . https://doi.org/10.1002/aic.690320906

112. Rikitake K, Oka I, Ando M, Yoshimoto T, Tsuru D (1979) Creatinine Amidohydrolase (Creatininase) from Pseudomonas putida: ePurification and Some Properties. J Biochem (Tokyo) 86:1109–1117 . https://doi.org/10.1093/oxfordjournals.jbchem.a132605

113. Zhou Z, Liu Y, Zhang J, Pang H, Zhu G (2020) Non-precious nickel-based catalysts for hydrogen oxidation reaction in alkaline electrolyte. Electrochem Commun 121:106871 . https://doi.org/10.1016/j.elecom.2020.106871

114. Mandal M (2021) Recent Advancement on Anion Exchange Membranes for Fuel Cell and Water Electrolysis. ChemElectroChem 8:36–45 . https://doi.org/10.1002/celc.202001329

115. Lindquist GA, Xu Q, Oener SZ, Boettcher SW (2020) Membrane Electrolyzers for Impure-Water Splitting. Joule 4:2549–2561 . https://doi.org/10.1016/j.joule.2020.09.020

116. Britton B, Holdcroft S (2016) The Control and Effect of Pore Size Distribution in AEMFC Catalyst Layers. J Electrochem Soc 163:F353 . https://doi.org/10.1149/2.0421605jes

117. Stanislaw LN, Gerhardt MR, Weber AZ (2019) Modeling Electrolyte Composition Effects on Anion-Exchange-Membrane Water Electrolyzer Performance. ECS Trans 92:767 . https://doi.org/10.1149/09208.0767ecst

118. Huang L-F, Hutchison MJ, Santucci RJ, Scully JR, Rondinelli JM (2017) Improved Electrochemical Phase Diagrams from Theory and Experiment: The Ni–Water System and Its Complex Compounds. J Phys Chem C 121:9782–9789 . https://doi.org/10.1021/acs.jpcc.7b02771

119. Mundra S, Criado M, Bernal SA, Provis JL (2017) Chloride-induced corrosion of steel rebars in simulated pore solutions of alkali-activated concretes. Cem Concr Res 100:385–397 . https://doi.org/10.1016/j.cemconres.2017.08.006

120. Taylor CD, Li S, Samin AJ (2018) Oxidation versus salt-film formation: Competitive adsorption on a series of metals from first-principles. Electrochimica Acta 269:93–101 . https://doi.org/10.1016/j.electacta.2018.02.150

121. Ma F-Y (2012) Corrosive Effects of Chlorides on Metals. In: Pitting Corrosion

122. Anderko A, Sridhar N, Jakab MA, Tormoen G (2008) A general model for the repassivation potential as a function of multiple aqueous species. 2. Effect of oxyanions on localized corrosion of Fe–Ni–Cr–Mo–W–N alloys. Corros Sci 50:3629–3647 . https://doi.org/10.1016/j.corsci.2008.08.046

123. Ayoub H, Griveau S, Lair V, Brunswick P, Cassir M, Bedioui F (2010) Electrochemical Characterization of Nickel Electrodes in Phosphate and Carbonate Electrolytes in View of Assessing a Medical Diagnostic Device for the Detection of Early Diabetes. Electroanalysis 22:2483–2490 . https://doi.org/10.1002/elan.201000307

124. Bohé AE, Vilche JR, Arvia AJ (1990) The electrochemical behaviour of polycrystalline nickel electrodes in different carbonate-bicarbonate ion-containing solutions. J Appl Electrochem 20:418–426 . https://doi.org/10.1007/BF01076050

125. Buxton S, Garman E, Heim KE, Lyons-Darden T, Schlekat CE, Taylor MD, Oller AR (2019) Concise Review of Nickel Human Health Toxicology and Ecotoxicology. Inorganics 7:89 . https://doi.org/10.3390/inorganics7070089

APPENDIX A: URC Anode Preparation Procedure

Name	Abbreviation	Vendor	Catalog #
Nickle foam, 1.6 mm	Ni F	Sigma Aldrich	GF28024657
urea	-	Sigma Aldrich	U5128
Nickle nitrate hexahydrate	$Ni(NO_3)_2 \cdot 6H_2O$	Sigma Aldrich	203874
Deionized water	DI H_2O	From Milli-Q Filtration unit	Direct Q3 UV
Concentrated HCl	-	Sigma Aldrich	H1758
Ethanol	-	Sigma Aldrich	459836
1000 mL PTFE-lined hydrothermal reactor	-	Xian Toption Instrument Co. Limited	TOPT--HT 1000ml (200 °C)
oven	-	Isotemp Oven	Did not purchase
Ultrasound bath	-	Branson 1510	Did not purchase
Laser cutter	-	Universal laser systems	Did not purchase

Table A.1 List of materials needed to follow the procedure outlined below for making NHF anodes for the URC.

Procedure:

1. Use laser cutter to precisely cut 25 cm^2 Ni foam into the number of electrodes required. Any number of electrodes that fit into hydrothermal reactor is permissible. NHF electrodes are stable at ambient conditions, so they may be made in batches and stored for long periods of time. Before cleaning the Ni foam substrates, practice arranging the cut Ni foam pieces into the autoclave PTFE crucible, so they stand upright rather than lay flat. If about eight or more electrodes are made simultaneously, they will each support their neighbor; otherwise, it is necessary to insert clean PTFE supports to ensure they remain upright throughout the duration of the hydrothermal growth. Other factors like spacing and whether electrodes touch during growth are not important, so long as they remain vertical. Once Ni foam pieces

are properly arranged in PTFE crucible, measure the amount of fluid needed to completely cover the electrodes by at least 2 cm of fluid. The vessel may be filled completely if necessary, however, resources are conserved if the headspace is appropriately determined based on electrode arrangement. Record the volume needed for Step 3.

2. In the hood, clean Ni foam by soaking for 5 minutes in 6 M HCl. Rinse well with a squeeze bottle of DI H_2O, followed by ethanol and let each Ni foam piece dry completely in the hood, about 10 minutes. Once fully dry, record the mass of each Ni foam piece. The mass of each laser-cut Ni foam piece should be consistent.
3. While the clean Ni foam pieces dry, mix the hydrothermal bath solution containing 0.125 M urea and 0.0125 M $Ni(NO_3)_2{\cdot}6H_2O$ to the total volume required, from Step 1. Example calculations to determine mass for urea and $Ni(NO_3)_2{\cdot}6H_2O$ are calculated on a basis of 0.9 L below. Using a laboratory balance, tare an empty volumetric flask and add required mass of each solute; add DI H_2O to the proper volume. The solutes will dissolve easily into the solution at these concentrations and the solution will turn a pale green.

	Concentration (M)	Moles	MW (g/mole)	Mass (g)
Urea	0.125	0.113	60.06	6.76
$Ni(NO_3)_2{\cdot}6H_2O$	0.0125	0.0113	290.8	3.27

4. Place the PTFE crucible inside the stainless-steel autoclave exterior with the lid off. Arrange the fully dried Ni foam pieces in the PTFE crucible as decided in Step 1. Carefully pour the solution made in Step 3 into the vessel being sure not to displace the Ni foam pieces. It is

important that they each remain vertical during growth. Place the PTFE lid onto the crucible and cover with the stainless-steel top plate. Align the 6 bolt holes for the top and bottom stainless-steel plates and slide the bolts into place. The bolts may require bolt grease if they do not tighten smoothly. In a star pattern, tighten each bolt with a wrench until they all feel equally tight and resistance to tightening is achieved—torque wrench not required. See picture to right for image of 1.0 L PTFE-lined hydrothermal reactor and bolts.

5. Preheat the oven to 105 °C. Carefully place the entire vessel into the oven and secure the door; leave hydrothermal reactor in the oven for 12 hours.
6. After 12 hours remove the reactor from the oven and place on lab bench to naturally cool, about 4 hours or overnight. Turn off the oven. Once the reactor is cool, remove the bolts, stainless steel plate, and PTFE crucible lid. The solution will have green $Ni(OH)_2$ precipitate, and the Ni foam substrates will now have NHF growth. With a pair of tweezers, carefully remove each NHF electrode from the hydrothermal bath and rinse with DI H_2O, either with a gentle spray from a squeeze bottle or with a bath, until it is precipitate-free. The hydrothermal solution is alkaline and should be placed in proper waste disposal container. Let all electrodes dry at room temperature, or up to 50 °C in oven, and cool completely before weighing and recording the mass of each electrode. The average catalyst loading should be about 1 mg/cm^2 of geometric area. The electrodes are now ready for characterization and/or

storage. If characterizing, a single electrode can be representative for the batch. If storing, ensure the storage location is within a rigid container where the electrodes will not be compressed before mounting into the URC. Storing may be done at room temperature and atmospheric pressure; shelf life is long.

Characterization:

NHF electrodes will be slightly darker and have a subtle green tint compared to clean NF, as seen in photo at left (NHF top, clean NF bottom). Mass loading recorded in Step 6 and visual differences will generally be a suitable confirmation for NHF growth; however, SEM can be used for additional characterization when required or desired.

Electron imaging is available with the FEI XL830 Dual Beam FIB/SEM in the Molecular Analysis Facility (MAF) on UW campus in the basement of the Molecular Engineering and Sciences building. Clean the mounting stage with ethanol and mount a small (1 cm^2 is plenty) piece of NHF onto the mounting stage using the stainless-steel securing pieces to ensure it is held in place without being compressed. Do the same for a piece of clean Ni foam. Follow the SEM SOP and capture images of both the clean Ni F and the NHF at magnifications of 5000x or above. All surfaces of the NHF will exhibit “nanowalls” of $Ni(OH)_2$ at higher magnification. Additionally, some “flowerlike” structures (microparticles with nanowalls grown on them) are observed, but do not cover the surface. Below are example micrographs of 5000x and 25000x comparing NHF

and clean Ni F; because Ni F does not have intricate surface morphology like NHF, the 25000x micrograph was not captured.

	NHF	Ni Foam
5000x	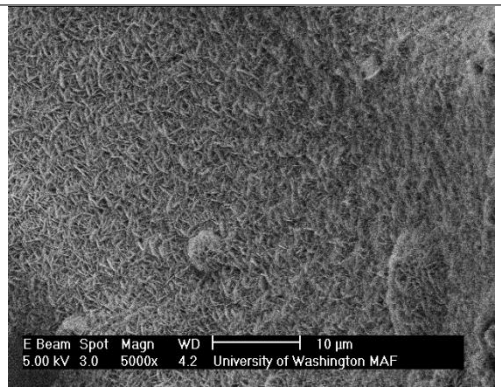	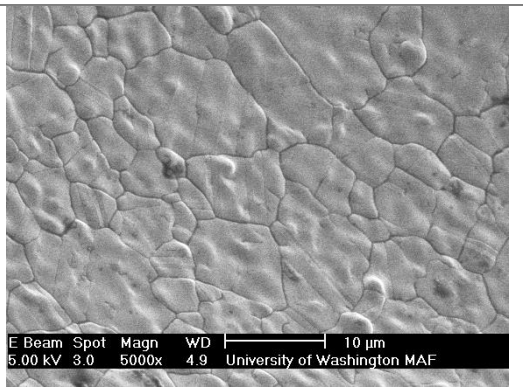
25000X	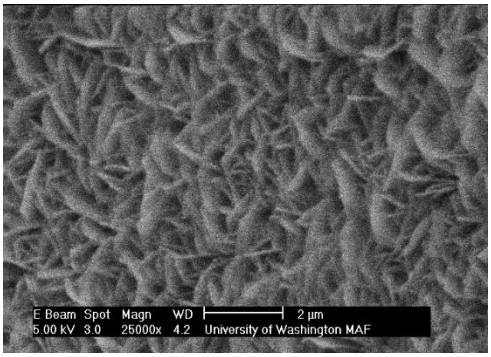	N/A

APPENDIX B: URC Cathode Preparation Procedure

Name	Abbreviation	Vendor	Catalog #
20% Platinum on Vulcan XC-72R	20% Pt/C	Fuel Cell Store	3151721
10 % FAA-3 in NMP	Ionomer	Fuel Cell Store	72500310
Methanol	MeOH	Sigma Aldrich	322415
Ultrasonic bath	-	Branson 1510	Did not purchase
Carbon cloth 1071 HBC	CC	Fuel Cell Store	1592020
Deionized water	DI H_2O	From Milli-Q Filtration unit	Direct Q3 UV
Laser Cutter	-	Universal Laser Systems	Did not purchase
Tetrahydrofuran	THF	Sigma Aldrich	401757
airbrush	-	Iwata	HP-C
Compressed air cylinder	-	Praxxair	Industrial grade

Table A.2 List of materials needed to follow the procedure outlined below for making Pt/C cathodes for the URC.

Procedure:

Steps 1–5 outline how to prepare the catalyst ink; steps 6–10 outline how to spray the ink onto the carbon cloth substrate as a catalyst layer to make the gas diffusion electrode (GDE). It is most efficient to spray multiple electrodes at one time because it eliminates losses due to overspray and container walls. This procedure should be started in the morning so that at least steps 1–9 may be completed in the same day.

1. Based on electrode size, number, desired loading, and excess for overspray, calculate the mass of each ingredient needed for the ink recipe. The mass percentages of each ingredient are as follows: 96% solvent (1:1 volume of MeOH and THF), 3% ionomer (10 % FAA-3 in NMP),

1% catalyst powder (20% Pt/C). Cathodes are made to have a 1 mg/cm^2 Pt loading, which can be verified based on final electrode mass.

Example calculations to make 16x 25 cm^2 electrodes for the URC with 10% excess using the mass percentages listed in Step 1. Final mass of each ingredient emphasized in bold.

Total area = (16 cells * 25cm^2)*1.1 = 440 cm^2

Mass of Pt = 1.0 mg/cm ^{2}*440 cm^2 = 0.44 g

Mass of catalyst powder: 0.44 g/0.2 = **2.20 g**

Final mass of ink: 2.20 g/0.01 = 220 g

Mass solvent: 220 g * 0.96 = 211.2 g = **105.6 g** of each solvent

Mass of ionomer: 220 g * 0.03 = **6.6 g**

2. Measure amount of Pt/C powder calculated in Step 1 into a sealable glass vessel appropriately sized to hold the final volume of ink. Wet the catalyst powder with DI H_2O (volume depends on amount of catalyst used, usually ~10–75 mL) into a slurry before adding solvent in Step 3. This step ensures there are no sparks formed due to Pt catalyzing the combustion of methanol in air, which is a safety hazard and consumes the Pt catalyst.
3. Prepare a solution of 1:1 volume MeOH and THF. This can be mixed into a squeeze bottle to use for ink recipe and airbrush cleaning (Step 8, 9); excess should be labeled, and stored in the flammables cabinet. Measure the amount of each solvent calculated in Step 1 into a separate container using a laboratory balance. Add the measured solvents to the fully wetted

catalyst, insert stir bar and place on stir plate. Keep the ink solution mixing for 30 minutes before moving to Step 4.

4. Measure the amount of ionomer (10% FAA-3 in NMP) calculated in Step 1 into a separate vessel on the laboratory mass balance. Using a pipette, add the ionomer dropwise (~2 drops per second) to the ink solution while it continues stirring briskly to encourage dispersion. Once all the ionomer is added to the ink solution, cap the vessel, seal with parafilm, and continue mixing vigorously for 1 hour.
5. Place ink in sonication bath for 1 hour. When sonication is done move it *immediately* back to stir plate. If the catalyst is left to settle out of solution even for a couple of minutes, it will need to undergo the sonication bath process again. The ink is now ready to be sprayed onto cathode substrates. It is important to always keep the vessel of ink mixing on the stir plate without letting it settle. During the spraying process (Step 6–9) only a few mL will be in the airbrush at a time, while the rest of the ink remains sealed and stirring. Even when continuously stirred, ink does not store well and should be sprayed within 24 hours.
6. Manually cut a single piece of carbon cloth to dimensions that allow for cutting the individual *square* electrodes after ink dries. For example, based on Step 1 calculations, 400 cm^2 of substrate are needed for 16 electrodes with side lengths of 5 cm. A carbon cloth piece that is 16 cm x 25 cm will only allow 15 electrodes to be cut. A CC piece that is 10 cm x 40 cm (with 1–2 cm excess around all sides) will allow all 16 electrodes to be cut.
7. Place a hotplate in the hood. Wrap hotplate surface in aluminum foil (for protection from ink overspray) and preheat to 80–100 °C. Place the carbon cloth onto hotplate. The heat will

cause the solvent to evaporate quickly and allow successive layers to be sprayed without ink pooling. If the carbon cloth piece has dimensions larger than the hotplate surface, it must be pulled with one hand during the spray process, as noted in Step 8.

8. Connect the airbrush to a compressed air or N_2 gas cylinder. Pressure on the tank should be less than 20 psig to achieve even spray of solvent. If higher pressure is needed, check to make sure airbrush is clean and assembled properly. Use a pipette to transfer ~2 mL of ink to fill the airbrush cup while the rest of the ink solution remains stirring in sealed vessel. Spray one layer of ink onto the full CC surface one layer at a time by moving airbrush in a steady serpentine fashion. For a consistent final catalyst layer thickness, do not spray multiple layers on the same area of cloth before spraying the entire carbon cloth surface. Refill the airbrush as required and continue along spray path. Eventually the entire electrode surface will be black, and it will be difficult to determine where you have sprayed and where you have not, so it is important to pick a spray pattern and stick to it without getting distracted. This requires practice for uniform coverage. Nozzle distance that is too close (ideally ~2”), or nozzle movement that is too slow (2 mL will take ~30 sec. to spray) will result in pooled ink. Nozzle distance that is too far or nozzle movement that is too quick may result in greater overspray, sloppy lines, and less even coating. If the piece of carbon is wider and/or taller than the hotplate, it is necessary to reposition it during spraying. To reposition, gently pull the carbon cloth in a smooth motion with one hand and continue evenly coating the surface with other hand. Work quickly so nozzle does not clog with dried ink. Keep a solution of MeOH and THF solvent to rinse airbrush cup when clogging begins to occur, usually after ~2–5 cup refills.

Either turn the substrate 180° or reverse the serpentine spray movement every few layers to achieve an even coating thickness.

9. Continue spraying until all ink is gone. Ink will dry nearly immediately throughout spray process. If ink pools even at 100 °C, spray from a farther distance or at a faster pace. Once a new layer is sprayed, the existing layer's ink should be completely dry before the next layer is sprayed. This process usually takes 1–4 hours depending on amount of ink mixed. Let the GDE dry for ~10 minutes on the hotplate before turning off. Leave the GDE to fully dry in the hood for a few more hours. Clean airbrush by flushing solvent through until the spray lines dry clear on a white paper towel. Then disassemble and clean the airbrush according to the user manual. Turn off gas cylinder.
10. Use the laser cutter to cut individual electrodes from the one large piece to proper dimensions. Weigh each electrode and calculate final mass loading using the density of CC 1071 HBC, 132 g/m^2.

Characterization:

Example of Pt mass loading calculation for a 25 cm^2 cathode.

Initial mass: 13.2 mg/cm^2 * 25 cm^2 = 330 mg

Final dry mass: 452 mg

Mass loading Pt: (452 mg –330 mg)*0.2/25 cm^2 = **0.98 mg/cm^2**

A loading that is lower than the targeted 1 mg/cm^2 indicates that the amount of ink lost to overspray/vessel walls was larger than expected. Variations in final mass loading of GDEs within a single batch indicate inconsistent spray technique.

If Pt mass loading is below 0.8 mg/cm^2 the electrodes may still be used but checked for activity once mounted in the cell. This is done by mounting the cathode into the URC. During operation at 1.6 V_{cell} or above, if differences in cathode flowrate affect the overall cell current, then the cathode reaction is limiting cell performance.

SEM may also be used for verification of microstructure morphology. Below are some example SEM micrographs of a Pt/C catalyst layer at magnifications from 250—10,000x. Microporous structure is apparent at magnifications higher than 5,000x. Additionally, no catalyst layer cracking or flaking should be observed at any magnification.

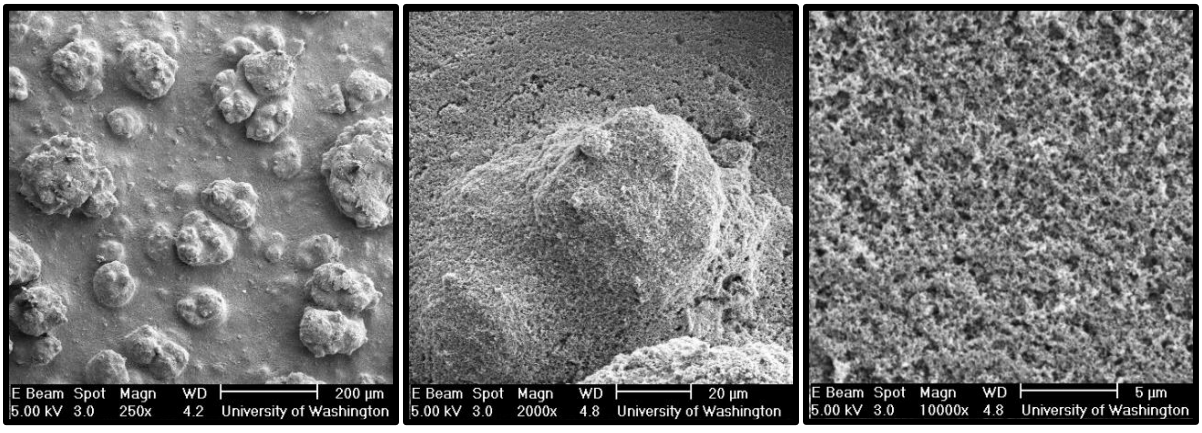

APPENDIX C: Ni Foam WE Preparation Procedure

Name	details	Vendor	Catalog #
Disposable Pasteur pipettes	2 mL Borosilicate glass 5 ¾”	VWR.com	14673-101
Cu wire	18-gauge (1mm diameter)	Sigma Aldrich	349216-70G
Male quick-disconnect	18–22-gauge, 0.187” diameter	McMaster Carr	69525K65
Female/male snap plug pair	18–22-gauge, 0.156” diameter	McMaster Carr	71285K11/ 71285K13
Ni wire	18-gauge (1 mm diameter)	Sigma Aldrich	GF45846456-1EA
Low-viscosity Resin (Part A)	Mas Epoxies	Fisheries Supply	55034
Slow Epoxy hardener (Part B)	Mas Epoxies	Fisheries Supply	55036
Epoxy	JB Weld 5-minute epoxy adhesive	Grainger	453U41
Disposable mixing container	50 mL plastic beakers	Grainger	23YW44
Spot welder	250 Watt-Seconds Resistance Spot Welder	Unitek	Did not purchase
Laser Cutter	In Bindra Lab, Benson Hall UW	Universal Laser Systems	Did not purchase

Table A.3 List of materials needed to follow the procedure outlined below for making Ni foam-based WEs.

Procedure:

Steps 1–5 are for the assembly of a WE holder that multiple WE heads can be mounted onto. Steps 6–8 are for the assembly of the replaceable WE heads. The figures below show a fabricated WE holder with a 0.5 cm^2 NHF WE head; the head is connected in the first photo and disconnected in the second.

1. Break off narrow tip of glass pipette so that 18-gauge (1.27 mm diameter) copper wire can slide through easily. Sand the sharp edge until smooth. The shaft of this glass pipette is perfectly sized to form a seal with the Pine Research electrochemical cell used for testing.
2. Cut a piece of 18-gauge Cu wire to extend about 1 cm from each end of sanded glass pipette. Final length will be ~13 cm and depend on length of glass pipette once fully sanded.
3. With the glass tubing strung on the wire, crimp a 0.187” 18–22-gauge male quick disconnect piece to the top end (wider glass tube diameter) and a 0.156” 18–22-gauge male snap plug to the bottom end (narrow glass tube diameter)
4. Epoxy the Cu wire at the top (narrow end, where male quick disconnect is) to the glass tubing. Make sure not to get epoxy on the male quick disconnect terminal, which must make electrical contact with the potentiostat during experiments. More epoxy here is helpful to ensure the resin does not leak in Step 5; epoxy will later be removed to ensure total diameter does not exceed glass body. The epoxy will solidify in 5 minutes. Wait 1 hour for the epoxy to

fully cure. Use a voltmeter, with leads placed on each end of the WE holder, to ensure the total resistance measured is no more than 0.2 Ω. before moving to Step 5.

5. Use a ring stand to vertically hold WE holder(s) epoxy-side down. Only ~3 mL of resin needed per WE holder. Mix appropriate volume of low-viscosity resin (2 parts resin: 1 part hardener) according to instructions. If resin is not precisely measured and thoroughly mixed, the resin will not cure. Use a disposable mixing container and tool. Once the resin is well mixed, pour immediately into the vertically held WE holder(s). Resin becomes more viscous as it cures and is difficult to work with after 10–15 minutes. Fill each glass tube completely. Some small air bubbles will rise to the top after a few minutes. If needed, top off with another pour of resin to ensure the resin fills the glass cavity completely. The resin will harden to touch in 30 minutes. Let cure completely overnight. Once fully cured, the resistance of each WE holder should still be no more than 0.2 Ω. Peel and/or sand the epoxy from the glass body wherever excess was used. The WE holder is complete when it fits securely into the 150 ml Pine electrochemistry three-electrode cell.
6. Use laser cutter to cut 0.5 cm x 1.0 cm of Ni foam pieces to ensure they are all identical in size/surface area. For each Ni foam piece, cut ~3 cm of 1 mm diameter Ni wire. The exact length is not important, though they should all be the same length so that each final WE head has the same mass (helpful for mass loading comparisons). Spot weld one clean wire piece onto one clean Ni foam piece using the 20% power setting on the spot welder in Benson B5. Spot weld in 3 locations along the joint for good electrical contact. More spot-welded joints will cause the Ni foam to melt down the middle joint and split in two pieces rendering the WE

head useless. Fewer spot-welded joints will result in more electrical resistance. The resistance for the WE should be ~0.6 Ω when measured with a voltmeter.

7. If growing NHF, place the spot-welded foam/wire (before female snap plug is added) into a PTFE-lined hydrothermal vessel and follow appropriate hydrothermal growth procedure.

8. Once electrodes are removed from hydrothermal vessel, and cleaned according to protocol, wipe the $Ni(OH)_2$ from the Ni wire with a Kim wipe before placing *just the wire end* (highlighted in red on image to right, although this step is done before female snap connector is mounted) into 3 M HCl for 30 minutes to reduce surface $Ni(OH)_2$ to ensure low resistance of the WE head. Rinse multiple times with DI H_2O and dry completely. Record mass of each electrode to determine mass loading. Crimp a female snap connector onto the free, acid cleaned Ni wire end. The female snap connector on the WE head connects to the male snap connector on the WE holder for mounting and use within the three-electrode cell.

Characterization:

If the total resistance of the WE holder with mounted head is <2 Ω the WE is ready to use. Eventually heads and holders both fail, as determined by high resistance (>5 Ω).

APPENDIX D: Chapter 6 Supplementary Information

Electrochemical surface area (ECSA) for each electrode was calculated based on Equation 3.2. Table A.4 lists results of ECSA calculations where E_0 and E_2 are the charge (Q) integration limits. Designations A and B indicate different electrodes of same catalyst type, and asterisks (*) indicate which electrodes were used in Chapter 4 figures. All voltages reported in tables are referenced to Hg/HgO in pH 14.

Electrode	Date	E_0 (V)	E_2 (V)	Q (C)	ECSA (cm^2)
Ni Foam, A	03/16/20	0.4416	0.5720	0.0115	44.76
Ni Foam, B	03/16/20	0.4507	0.5741	0.0144	56.12
Ni Foam, B*	03/17/20	0.4416	0.5759	0.0149	58.00
NHF, A	10/21/19	0.3967	0.6586	0.5283	2055.76
NHF, B*	03/17/20	0.4109	0.6308	0.1289	501.63
Fe-NHF, A	10/21/19	0.3483	0.6185	0.3306	1286.26
Fe-NHF, B	03/10/20	0.4070	0.6412	0.3050	1186.76
Fe-NHF, A*	03/18/20	0.4108	0.6048	0.2298	893.97

Table A.4 Anodic charge passed (Q) between E_0 and E_2 during blank scans, and the resulting ECSA calculated for each electrode and date tested.

Table A.5 and Table A.6 report values extracted from dialysate-relevant CV experiments performed on the above electrodes with 10 mM urea and 0–180 µm creatinine. The OER slope (m) was calculated between two points in the linear region of the CVs and extrapolated to determine the potential at which OER onset begins (E_1). The raw charge integration (Q_{raw}) between E_0 and E_2 and OER-corrected charge (Q_{ox}) on each electrode are listed in Table A.6. When $E_1 > E_2$, then Q_{raw} is equivalent to Q_{ox} because the charge is measured in a region before OER dominates; this occurs in all Ni foam and one NHF experiment. Because ECSA changes between electrodes and dates, the ECSA normalized oxidation charge (Q_{ECSA}) is also calculated in Table A.6, based on ECSA values in Table A.4.

Catalyst	[Creatinine] (mM)	$m\left(\frac{A}{\mathrm{cm}_{\mathrm{geo}}^2 \mathrm{V}}\right)$	E_0 (V)	E_1 (V)	E_2 (V)
Ni foam, A	0	0.1521	0.4226	0.6210	0.6263
	0.06	0.2760	0.4330	0.6486	0.6143
Ni foam, B	0	0.5837	0.4475	0.6610	0.6028
	0.06	0.5066	0.4470	0.6481	0.5968
Ni foam, B*	0	0.4981	0.4398	0.6605	0.6102
	0.06	0.5533	0.4456	0.6668	0.6081
NHF, A	0	0.6630	0.2319	0.6676	0.7045
	0.06	0.7370	0.3577	0.6774	0.7024
NHF, B*	0	0.3743	0.3580	0.6898	0.6763
	0.06	0.3600	0.3539	0.6878	0.6776
	0.12	0.3522	0.3057	0.6856	0.6750
	0.18	0.3803	0.3517	0.6927	0.6719
Fe-NHF, A	0	0.6802	0.1350	0.6035	0.6498
	0.06	0.8050	0.1167	0.6168	0.6527
Fe-NHF, B	0	0.3722	0.3803	0.6137	0.7059
	0.06	0.4318	0.3568	0.6275	0.7065
Fe-NHF, A*	0	0.6040	0.3992	0.6107	0.6434
	0.06	0.5881	0.3476	0.6076	0.6557
	0.12	0.6018	0.3946	0.6130	0.6597
	0.18	0.6157	0.3799	0.6154	0.6594

Table A.5 Calculated OER slope (m), charge integration limits (E_0, E_2), and voltage intercept for OER (E_1). All experiments contained 10 mM urea in addition to creatinine concentration listed.

Catalyst	[Creatinine] (mM)	Q_{raw} (C)	Q_{ox} (C)	Q_{ESCA} (C/cm^2)	%change creatinine	Average %change 0.06 mM creatinine
Ni foam, A	0	0.0635	0.0633	1.41E-03		-14.1
	0.06	0.0550	0.0550	1.23E-03	-13.1	
Ni foam, B	0	0.0591	0.0591	1.05E-03		
	0.06	0.0461	0.0461	8.21E-04	-22.0	
Ni foam, B*	0	0.0598	0.0598	1.03E-03		
	0.06	0.0556	0.0556	9.58E-04	-7.1	
NHF, A	0	1.0010	0.9560	4.65E-04		-2.9
	0.06	0.9404	0.9173	4.46E-04	-4.0	
NHF, B*	0	0.3527	0.3527	7.03E-04		
	0.06	0.3467	0.3467	6.91E-04	-1.7	
	0.12	0.3398	0.3398	6.77E-04	-3.7	
	0.18	0.3122	0.3122	6.22E-04	-13.0	
Fe-NHF, A	0	0.6908	0.6179	4.80E-04		14.0
	0.06	0.7596	0.7076	5.50E-04	14.5	
Fe-NHF, B	0	0.7574	0.5993	5.05E-04		
	0.06	0.7923	0.6576	5.54E-04	9.7	
Fe-NHF, A*	0	0.4946	0.4624	5.17E-04		
	0.06	0.6120	0.5440	6.08E-04	17.6	
	0.12	0.6265	0.5610	6.28E-04	26.7	
	0.18	0.6391	0.5796	6.48E-04	29.2	

Table A.6 Designations A and B indicate different electrodes of same catalyst type, and * indicates which electrodes were used in figures. All voltages reported are referenced to Hg/HgO in pH 14.

APPENDIX E: URC Assembly, Start-up, and Operation

Chemical/Equipment/Specs	CAS #	Vendor	Catalog #
Anode (Appendix A)	-	-	-
Cathode (Appendix B)	-	-	-
Anion Exchange Membrane	-	Fuel Cell Store	5041624
Anode gasket, 1/16” silicone	-	McMaster Carr	1460N12
Scribner flow cell + accessories	-	Scribner	Flow Cell Fixture
Potentiostat	NA	Solartron	1287A
Urea	57-13-6	Sigma-Aldrich	U5128
$KHCO_3$	298-14-6	Sigma-Aldrich	237205
KOH	57-13-6	Sigma-Aldrich	U5128
NaCl	7647-14-5	Sigma-Aldrich	S9888
CO_2	124-38-9	Praxair	CD 5
DI H_2O	N/A	From Mili-Q system	Direct Q-3
Torque wrench	-	Fisher Scientific	NC1276757
CO_2 flowmeter	-	Sigma Aldrich	23320-U
Stainless steel mesh	-	McMaster Carr	1063T11
Cathode gasket, 1/32” PTFE	-	McMaster Carr	1063T11
Hotplate	-	Fisher Scientific	SP88850200
pH meter	-	Thermo Scientific	VSTAR90
Laser Cutter	-	-	-
KimWipes	-	Sigma Aldrich	Z188956-1PAK
Staco Variable Transformer	-	Galco.com	3PN1010B

Table A.7 List of materials needed to follow the procedure outlined below for assembly, start-up, and operation of the URC.

Solution Preparation

The anode and cathode each need their own feed solutions. The anode utilizes a solution containing urea (2–10 mM) in bicarbonate (25–100 mM) and NaCl (0–0.15 M), where concertation of each component depends on experimental design. The temperature of the anode feed solution should be kept at 37 °C using a hotplate and a stir bar mixing ~300–600 RPM to decrease thermal gradients. When mixed vigorously and open to the atmosphere, the bicarbonate buffer system will off-gas CO_2 and become more alkaline. As such, it is desirable to use a sealable vessel and control the solution pH at 7.4 by use of CO_2 partial pressure in the solution headspace. A pH meter is kept in the solution and the CO_2 flowrate (<50 mL/min needed) is manually adjusted using a needle valve rotameter to maintain a pH of 7.4. The cathode solution is DI water which does not need to be pH or temperature controlled. Below is a labeled photo of the URC experimental setup.

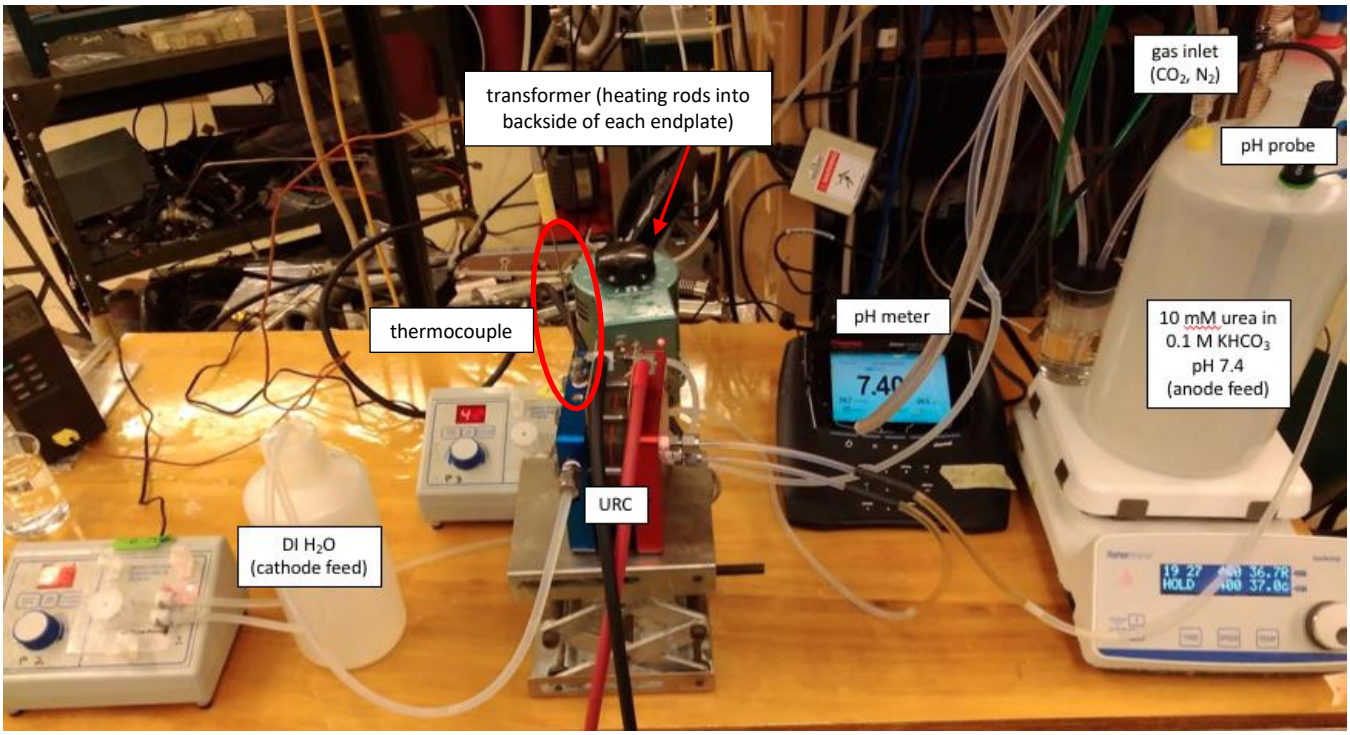

Cell Assembly/Membrane Activation

See separate protocols for URC anode and cathode manufacturing (Appendices A, B). Once the anode and cathodes are made, follow Steps 1–9 for URC Assembly and Step 10 for Membrane Activation.

1. Cut an anion exchange membrane (AEM) to the proper size, including alignment holes, using the acrylic gasketing template that comes with the cell. Usually only one membrane is cut and soaked at a time because AEMs should be stored in KOH until they are used, yet they should not be stored in KOH for longer than 3 weeks per manufacturer (FuMA-Tech) instructions. Soak AEM in 1–2 M KOH for at least 18 hours before moving to step 2. This exchanges the bromide anions in the dehydrated membrane with hydroxide ions and hydrates the AEM. The

membrane will begin to curl over itself once exposed to moisture which makes it hard to mount into the URC later; soak the AEM while it is clamped between two stainless steel (SS) mesh screens cut to the same size to keep it flat, shown in photo at right. Keep the membrane soaking in a properly labeled, sealed vessel in the Bases cabinet for at least 18 hours (yet no longer than 3 weeks) before beginning Step 5.

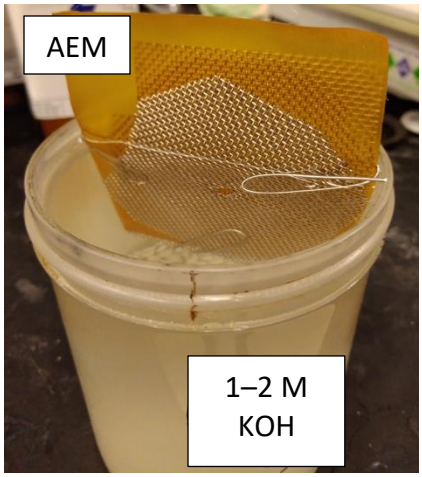

2. Prepare electrodes for the URC by following appropriate protocol (Appendix A for URC anodes and Appendix B for URC cathodes).
3. Cut gaskets for URC, with alignment holes, using the acrylic gasket template and a sharp razor blade. Alternatively, use the laser-cutter for more precise cutting. Gasketing for the anode (when it is Ni foam-based), is 1/16” silicone. Gasketing for the cathode is 1/32” PTFE.
4. Prepare the URC hardware for mounting the electrodes, gaskets, and AEM. The blue endplate is for the cathode (negative terminal) and the red endplate is for the anode (positive terminal). The blue endplate is not compatible with alkaline solution, which is needed on the anode for cell activation, and therefore it is important to not mix up the two endplates. All flow field plates (FFPs), gaskets, and current collectors (CCs) should be wiped with ethanol to clean before assembly. Aside from this SOP, an instructional video from Scibner is provided at http://www.scribner.com/products/fuel-cell-test-accessories/fuel-cell-fixture/ and shows animated components, how to assemble, multiple exploded views, and provides general tips.

a. Remove the 8 bolts/washers and open the cell. When viewed from the side, the rigid tubing for the anode endplate should protrude from the endplate once inserted into the proper holes (for 5 or 25 cm^2 configuration). These will hold the anode CC and FFP in place during assembly.

b. Place the rubber O-rings and CC (insulated side facing the endplate, gold-plated side facing the FFP) on the anode endplate, followed by the anode FFP. The protruding anode flow tubes will hold all these pieces in place to stand vertically. Add the alignment plastic tubes into the anode FFP alignment holes. These will be helpful in Step 6.

c. Place the cathode endplate with the size configuration holes facing up. The cathode endplate has internal flow channels machined that do not use the same tubing as the anode. Ensure the size configuration for flow matches that of the anode by using the spacers and O-rings provided with the cell. Place the cathode CC (insulated side facing the endplate and gold-plated side facing the FFP) and FFP in succession; they should both be held in place by the size configuration spacers used.

d. At this point the anode endplate/CC/FFP and cathode endplate/CC/FFP are individually ready for cell assembly. Each of these halves of the cell should be considered unit pieces (not separated from their associated parts) during the rest of the URC assembly. The two phots to the right show the URC unit pieces from two perspectives, each highlighted by green dotted lined boxes and without the membrane, anode, or cathode mounted. Step 6 describes how to mount the gaskets, electrodes, and AEM between the anode and cathode halves of the URC. At this point, confirm there is no debris visible in the FFPs that may block fluid flow. Using Kimwipes while cleaning FFPs is desirable to avoid debris left from paper towels.

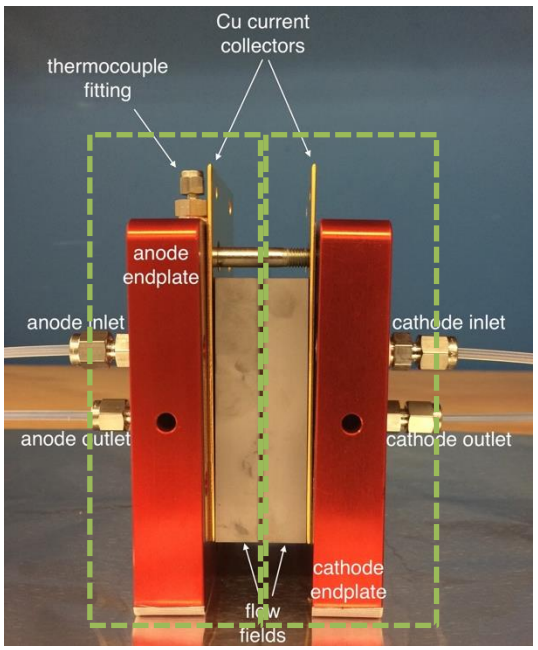

5. Remove the hydrated, alkaline AEM from the soak solution and rinse with DI water while still sandwiched between the SS mesh. Dispose of the soak and rinse solution in proper alkaline laboratory chemical waste. Keep the AEM in DI water and sandwiched between the SS screens until it is mounted into the cell in Step 6c.

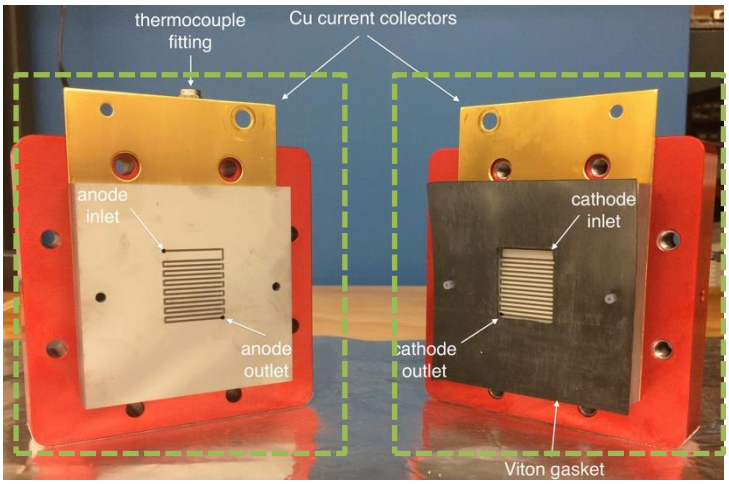

6. Sit in a chair with feet flat on the ground and knees level with hips. This is the body position I have found to be most comfortable for assembly of the URC.
    a. Hold the anode endplate/CC/FFP cradled securely in lap with the fluid tubing allowed to hang down between your knees and the FFP alignment tubes facing up. This position keeps both hands free for use in assembly.
    b. Thread the anode gasket over the alignment tubes protruding from the anode FFP, the channels in the FFP should be completely exposed in the cut-out region of the anode gasket. Place the anode inside the cut-out region of the anode gasket, ensure there is no overlap. If the gasket/electrode are laser cut this is easier; if they are hand-cut, it may require some trimming. Overlap in this stage could result in URC fluid leakage which would require disassembly, remounting, and reassembly. Because Ni hydroxide foam (NHF, a typical URC anode) has symmetrical front/back, it does not matter how NHF anode is oriented; however, if there is asymmetry to the anode, ensure the active catalyst layer is facing up.
    c. Remove the hydrated, alkaline AEM from its DI water solution and from the SS mesh supports. Let most of the water droplets drip off into the container before threading the AEM alignment holes onto the alignment tubes. Ensure the AEM lays flat on the anode/anode gasket before adding the next layers; this may require using a (gloved) hand to keep it in place.
    d. Thread the cathode gasket alignment holes over the alignment tubes. Place the cathode, catalyst layer down, into the cut-out region. Again, ensure there is no

overlap between the electrode and the gasket. Because the cathode is thinner and more flexible than the anode, it is easier for unwanted overlap to occur here. The cathode gasket should keep the AEM lying flat until the URC is compressed.

e. Keeping the entire cathode endplate/CC/FFP together, thread the cathode FFP alignment holes over the alignment tubes. At this point all the bolt holes should align with each other as well; if the bolt holes do not align, then there in an orientation mistake. This step can take some wiggling to get the endplates properly aligned. In doing so, ensure the electrodes and AEM remain aligned. If there is a question whether a layer became disrupted, it is easier to remount now than it will be later.

7. If the bolts appear dry, apply a thin layer of bolt grease to each one. This does not need to be done every time the cell is assembled. Drop the bolts and washers into their holes through the cathode endplate, screw them into the anode endplate until they are finger tight. Work in a star pattern using a 7/16” wrench to tighten each bolt until it just begins to provide resistance, still relatively loose. Do not over tighten here because the NHF will irreversibly compress.
8. Use a 7/16” torque wrench to tighten all 8 bolts, in a star pattern, until the proper compression is reached. Start with a torque of 10 lb_f-in, and work in increments of 5 lb_f-in. Each increment of 5 lb_f-in will require a few cycles of star-pattern tightening because the NHF is easily compressed. The final compression is an experimental parameter that can be optimized according to results. Too loose will not provide a liquid tight seal, and too tight

will compress the anode and increase the pressure drop required for the anode feed solution. Typically, a torque of 20–25 lb_f-in on each bolt is used. Adjust as desired.

9. Hook up the anode and cathode tubing and begin to flow DI water through each side. This works to:
    a. Ensure there are no leaks in the cell: leaks would be apparent as fluid dripping from between the FFPs.
    b. Ensure there is no membrane puncture: membrane punctures are not visible to the naked eye; however, if only one pump is on (either one) and there is fluid movement in both anode and cathode tubing, this reveals an AEM puncture.
    c. Keep the AEM hydrated: especially important if URC will not be used immediately. URC may be stored for weeks safely if the FFP chambers are filled with DI water. If there are no leaks, no AEM puncture, and you do not plan to use URC immediately, turn both of the pumps off. DI water should remain in each FFP chamber to keep the AEM from dehydrating.
10. Before using the URC for urea oxidation, the membrane must be activated. The activation process establishes ionic pathways through the membrane and ensures the alkalinity and hydration of the AEM.
    a. Activation of the membrane requires using a 1.0 M KOH feed at room temperature. The outlet of the anode may feed back into the same container. Once the tubing is hooked up, turn the pump on to 20 mL/min.
    b. The cathode solution is DI water, also at 20 mL/min and room temperature.

c. The WE/RE2 terminals of the potentiostat should be hooked up to the anode (red) CC and the CE/RE1 should be hooked up to the cathode (blue) CC.

d. A potential stairstep experiment beginning at 1.3 V up to the final URC operating potential (usually 1.9 V) in 500 mV steps is performed. Each step must be at least 5 minutes long, or enough for the current at each step to level off. At each potential step, the current will also increase in a step-change fashion followed by a relaxation until the next step is performed. Generally, the current will continue to gradually increase over many minutes while that potential is held constant, due to the formation of the ionic pathways during URC activation.

e. After the potential stairstep experiment is complete, repeat the exact same experiment two or more times until both of the following conditions are met:

   i. current density for each step is constant throughout the entire step.

   ii. successive experiments result in similar current density results at each step.

   Usually this takes around 3–5 potential step experiments, depending on step length. Because the purpose of this activation step is to ensure the AEM is ready for urea degradation, it is important to ensure that the current density during the final potential step is ~10 mA/cm^2. This is about double that expected during URC operation and ensures the AEM is plenty activated for URC operation.

Operation

Once the URC is assembled and the AEM is activated, urea oxidation experiments may be run using the following steps.

1. The anode inlet (lower on the cell compared to the anode outlet) should be fed by a solution via a pump at a flow <50 mL/min. The total volume depends on experiment length and interest. For example, if total urea conversion will be directly measured, a smaller total volume will allow for higher conversions over shorter times whereas a larger feed may not register even a small change in urea concentration for many hours (active area is only 25 cm^2). However, sometimes it may be desirable to only pass the solution once through the URC rather than recirculate it (i.e., to measure conversion per pass or to measure pH change within the cell) in which case anode inlet feed volume and flow rate will define maximum experimental time. The anode solution (bicarbonate, KOH, imitation dialysate, etc.) should be heated to 37 °C. Keep the solution covered to prevent evaporation.
2. URC performance should not be sensitive to cathode water reduction because excess catalyst has intentionally been added to ensure the water reduction does not limit overall cell reaction. (Note, if it is observed that different temperature or flowrate on cathode affects URC performance, check catalyst loading, health, mounting, compression). Cathode inlet and outlet can recirculate indefinitely in DI water beaker. This beaker does not need to be heated. Lower flow rates preserve peristaltic tubing, usually around 10–15 mL/min.

3. Heat the cell using the heating rods (one for each end plate) plugged into variable transformer (variac). Heating the cell separately from the feed solution allows for easier control of cell temperature without concern for loss of heat in tubing in route to cell. Monitor cell temperature with thermocouple inserted into cathode endplate and ensure that it stays within 1 degree of 37.0 °C while heated anode & cathode solutions are flowing at desired rates. This helps to make up for lost heat in anode tubing. Faster solution flowrates will reduce the required variac power setting for cell heating. Variac is typically set between 10 and 40% depending on other experimental conditions. Allow cell temperature and anode feed to reach a steady state (usually takes about 2 hours from room temperature) before experiments are run because rapid temperature fluctuations are more likely to occur when heating settings are changed mid-experiment.
4. Attach the working electrode (WE) and Reference 2 (RE2) of potentiostat to the anode (red) current collector and the counter electrode (CE) and Reference 1 (RE1) to the cathode. Potentiostat settings should be set so that a positive current is defined as oxidative, and a positive voltage is anodic. The total cell area should be defined (5 or 25 cm^2) and the RE type should be set to "User defined vs. NHE". These settings will result in i-V curves that represent *cell voltage* and *current density.*
5. The URC is now ready to operate for desired experiments. Typically, these are potential hold experiments at ~1.9 V with urea concentration measured before and after for associated calculations.

VITA

Kelly completed her undergraduate degree at the University of CA, Santa Barbara where she majored in Environmental Science and developed an interest in applied research for sustainable technologies through internships working on flow batteries and biofuels. This interest motivated her to apply to chemical engineering graduate programs that promote research in clean energy applications, like the UW Clean Energy Institute. Once at the University of Washington, her early research under Professor Eric Stuve was motivated by fundamental Li-air batteries and was short-lived when the opportunity to join the Center for Dialysis Innovation (CDI) research team became available. During her time at UW, Kelly enjoyed holding leadership positions as a co-leader of Time To Invent, and a member of the Program on Clime Change Graduate Student Steering Committee. She is excited to begin an industry career to apply her understanding of electrochemical systems to advance clean energy technologies like electrolyzers and fuel cells.